DTU Physics
Department of Physics

Master Thesis

Acoustic Streaming in Polymer Systems

William N. Bodé
s141209

Newtonian

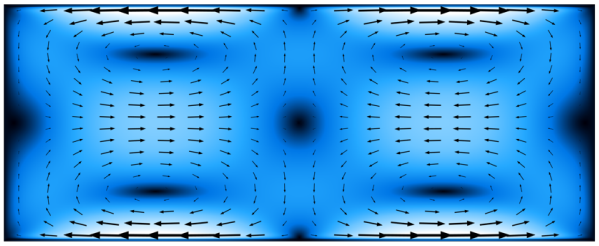

Viscoelastic

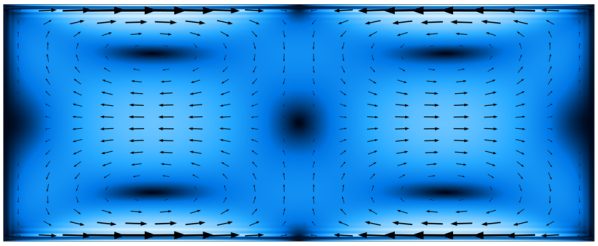

Supervisor: Henrik Bruus

Department of Physics
Technical University of Denmark

17 June 2019

Cover illustration: Acoustic streaming in a rectangular channel for a Newtonian and viscoelastic fluid. Showing the fundamental, but disguised, streaming reversal.

Abstract

Successful label-free and gentle mechanical manipulation of particles is now an out-of-the-box feature in acoustofluidics. Within acoustofluidics the manipulation of particles goes by the name acoustophoresis. This is achieved by using liquid-filled microchannels embedded in an elastic and acoustically hard material, excited by a ultrasound transducer.

In contrast to conventional hard material devices, such as silicon and Pyrex, a soft all-polymer system has been suggested. Motivated by single-use and low-cost for biotechnical applications. The acoustic contrast is now between the device as a whole and the surrounding air, which makes it a whole-system resonance. The suggested all-polymer has proven successful acoustophoresis, however the acoustic streaming has not yet been investigated in such system. In this thesis the acoustic streaming in such device will be explored by numerical simulations and compared to conventional hard systems.

A major challenge in acoustophoresis is the ability to manipulate sub-micron sized particles, since the inherent streaming dominates the particle motion. Effectively working against any desired manipulation. Motivated by this inherent phenomena we calculate the particle motion for different sized particles for the all-polymer device.

The next study is modelling and measurements of acoustophoresis in hard microchannels with soft lids, in collaboration with the Department of Biomedical Engineering at Lund university. The motivation behind this type of device is fast prototyping and the ability to suppress streaming due to the soft lid yielding to the fluid motion. The acoustic radiation force will be compared to measured particle velocities.

Finally we turn to the viscoelastic description of a fluid, focusing on acoustic streaming. Formerly this has been studied in the low-sonic regime suggesting flow reversal in the acoustic streaming. In this thesis we turn to model a viscoelastic fluid in the ultrasonic regime inside a rectangular channel.

Resumé

Vellykket etiketfri og blid mekanisk manipulation af partikler er blevet en ud af boksen løsning indenfor akustofluidik. Dette opnås ved anvendelse af væskefyldte mikrokanaler indlejret i et elastisk og akustisk hårdt materiale, der er exciteret ved ultralyd. Dette er en konsekvens af den høje akustiske kontrast mellem den væskefyldte mikrokanal og det omgivende faste materiale.

I modsætning til konventionelle hårde materialer, såsom silicium og Pyrex, er der blevet foreslået et alternativ bestående af en blød polymer. Motiveret af engangsbrug og lavpris materialer til biotekniske anvendelser. Den akustiske kontrast er nu mellem apparatet som helhed og den omgivende luft, hvilket gør det til en systemresonans. Det foreslåede polymer apparat er nu en realitet indenfor akustoforese, men den akustiske strømning er endnu ikke undersøgt i et sådanne system. I denne afhandling vil anden ordens strømning, i et polymer apparat, blive udforsket ved numeriske studier og sammenlignet med konventionelle hårde systemer.

En stor udfordring inden for akustoforese er evnen til at manipulere små partikler (mindre end én mikrometer i radius), da anden ordens strømningen dominerer partikelbevægelsen, der modarbejder enhver ønsket manipulation. Motiveret af dette fænomen beregner vi partikelbevægelsen for forskellige størrelser af partikler i polymer apparatet.

Herefter modellerer vi akustoforese i hårde mikrokanaler med bløde låg og sammenligner med målinger, i samarbejde med Institut for Biomedicinsk Engineering fra Lund Universitet. Motiveringen bag dette apparat er hurtig prototypefremstilling og evnen til at undertrykke strømning på baggrund af det bløde låg, der giver efter til væsken. Den akustiske strålingskraft vil blive sammenlignet med målte partikelhastigheder.

Endlig vil vi beskrive væsken som værende viskoelastisk og undersøge konsekvenserne heraf, med fokus på akustisk strømning. Tidligere studier i det soniske regime har antydet omvendt omdrejning i strømningen. Her vil vi modellere den viskoelastiske væske i ultralydregimet.

Preface

This thesis is submitted in agreement to the prerequisites for obtaining the degree as Master of Science and Engineering in Physics and Nanotechnology at the Technical University of Denmark. The work was carried out at the Department of Physics in the Theoretical Microfluidics group (TMF) headed by Professor Henrik Bruus. The duration of the project was close to 5 months from 4 February 2019 to 17 June 2019 corresponding to 30 ECTS points.

First I want to thank all the people in the TMF group, their dedication and professional work should be an inspiration to all. A special thanks to postdoctoral fellow Wei Qiu who is always open minded for suggestions to new experiments. I also want to point out Jacob S. Bach, who always take his time to explain and discuss physical problems, and for introducing me to his admirable effective boundary layer theory.

I also want to appreciate the cooperation with Ph.D. student Jiang Lei providing me with nice measurement presented in this thesis. Also thanks to professor emeritus Ole Hassager, who introduced us to the viscoelastic flow reversal phenomena.

Finally a special thanks to my supervisor Henrik Bruus for his ability to communicate physics and science, I am certain this is appreciated in his entire network. From my point of view he is an academic role model.

Thanks to my friend Thor for his wholehearted support throughout my time at the Technical University of Denmark and his proofreading. Of course not to forget, a huge thanks to my girlfriend Nikoline, who always seems to lift my spirit when in need.

William N. Bodé
Department of Physics
Technical University of Denmark
17 June 2019

Contents

List of Figures

List of Tables

List of symbols

Symbol	Description	SI unit
A	Area	m^2
a	Characteristic radius	m
C_{ijkl}	Fourth order stiffness tensor	Pa
C	Convergence parameters	1
c	Speed of sound	m/s
$\mathrm{d}A$	Infinitesimal area element	m^2
$\mathrm{d}V$	Infinitesimal volume element	m^3
D_i	Electric displacement field	$\mathrm{C/m}^2$
De	Deborah number	1
d_0	Displacement amplitude	m
E	Young's modulus	Pa
E_{ac}	Acoustic energy density	Pa
$\mathcal{E}$	Absolute energy	J
E_i	Electric field	V/m
$e_{ij,k}$	Piezoelectric tensor	$\mathrm{C/m}^2$
$\tilde{F}$	Helmholtz free energy per unit volume	Pa
F_i	Force vector	N
f_i	Force density vector	N
f	Frequency	Hz
$\tilde{G}$	Gibbs free energy per unit volume	$\mathrm{J/m}^3$
g_i	Gravitational acceleration	$\mathrm{m/s}^2$
H	Height	m
i	The imaginary unit $\mathrm{i} = \sqrt{-1}$	1
J_{ij}	Flux, Flux density, current density	-
K_{ij}	Stiffness matrix	-
k_0	Acoustic wavenumber	m^{-1}
k_{c}	Compressional wavenumber	m^{-1}
k_{s}	Shear wavenumber	m^{-1}
L	Characteristic length	m
Ma	Mach number	1

m_{mesh}	Edge mesh parameters	1
n_{mesh}	Domain mesh scaling	1
$\hat{n}_i$	Surface normal unit vector	1
p	pressure	
Q	Flow rate	m^3/s
R	Characteristic radius	m
r_i	Position vector	m
$\mathcal{R}$	Figure of merit	1
S	Entropy per unit mass	J/k
s	Entropy per unit volume	$\text{J}\,\text{K}^{-1}\,\text{m}^{-3}$
T	Temperature	K
$\hat{t}_i$	Tagential normal vector	1
$\tilde{U}$	Internal energy per unit volume	J/m^3
u_i	Displacement field	m
V	Volume	m^3
v_i	Velocity field	m/s
α	Acoustic perturbation parameter	1
Γ	Damping coefficient	1
γ_{ij}	Strain tensor	1
$\dot{\gamma}_{ij}$	Rate of strain tensor	1
δ	Viscous boundary layer thickness	m
δ_{ij}	Unit tensor	m
ϵ_0	Vacuum permittivity	F/m
$\epsilon_{ij,k}$	Dielectric permittivity tensor	F/m
η_0	Dynamic viscosity	Pa s
η_{b}	Bulk viscosity	Pa s
κ_0	Compressibility	Pa^{-1}
λ	Wavelength	m
ν_0	Kinematic viscosity	m^2/s
Π_{ij}	Momentum flux density tensor	Pa
ρ_0	Mass density	kg/m^3
σ	Poisson ratio	1
σ_{ij}	Elastic stress tensor	Pa
τ_{ij}	Viscous stress tensor	Pa
ϕ	Electric potential	V
Ω	Domain	1
ω	Angular frequency	s^{-1}

Bold and index notation is used interchangeably to formulate vector and tensor calculus. The index notation is denoted by Latin letters and the unit tensor is δ_{ij}. Summation over repeated index is implicit according to the Einstein summation convention.

Chapter 1

Introduction

1.1 Acoustofluidics

In the field of microfluidics and lab-on-a-chip systems, microscale acoustofluidics has emerged. As the name suggest, the concept is to utilize acoustic effects originating from sound waves in fluids contained in microchannels. The sound waves are typically ultrasound in the MHz regime, making the wavelength comparable to the microscale chip dimensions.

Perhaps the most important effect by introducing ultrasound waves in a fluid microchannel is the ability to manipulate particles gentle, non-invasive and label-free. This effect goes by the name acoustophoresis. This is now a well-known phenomena and has been used in many applications; size-independent sorting of blood cells [1], particle trapping [2] and acoustic tweezing [3]. Many of these applications involves acoustic manipulation of particles, but as the particle radius gets smaller ($<1\,\mu m$) the inherent acoustic streaming kicks in and begins to dominate the particle motion. Working against any desired acoustophoresis. This drives a desire to further understand the acoustic streaming and eventually invent methods to suppress this phenomena.

The basic design behind an acoustophoretic device is as follows: a microchannel architecture is constructed in a solid material accomplished by micro milling or cleanroom techniques. Afterwards a lid is mounted on top enclosing the microchannel. This block of material is bonded on top of a transducer either by glue or anodic bonding depending on the materials. The transducer is coupled to an alternating signal at MHz frequencies, effectively driving the whole system. At the right frequencies, resonances begins to built up in the system and eventually successful acoustophoresis arise. This is an example of a system driven by bulk acoustic waves (BAWs). Another way to excite these resonances is to use surface acoustic waves (SAWs), such a setup requires interdigitated metallic transducer electrodes on the surface of a piezoelectric material [4].

Conventional acoustophoresis has been achieved by using materials with high acoustic impedance, such as Pyrex* and silicon. We will refer to these as hard-wall systems.

These hard-wall systems makes it possible to obtain decoupled resonances due to the high acoustic contrast. The resonance will then depend on the dimensions of the microchannel e.g. a microchannel of width 375 µm will have a half-wave resonance at frequency 2 MHz. Such a device with all its relevance is depicted in Fig. 1.1.

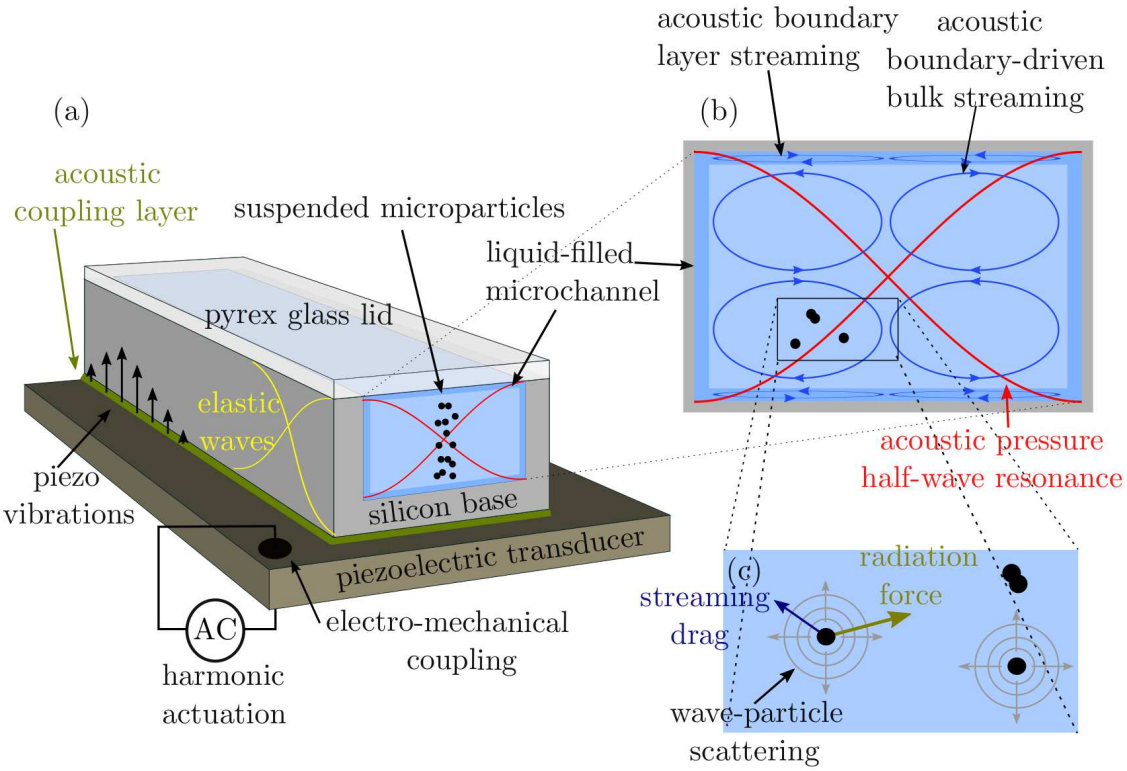

Figure 1.1: (a) Conceptual sketch behind a conventional acoustophoretic device, showing the hard silicon base microchannel with a Pyrex lid, bonded on top of a transducer coupled to an alternating signal. The alternating electric potential couples to the piezoelectric material and elastic waves starts to propagate through the silicon chip. (b) At the right frequency the elastic waves will match the half-wave resonance as indicated with red lines. (c) The standing half-wave acoustic pressure field will eventually focus particles towards the pressure nodal plane due to second order effects. As a consequence to the high amplitude pressure, acoustic streaming begins to appear as flow rolls, working against any desired focusing. The figure is adapted from Ref. [5].

*Pyrex is a borosilicate glass material and a registered trademark

For large scale production and single-use devices, Pyrex and silicon are expensive materials compared to for example polymers. Especially the polymer polymethylmethacrylat[†] (PMMA) has been predicted and observed to be a good choice of material in production of acoustophoretic devices by [6, H. Bruus and R. Moiseyenko] and the Swedish biotech company AcouSort AB [7]. However, the resonances are now coupled making it a whole-system resonance and harder to predict, nevertheless it is still a good choice of material. This new choice of material challenge the thinking of a hard-wall system.

The acoustic streaming has not yet been investigated in such polymer systems, which sets the primary motivation for this project. This thesis will focus on polymers as a material but also as a fluid (solute). The disciplines within acoustofluidic research ranges all the way from clinical research to fundamental physics and device engineering in between. This thesis seeks to connect device engineering to fundamental physics with numerical simulations as a predictive tool.

[†]commercially known as Plexiglas, Crylux, Acrylite, Lucite, and Perspex

Chapter 2

Theory

2.1 Continuum mechanics

In the continuum limit both mass and momentum densities are continuously distributed throughout space and time. The limit can be understood as being the case where infinitesimal domains of a bulk material holds the same material properties as the bulk itself. This puts an upper and lower limit for the domain at which the material is observed. The continuum frame is often used within fluid and solid mechanics, where any field is independent of coordinate system making the mathematical description that of tensor calculus. The physical fields of interest within these areas are the mass density $\rho(\mathbf{r}, t)$, pressure $p(\mathbf{r}, t)$, velocity $\mathbf{v}(\mathbf{r}, t)$ and the displacement $\mathbf{u}(\mathbf{r}, t)$ all continuous functions of position $\mathbf{r}$ and time t. Conservation laws and equations of state are then formulated in terms of these fields. The velocity of some continuous matter at position $\mathbf{r} = (x, y, z)$ is defined as the center-of-mass velocity.

2.2 Fluid mechanics

For a fluid domain Ω bounded by $\partial\Omega$ with surface outward normal $\hat{\mathbf{n}}$ the mass conservation reads

$$\partial_t \int_\Omega \rho \, \mathrm{d}V = \oint_{\partial\Omega} (-\hat{\mathbf{n}}) \cdot (\rho \mathbf{v}) \, \mathrm{d}A. \tag{2.2.1}$$

If the domain is fixed, the continuity equation can be written as

$$\partial_t \rho = -\boldsymbol{\nabla} \cdot (\rho \mathbf{v}) \quad \text{or in index notation} \quad \partial_t \rho = -\partial_j \left(\rho v_j\right), \tag{2.2.2}$$

that is the change in mass density is balanced by a mass flux density. Here the Einstein summation convention is used i.e. summation over repeated index together with the shorthand notation for the differential operators $\partial_j \equiv \frac{\partial}{\partial r_j}$ and $\partial_t \equiv \frac{\partial}{\partial t}$.

To describe the motion of a fluid we equate the rate of momentum density $\rho\mathbf{v}$ to the contributing force densities. Amounting to a momentum flux density tensor Π_{ij} and any external force density contribution f_i

$$\partial_t (\rho v_i) = -\partial_j \Pi_{ij} + f_i, \tag{2.2.3}$$

analogue to Eq. (2.2.2). The tensor Π_{ij} contains all sources of momentum transport i.e. mechanical pressure p, viscous stress tensor τ_{ij} and momentum density convection $\rho v_i v_j$

$$\Pi_{ij} = p\delta_{ij} - \tau_{ij} + \rho v_i v_j. \tag{2.2.4}$$

For a Newtonian fluid with dynamic viscosity η_0 and bulk viscosity η_b, the viscous stress tensor τ_{ij} is linear in the velocity gradient and reads

$$\tau_{ij} = \eta (\partial_j v_i + \partial_i v_j) + \left(\eta_\mathrm{b} - \frac{2}{3}\eta_0\right) \partial_k v_k \delta_{ij}. \tag{2.2.5}$$

The viscous stress tensor is defined such that the bulk viscosity η_b describes internal friction due to compression i.e. $\mathrm{Tr}\{\boldsymbol{\tau}\} = \eta_\mathrm{b} \boldsymbol{\nabla} \cdot \mathbf{v}$. For a Newtonian fluid the equation governing the fluid motion is the Navier–Stokes equation

$$\partial_t (\rho v_i) = -\partial_i p + \eta (\partial_j \partial_j v_i + \partial_j \partial_i v_j) + \left(\eta_\mathrm{b} - \frac{2}{3}\eta\right) \partial_i \partial_k v_k - \rho \partial_j (v_i v_j) + f_i \tag{2.2.6}$$

written in the well-known form

$$\rho (\partial_t + \mathbf{v} \cdot \boldsymbol{\nabla}) \mathbf{v} = -\boldsymbol{\nabla} p + \eta \nabla^2 \mathbf{v} + \left(\eta_\mathrm{b} + \frac{1}{3}\eta\right) \boldsymbol{\nabla} (\boldsymbol{\nabla} \cdot \mathbf{v}) + \mathbf{f}. \tag{2.2.7}$$

Here the material derivative appears on the left-hand side comprising the Lagrangian picture of an accelerating parcel of fluid. Together with Eq. (2.2.2) there are four equations governing three velocity components v_i and the pressure field p, and the system of equations is closed.

2.3 Sound waves in fluids

Oscillatory variations in the fluid pressure or density is called sound waves and is a direct consequence of the compressibility. These oscillatory motions causes alternating compression and are thereby manifested in disturbances to the equilibrium condition denoted with a zero subscript. Variations to the equilibrium fields can be understood within the framework of perturbation.

Working within fluid dynamics many characteristic scales appear in the governing equation, concerning the specific problem at hand. These scales form a foundation for the perturbation. Working with acoustofluidics the ratio between the flow velocity and the speed of sound appears to be the characteristic perturbation parameter, also known as

the Mach number denoted Ma. The Mach number is also a direct measure of the density variations.

If the perturbation is periodic with angular frequency $\omega = 2\pi f$, where f is the frequency, one can expand the fields as a Fourier series, making the first order term of the form $f_1(\mathbf{r},t) = f_1(\mathbf{r})\mathrm{e}^{-\mathrm{i}\omega t}$. The perturbation expansion to second order for a quiescent fluid can be written as

$$\rho(\mathbf{r},t) - \rho_0 = \rho_1(\mathbf{r})\mathrm{e}^{-\mathrm{i}\omega t} + \rho_2(\mathbf{r}), \tag{2.3.1a}$$

$$p(\mathbf{r},t) - p_0 = p_1(\mathbf{r})\mathrm{e}^{-\mathrm{i}\omega t} + p_2(\mathbf{r}), \tag{2.3.1b}$$

$$\mathbf{v}(\mathbf{r},t) - \mathbf{0} = \mathbf{v}_1(\mathbf{r})\mathrm{e}^{-\mathrm{i}\omega t} + \mathbf{v}_2(\mathbf{r}), \tag{2.3.1c}$$

where the Mach number is implicit in the subscript. Second order terms will in general have a time-independent component and a component with twice the angular frequency 2ω. In Eq. (2.3.1) the second order fields has already been time-averaged (over one cycle) and from now on the subscript "2" can be understood as an implicit time-averaged field. Throughout this thesis products of any two first order fields implies time-averaging, which makes the following identity most useful

$$\left\langle f(\mathbf{r})\mathrm{e}^{-\mathrm{i}\omega t} g(\mathbf{r})\mathrm{e}^{-\mathrm{i}\omega t}\right\rangle = \frac{1}{2}\mathrm{Re}\left\{f(\mathbf{r})^* g(\mathbf{r})\right\}. \tag{2.3.2}$$

For a field $f(\mathbf{r},t)$ with period $T = 2\pi/\omega$ the time-averaging becomes

$$\langle f(\mathbf{r},t)\rangle \equiv \frac{1}{T}\int_0^T f(\mathbf{r},t)\,\mathrm{d}t, \tag{2.3.3}$$

where the asterisk denotes complex conjugation.

It turns out that the validity of the perturbation expansion is described by the size of the parameter $\alpha = \omega d_0/c_0$, with fluid displacement d_0, angular frequency ω at which the system is actuated and the speed of sound c_0. Lets say the fluid is displaced with $d_0 = 0.1\,\mathrm{nm}$ at $\omega = 2\pi 2\,\mathrm{MHz}$. In water the speed of sound is $c_0{\sim}1\times10^3\,\mathrm{m/s}$ and the perturbation becomes correct within the small error $\alpha{\sim}10^{-6}$. At resonance the Mach number turns out to be inversely proportional to the acoustic damping factor $\Gamma{\sim}10^{-5}$ which makes the perturbation error $\alpha{\sim}10^{-1}$.

In a quiescent fluid with equilibrium density ρ_0, pressure p_0 and compressibility κ_0 the first order corrections to the continuity equation Eq. (2.2.2) reads

$$\mathrm{i}\omega\rho_1 = \rho_0\boldsymbol{\nabla}\cdot\mathbf{v}_1 \quad \text{or} \quad \mathrm{i}\omega\kappa_0 p_1 = \boldsymbol{\nabla}\cdot\mathbf{v}_1 \quad \text{where} \quad \kappa_0 = \frac{1}{\rho_0 c_0^2}, \tag{2.3.4}$$

and for the Navier–Stokes Eq. (2.2.6)

$$-\mathrm{i}\omega\rho_0\mathbf{v}_1 = -\boldsymbol{\nabla}p_1 + \boldsymbol{\nabla}\cdot\boldsymbol{\tau}_1. \tag{2.3.5}$$

For a Newtonian fluid the viscous stress tensor to first order is

$$\tau_{1,ij} = \eta_0 \left(\partial_j v_{1,i} + \partial_i v_{1,j}\right) + \left(\eta_\mathrm{b} - \frac{2}{3}\eta_0\right) \partial_k v_{1,k} \delta_{ij}. \tag{2.3.6}$$

The gravitational body force has been left out since the wavelength λ of the sound wave is much smaller than c^2/g. At MHz frequencies the relation becomes $\lambda/(c^2/g) = g/(fc_0) \approx 1 \times 10^{-9}$ so the gravitational body force can safely be ignored.

Assuming adiabatic behaviour the pressure can be expanded in terms of the mass density

$$p - p_0 = \left(\frac{\partial p(\rho_0)}{\partial \rho}\right)_S (\rho - \rho_0) + \frac{1}{2}\left(\frac{\partial^2 p(\rho_0)}{\partial \rho^2}\right)_S (\rho - \rho_0)^2 + \mathcal{O}\left(\rho^3\right), \tag{2.3.7}$$

where the subscript S denotes constant entropy per unit mass. For a full thermal treatment we refer to [8, P.B. Muller] and [9, J.T. Karlsen].

Furthermore it turns out that the isentropic derivative in the first term is the isentropic speed of sound squared c_0^2. Collecting terms to second order

$$p - p_0 = c_0^2 \rho_1 + \left(c_0^2 \rho_2 + \frac{1}{2}\frac{\partial c_0}{\partial \rho}\rho_1^2\right), \tag{2.3.8}$$

identifying the first term as the first order pressure and the term in parentheses as the second order pressure, both expressed as density variations.

Using the continuity equation Eq. (2.3.4) together with the isentropic relation Eq. (2.3.8) the divergence of Eq. (2.3.5) becomes

$$-\frac{\omega^2}{c_0^2}\left[1 - \mathrm{i}\Gamma\right]^{-1} \rho_1 = \nabla^2 \rho_1 \quad \text{where} \quad \Gamma = (1+\beta)\,\kappa_0 \eta_0 \omega. \tag{2.3.9}$$

With the acoustic damping factor Γ and $\beta = 1/3 + \eta_\mathrm{b}/\eta_0$.

Now we have a single equation governing ρ_1, thereby also p_1 since the two are proportional according to Eq. (2.3.8). For water at MHz frequencies the damping factor Γ becomes much smaller than one and Eq. (2.3.9) can be approximated by

$$-k^2 \rho_1 = \nabla^2 \rho_1 \quad \text{where} \quad k = k_0 \left(1 + \frac{\mathrm{i}\Gamma}{2}\right), \tag{2.3.10}$$

and the well-known Helmholtz equation appears with complex wavenumber k and acoustic wavenumber $k_0 = \omega/c_0$. The approximation is correct within a factor of $\Gamma \approx 10^{-5}$ and the complex wavenumber implies viscous damping. The same arguments can be made for the acoustic pressure field p_1.

2.3.1 Acoustic energy density

Propagating sound waves in fluids will transport energy. The question is how much energy is associated with a sound wave in a fluid. By using thermodynamic relations between pressure and internal energy, the acoustic energy density E_{ac} becomes the sum of kinetic and potential energy densities

$$E_{\text{ac}} = \frac{1}{2}\rho_0 \left\langle \mathbf{v}_1^2 \right\rangle + \frac{1}{2}\kappa_0 \left\langle p_1^2 \right\rangle . \tag{2.3.11}$$

Using the identity in Eq. (2.3.2) the acoustic energy density now reads

$$E_{\text{ac}} = \frac{1}{4}\rho_0 |\mathbf{v}_1|^2 + \frac{1}{4}\kappa_0 |p_1|^2. \tag{2.3.12}$$

This quantity will be used as a probe to locate acoustic resonances in the fluid domain.

Acoustic resonance

Acoustic resonance can be understood by considering the case of a fluid slap in between two infinite walls separated by the distance W, parallel to the (x, z)-plane. The walls are oscillating in anti-phase with angular frequency ω and displacement amplitude d_0, so the boundary conditions are

$$v_{1,y}(\pm W/2, t) = \pm\omega d_0 \mathrm{e}^{-\mathrm{i}\omega t}. \tag{2.3.13}$$

Due to invariance in (x, z)-plane the velocity will have a single y-component depending on the y direction. The velocity will then be irrotational and satisfy Helmholtz equation with the solution

$$\mathbf{v}_1 = \omega d_0 \frac{\sin(ky)}{\sin\left(k\frac{W}{2}\right)} \mathbf{e}_y. \tag{2.3.14}$$

By using the continuity Eq. (2.3.4) the acoustic energy density follows directly from Eq. (2.3.12)

$$E_{\text{ac}} = \frac{1}{4}\rho_0 \omega^2 d_0^2 \frac{1}{|\sin(kW/2)|^2}. \tag{2.3.15}$$

Now the average energy density in the fluid slap can be expanded around the resonance frequency ω_n

$$E_{\text{ac}} = \frac{1}{4}\rho_0 \omega^2 d_0^2 \frac{1}{|\sin(kW/2)|^2} \approx \frac{\rho_0 \omega^2 d_0^2}{4n^2\pi^2} \frac{\omega_n^2}{(\omega - \omega_n)^2 + \Gamma^2 \omega_n^2/4}, \quad \text{for} \quad \omega \approx \omega_n. \tag{2.3.16}$$

This shows that if the system is damped with the damping-factor Γ the acoustic energy will be distributed as a Lorentzian line shape near the resonance frequency ω_n. The resonance condition follows from minimising the denominator in Eq. (2.3.15) i.e. when

$$k_n = n\frac{2\pi}{W} \quad \text{or} \quad \omega_n = n\frac{2\pi c_0}{W}, \quad n = 1, 2, 3, \ldots. \tag{2.3.17}$$

Now the full width $\Delta\omega$ at half maximum can be calculated from Eq. (2.3.16) and is $\Delta\omega = \Gamma\omega_n$ defining the quality factor Q as

$$Q = \frac{\omega_n}{\Delta\omega} = \frac{1}{\Gamma}. \tag{2.3.18}$$

The quality factor is not only a measure of the width but also a direct measure of how many cycles is takes to reach the acoustic state.

2.3.2 Time-averaged second order flow: acoustic streaming

Steady acoustic phenomena can be described by the time-averaged second order fields. These slowly evolving processes can be formulated by averaging the governing equations over a full oscillation period (one cycle). This also implies that full time derivatives will average to zero. The second order corrections to the continuity equation becomes

$$0 = -\boldsymbol{\nabla} \cdot (\rho_0 \mathbf{v}_2 + \langle \rho_1 \mathbf{v}_1 \rangle), \tag{2.3.19}$$

and for the Navier–Stokes equation

$$\mathbf{0} = -\boldsymbol{\nabla} p_2 + \boldsymbol{\nabla} \cdot \boldsymbol{\tau}_2 - \rho_0 \boldsymbol{\nabla} \cdot \langle \mathbf{v}_1 \mathbf{v}_1 \rangle. \tag{2.3.20}$$

For a Newtonian fluid the second order stress tensor is

$$\tau_{2,ij} = \eta_0 \left(\partial_j v_{2,i} + \partial_i v_{2,j}\right) + \left(\eta_\mathrm{b} - \frac{2}{3}\eta_0\right) \partial_k v_{2,k} \delta_{ij}. \tag{2.3.21}$$

Here it is evident that the nonlinearities introduced in Eq. (2.3.20) arises from the inertial first order terms also known as the Reynolds stress. The steady velocity $\mathbf{v}_2$ will be referred to as the acoustic streaming velocity.

2.3.3 Acoustic radiation force

The acoustic energy density is an example of a steady second order effect which follows from the product of two first order fields. The acoustic radiation force $\mathbf{F}_\mathrm{rad}$ exerted on particles due to scattering, is another example of a second order time-averaged effect.

If the fluid contains spherical particles then the acoustic pressure waves will exert a force on the particles. The force will depend on the acoustic contrast between the particle and the surrounding fluid, determined by the mass density and compressibility. If the particle radius a is much smaller than the wavelength λ the particle can be thought of as a point scatterer. A sound wave in water at MHz frequencies will typically have wavelength of order $\lambda{\sim}1\,\mathrm{mm}$ and particles of interest will have a typical radius $a{\sim}\mu\mathrm{m}$ i.e. $a/\lambda{\sim}10^{-3}$. This makes the point scatterer a good approximation.

This scattering process can be decomposed into incoming waves denoted by the subscript "in" and a scattered wave effectively described by a monopole and dipole scattering coefficients f_mp and f_dp respectively. To calculate an expression for the radiation force due

to scattering, begins with the general expression for the force acting on a time-dependent surface

$$\mathbf{F}_{\text{rad}} = \left\langle \oint_{\partial\Omega(t)} \boldsymbol{\sigma}_2 \cdot \mathbf{n} \, \mathrm{d}A \right\rangle, \tag{2.3.22}$$

this time-dependence arises from the acoustic fields acting on the particle surface.

By expanding the time dependent surface to a fixed far-field surface enclosing the particle, the calculation reduces to a time-independent integral. The cost of expanding the surface will be the momentum-flux $\rho_0 \langle \mathbf{v}_1 \mathbf{v}_1 \rangle$ through the fixed surface $\partial\Omega$

$$\mathbf{F}_{\text{rad}} = \oint_{\partial\Omega} \left(\boldsymbol{\sigma}_2 - \rho_0 \langle \mathbf{v}_1 \mathbf{v}_1 \rangle \right) . \cdot \hat{\mathbf{n}} \, \mathrm{d}A. \tag{2.3.23}$$

In Ref. [10] this integral has been calculated and reads

$$\mathbf{F}_{\text{rad}} = -\frac{4\pi}{3} a^3 \left[\frac{1}{2} \kappa_0 \mathrm{Re} \left\{ f_{\text{mp}}^* p_{\text{in}}^* \boldsymbol{\nabla} p_{\text{in}} \right\} - \frac{3}{4} \rho_0 \mathrm{Re} \left\{ f_{\text{dp}}^* \mathbf{v}_{\text{in}}^* \cdot \boldsymbol{\nabla} \mathbf{v}_{\text{in}} \right\} \right]. \tag{2.3.24}$$

Notice how the radiation force scales with the particle volume a^3.

Here the scattering coefficients, f_{mp} and f_{dp}, are defined in terms of the non-dimensionalised material parameters

$$\tilde{\kappa} = \frac{\kappa_{\text{p}}}{\kappa_0}, \quad \tilde{\rho} = \frac{\rho_{\text{p}}}{\rho_0}, \quad \tilde{\delta} = \frac{\delta}{a} \quad \text{and} \quad \gamma = -\frac{3}{2} \mathrm{Re} \left\{ 1 + \mathrm{i} \left(1 + \tilde{\delta} \right) \right\} \tilde{\delta}, \tag{2.3.25}$$

where the particle parameters are denoted with a subscript "p". And so the scattering coefficients becomes

$$f_{\text{mp}} = 1 - \tilde{\kappa} \quad \text{and} \quad f_{\text{dp}} = \frac{2 \left(1 - \gamma \right) \left(\tilde{\rho} - 1 \right)}{2\tilde{\rho} + 1 - 3\gamma}. \tag{2.3.26}$$

For a standing pressure wave $p_1 = p_a \cos(ky)$ with potential flow $\mathbf{v}_1 \propto \boldsymbol{\nabla} p_1$ the radiation force can be evaluated from Eq. (2.3.24) yielding

$$\mathbf{F}_{\text{rad}} = 4\pi \Phi_{\text{ac}} a^3 k_0 E_{\text{ac}} \sin(2k_0 y) \mathbf{e}_y \quad \text{with} \quad E_{\text{ac}} = \frac{1}{4} \kappa_0 p_a^2, \tag{2.3.27}$$

defining the acoustic contrast factor

$$\Phi_{\text{ac}} = \frac{1}{3} \mathrm{Re} \left\{ f_{\text{mp}} \right\} + \frac{1}{2} \mathrm{Re} \left\{ f_{\text{dp}} \right\}. \tag{2.3.28}$$

This factor also determines the direction of the radiation force. The acoustic radiation force will be used to calculate particle motions.

2.4 Linear theory of elastic solids

Since the acoustics essentially originates from the displaced fluid/solid interface, we now turn to the physical description of an elastic solid with displacement field $\mathbf{u}(\mathbf{r}, t)$. Again with a common phase factor $\mathrm{e}^{-\mathrm{i}\omega t}$.

The displacement field $\mathbf{u}$ inside an elastic material describes how the material is deformed under strain. If the strain is small i.e. $|\boldsymbol{\nabla}\mathbf{u}| \ll 1$ the strain tensor γ_{ij} can be written as

$$\gamma_{ij} = \frac{1}{2}\left(\partial_j u_i + \partial_i u_j\right). \tag{2.4.1}$$

The equation of motion is obtained by equating the internal stress, defined in terms of the stress tensor σ_{ij}, to the force density which equals the acceleration in the displacement field. Within acoustics the equation of motion reads

$$-\omega^2 \rho_0 u_i = \partial_j \sigma_{ij}. \tag{2.4.2}$$

The linear theory of elastic solids assume a linear relation between stress and strain

$$\sigma_{ij} = C_{ijkl}\gamma_{kl}, \tag{2.4.3}$$

where C_{ijkl} is called the fourth-order stiffness tensor containing the elastic material parameters. For an isotropic homogeneous media the stiffness tensor is completely described by two elastic parameters. The most common pair of parameters are the Young's modulus E and the Poisson ratio σ, which describes homogeneous deformations. The Young's modulus describes the proportionality between strain and stress for homogeneous deformations

$$E = \frac{\sigma_{zz}}{\gamma_{zz}}, \tag{2.4.4}$$

where the Poisson ratio is the proportionality between orthogonal strain

$$\sigma = -\frac{\gamma_{yy}}{\gamma_{zz}} = -\frac{\gamma_{xx}}{\gamma_{zz}}. \tag{2.4.5}$$

With this set of elastic parameters the stress-strain relation takes the simple form

$$\sigma_{ij} = \frac{E\sigma}{(1-2\sigma)(1+\sigma)}\delta_{ij}\gamma_{kk} + \frac{E}{(1+\sigma)}\gamma_{ij}. \tag{2.4.6}$$

In the Voigt notation the fourth-order tensor C_{ijkl} can be replaced by a second-order tensor $C_{\alpha\beta}$ leaving out duplicates, which makes the stress-strain relation more compact

$$\sigma_\alpha = C_{\alpha\beta}\gamma_\beta. \tag{2.4.7}$$

Here the Greek letters implies Voigt notation and runs over six indices. For cubic or isotropic materials the explicit relation reads

$$\begin{pmatrix} \sigma_{xx} \\ \sigma_{yy} \\ \sigma_{zz} \\ \hline \sigma_{yz} \\ \sigma_{xz} \\ \sigma_{xy} \end{pmatrix} = \left(\begin{array}{ccc|ccc} C_{11} & C_{12} & C_{12} & 0 & 0 & 0 \\ C_{12} & C_{11} & C_{12} & 0 & 0 & 0 \\ C_{12} & C_{12} & C_{11} & 0 & 0 & 0 \\ \hline 0 & 0 & 0 & C_{44} & 0 & 0 \\ 0 & 0 & 0 & 0 & C_{44} & 0 \\ 0 & 0 & 0 & 0 & 0 & C_{44} \end{array}\right) \begin{pmatrix} \partial_x u_x \\ \partial_y u_y \\ \partial_z u_z \\ \hline \partial_y u_z + \partial_z u_y \\ \partial_x u_z + \partial_z u_x \\ \partial_x u_y + \partial_y u_x \end{pmatrix}. \tag{2.4.8}$$

For an isotropic media the elastic moduli $C_{\alpha\beta}$ are related to the longitudinal and transverse speed of sound by the relations

$$C_{11} = \rho_0 c_\mathrm{l}^2, \quad C_{44} = \rho_0 c_\mathrm{t}^2 \quad \text{and} \quad C_{12} = C_{11} - 2C_{44}. \tag{2.4.9}$$

2.4.1 Piezoelectrics

Classically the acoustofluidic chip is actuated by a piezoelectric transducer in order to reach MHz acoustic fields. The transducer is bonded directly to the chip which contains the fluid channel, this complicates the actuation at the interface. To model this piezoelectric behaviour, the electric forces in a elastic material due to the electric field is considered a part of the equation of motion. The piezoelectric effect arises from materials with an intrinsic dipole moment, which then couples to the electric field and thereby the electric field will induce additional stress in the elastic material.

By introducing the elastic solid to an electric field $\mathbf{E}$ amounts to an additional term in the internal energy per unit volume $\tilde{U}$. The energy associated with an electric displacement field $D_i = \epsilon_{ij} E_j$ per unit volume is $\mathbf{E} \cdot \mathbf{D}$ and the small change in internal energy per unit volume can be written as

$$\mathrm{d}U = \sigma_{ij} \mathrm{d}\gamma_{ij} + \mathbf{E} \cdot \mathrm{d}\mathbf{D}. \tag{2.4.10}$$

And so the Gibbs free energy $\tilde{G}$ per unit volume becomes

$$\mathrm{d}\tilde{G} = \mathrm{d}\tilde{U} - \mathrm{d}\left(\mathbf{E} \cdot \mathbf{D}\right) = \sigma_{ij} \mathrm{d}\gamma_{ij} - \mathbf{D} \cdot \mathrm{d}\mathbf{E}. \tag{2.4.11}$$

Now the thermodynamic relations are

$$\left(\frac{\partial \tilde{G}}{\partial E_k}\right)_{\gamma_{ij}} = -D_k \quad \text{and} \quad \left(\frac{\partial \tilde{G}}{\partial \gamma_{ij}}\right)_{\mathbf{E}} = \sigma_{ij}, \tag{2.4.12}$$

defining the piezoelectric tensor $e_{ij,k}$ as

$$\left(\frac{\partial \sigma_{ij}}{\partial E_k}\right)_{\gamma_{ij}} = -\left(\frac{\partial D_k}{\partial \gamma_{ij}}\right)_{\mathbf{E}} \equiv -e_{ij,k} = -e_{k,ij}. \tag{2.4.13}$$

The stress due to a linear displacement field coupled to an electric field can be written as

$$\sigma_{ij} = \left(\frac{\partial \sigma_{ij}}{\partial \gamma_{ij}}\right) \gamma_{kl} + \left(\frac{\partial \sigma_{ij}}{\partial E_k}\right) E_k = C_{ijkl} \gamma_{kl} - e_{ij,k} E_k \tag{2.4.14}$$

or in terms of the displacement field

$$D_k = \left(\frac{\partial D_k}{\partial \gamma_{ij}}\right) \gamma_{ij} + \left(\frac{\partial D_k}{\partial E_k}\right) E_k = e_{k,ij} \gamma_{ij} + \epsilon_{ki} E_i. \tag{2.4.15}$$

In this thesis the transducer will be that of a lead-zirconate-titanate ceramic (PZT-Pz26), with the coupling presented in Voigt notation

$$\begin{pmatrix} \sigma_{xx} \\ \sigma_{yy} \\ \sigma_{zz} \\ \hline \sigma_{yz} \\ \sigma_{xz} \\ \sigma_{xy} \\ \hline D_x \\ D_y \\ D_z \end{pmatrix} = \left(\begin{array}{ccc|ccc|ccc} C_{11} & C_{12} & C_{13} & 0 & 0 & 0 & 0 & 0 & -e_{31} \\ C_{12} & C_{11} & C_{13} & 0 & 0 & 0 & 0 & 0 & -e_{31} \\ C_{13} & C_{13} & C_{33} & 0 & 0 & 0 & 0 & 0 & -e_{33} \\ \hline 0 & 0 & 0 & C_{44} & 0 & 0 & 0 & -e_{15} & 0 \\ 0 & 0 & 0 & 0 & C_{44} & 0 & -e_{15} & 0 & 0 \\ 0 & 0 & 0 & 0 & 0 & C_{66} & 0 & 0 & 0 \\ \hline 0 & 0 & 0 & 0 & e_{15} & 0 & \epsilon_{11} & 0 & 0 \\ 0 & 0 & 0 & e_{15} & 0 & 0 & 0 & \epsilon_{11} & 0 \\ e_{31} & e_{31} & e_{33} & 0 & 0 & 0 & 0 & 0 & \epsilon_{33} \end{array}\right) \begin{pmatrix} \partial_x u_x \\ \partial_y u_y \\ \partial_z u_z \\ \hline \partial_y u_z + \partial_z u_y \\ \partial_x u_z + \partial_z u_x \\ \partial_x u_y + \partial_y u_x \\ \hline -\partial_x \phi \\ -\partial_y \phi \\ -\partial_z \phi \end{pmatrix}, \quad (2.4.16)$$

in the electrostatic regime where $\mathbf{E} = -\boldsymbol{\nabla}\phi$.

2.4.2 Elastic energy

The energy associated with acoustic waves in a solid is very similar to that of the acoustic energy in a fluid. The time-averaged kinetic energy density E_{kin} associated with an elastic wave at angular frequency ω is

$$E_{\text{kin}} = \frac{1}{4}\rho_0\omega^2|\mathbf{u}|^2, \quad (2.4.17)$$

and the elastic potential energy E_{pot} is given by

$$E_{\text{pot}} = \frac{1}{2}C_{ijkl}\gamma_{ij}\gamma_{kl}. \quad (2.4.18)$$

The time-averaged acoustic energy density for an elastic solid can be written as the sum of kinetic and potential energy

$$E_{\text{ac}} = \frac{1}{4}\rho_0\omega^2|\mathbf{u}|^2 + \frac{1}{4}\text{Re}\left\{(\boldsymbol{\nabla}\mathbf{u}) : \boldsymbol{\sigma}^*\right\}. \quad (2.4.19)$$

As for the acoustic energy density in the fluid domain, this quantity will be used to locate resonances in the solid domain.

2.5 Effective boundary layer theory

2.5.1 The viscous boundary layer

Working with surface phenomena such as interfaces between solid and fluid domains requires understanding of what happens in this region. The characteristic length scale at which the fluid velocity varies near such an interface happens to be the boundary layer thickness δ depending on the kinematic viscosity $\nu_0 = \eta_0/\rho_0$ and angular frequency ω

$$\delta = \sqrt{\frac{2\nu_0}{\omega}}. \quad (2.5.1)$$

To understand this length scale consider Stokes second problem; an incompressible fluid with kinematic viscosity ν_0 in contact with an oscillating wall at angular frequency ω i.e. a common phase factor $\mathrm{e}^{-\mathrm{i}\omega t}$. For an infinite wall in the (x, y)-plane the y-component of the Navier–Stokes equation reduces to Stokes flow

$$\partial_z^2 v_y^\delta(z,t) = -\frac{\mathrm{i}\omega}{\nu_0} v_y^\delta(z,t) = -\mathrm{i}\frac{2}{\delta^2} v_y^\delta(z,t). \tag{2.5.2}$$

The boundary conditions are written as

$$\mathrm{Re}\left\{v_y^\delta(0,t)\right\} = v_y^{\delta 0}\cos(\omega t) \quad \text{and} \quad v_y^\delta(z, t\to\infty) = 0, \tag{2.5.3}$$

and the solution to Stokes second problem is

$$v_y^\delta(z,t) = v_y^{\delta 0}\mathrm{e}^{\mathrm{i}k_\mathrm{s}z}\mathrm{e}^{-\mathrm{i}\omega t} \quad \text{where} \quad k_\mathrm{s} = \frac{1+\mathrm{i}}{\delta}. \tag{2.5.4}$$

Here we have introduced the shear wavenumber k_s.

This means that a shear wave travels with phase velocity $v_\mathrm{shear} = \omega\delta$ and decays exponentially with the characteristic length δ. For water at MHz frequencies the boundary layer thickness is $\delta \approx 0.5\,\mu\mathrm{m}$ so $v_\mathrm{shear} \approx 3.5\,\mathrm{m/s} \ll c_0$. This region becomes very important within the work of acoustic streaming, where the steady time-averaged fields are defined through the boundary conditions at the wall.

In general any vector field can be written as a Helmholtz decomposition $\mathbf{v} = \mathbf{v}_1^d + \mathbf{v}_1^\delta$ where

$$\boldsymbol{\nabla}\times\mathbf{v}_1^d = \mathbf{0} \quad \text{and} \quad \boldsymbol{\nabla}\cdot\mathbf{v}_1^\delta = 0, \tag{2.5.5}$$

it turns out that the δ-field corresponds to an incompressible boundary layer field as for Stokes second problem. The d-field is a potential field accounting for the compressional effects.

2.5.2 The Lagrangian no-slip boundary condition

Close to a wall the no-slip conditions has to be fulfilled at any time, if the walls are displaced by an amount $\mathbf{s}(\mathbf{s}_0, t) = \mathbf{s}_0 + \mathbf{s}_1(\mathbf{s}_0)\mathrm{e}^{-\mathrm{i}\omega t}$ around the equilibrium position $\mathbf{s}_0$ the no-slip condition reads

$$\begin{aligned}\mathbf{v}\left(\mathbf{s}\left(\mathbf{s}_0,t\right),t\right) &= -\mathrm{i}\omega\mathbf{s}_1(\mathbf{s}_0)\mathrm{e}^{-\mathrm{i}\omega t} \\ &= \mathbf{v}_1\left(\mathbf{s}_0,t\right) + \left\langle \mathbf{s}_1\cdot\boldsymbol{\nabla}\mathbf{v}_1\right\rangle\Big|_{\mathbf{s}_0} + \mathbf{v}_2\left(\mathbf{s}_0\right) + \mathcal{O}\left(s_1^2\right).\end{aligned} \tag{2.5.6}$$

This implies the first and second order Lagrangian no-slip conditions

$$\mathbf{v}_1\left(\mathbf{s}_0,t\right) = \mathbf{V}_1^0\left(\mathbf{s}_0\right)\mathrm{e}^{-\mathrm{i}\omega t} \quad \text{and} \quad \mathbf{v}_2\left(\mathbf{s}_0\right) = -\left\langle \mathbf{s}_1\cdot\boldsymbol{\nabla}\mathbf{v}_1\right\rangle\Big|_{\mathbf{s}_0}, \tag{2.5.7}$$

where $\mathbf{V}_1^0(\mathbf{s}_0) = -\mathrm{i}\omega\mathbf{s}_1(\mathbf{s}_0)$. The expansion in Eq. (2.5.6) is valid when the parallel displacement of the wall is very small compared to both the acoustic wavelength and the curvature radius of the wall, furthermore the validity requires a boundary layer much larger than the perpendicular displacement.

As a consequence to the Lagrangian no-slip boundary condition the first order no-slip condition can be written as

$$\mathbf{v}_1^{\delta 0} = \mathbf{V}_1^0 - \mathbf{v}_1^{d0}, \tag{2.5.8}$$

where the zero superscripts denotes a surface field, which is only non-zero at the wall. This condition will be used later to assess certain limits.

2.5.3 First-order acoustic pressure

In Ref. [11] they considered the separation of the short-ranged δ-field and the long-ranged d-field to formulate a boundary condition for the acoustic pressure field, which takes the viscous boundary layer effects fully into account. This can be summarised by the usual Helmholtz equation governing the acoustic pressure

$$\nabla^2 p_1 + k_\mathrm{c}^2 p_1 = 0, \quad k_\mathrm{c} = \left(1 + \mathrm{i}\frac{\Gamma}{2}\right) k_0, \tag{2.5.9}$$

with the compressional wavenumber k_c. By including the viscous boundary, the boundary condition at a wall with surface inward normal $\hat{\mathbf{n}}$ and inward normal derivative $\partial_\zeta = -\hat{\mathbf{n}}\cdot\boldsymbol{\nabla}$ turns out to be

$$\partial_\zeta p_1 = \frac{\mathrm{i}\omega\rho_0}{1-\mathrm{i}\Gamma}\left(-\hat{\mathbf{n}} - \frac{\mathrm{i}}{k_\mathrm{s}}\boldsymbol{\nabla}\right)\cdot\mathbf{V}_1^0 - \frac{\mathrm{i}}{k_\mathrm{s}}\left(k_\mathrm{c}^2 p_1 + \partial_\zeta^2 p_1\right) \quad \text{for} \quad \mathbf{r}\in\mathbf{s}_0. \tag{2.5.10}$$

This is actually the first order no-slip condition Eq. (2.5.8) in terms of the acoustic pressure field. Now $\mathbf{v}_1^\delta$ has been included analytically and the bulk field $\mathbf{v}_1^d$ is a potential flow in terms of the p_1

$$\mathbf{v}_1^d = -\mathrm{i}\frac{1-\mathrm{i}\Gamma}{\omega\rho_0}\boldsymbol{\nabla}p_1. \tag{2.5.11}$$

2.5.4 Second-order acoustic streaming

The long-ranged steady second order velocity $\mathbf{v}_2^d$ can be considered incompressible when $\Gamma \ll 1$ and the governing equations are

$$\boldsymbol{\nabla}\cdot\mathbf{v}_2 = 0, \tag{2.5.12a}$$

$$-\boldsymbol{\nabla}\left[p_2^d - \left\langle\mathcal{L}_\mathrm{ac}^d\right\rangle\right] + \eta_0\nabla^2\mathbf{v}_2^d + \frac{\Gamma\omega}{c_0^2}\left\langle\mathbf{S}_\mathrm{ac}^d\right\rangle = \mathbf{0}. \tag{2.5.12b}$$

This equation has the same form as an incompressible Stokes flow driven by the body force $\frac{\Gamma\omega}{c_0^2}\left\langle \mathbf{S}_{\mathrm{ac}}^d \right\rangle$. Here, we have introduced the long-ranged time-averaged acoustic Lagrangian density $\left\langle \mathcal{L}_{\mathrm{ac}}^d \right\rangle$ and the time-averaged energy-flux density $\left\langle \mathbf{S}_{\mathrm{ac}}^d \right\rangle$ defined as

$$\left\langle \mathcal{L}_{\mathrm{ac}}^d \right\rangle = \frac{1}{4}\kappa_0|p_1|^2 - \frac{1}{4}\rho_0\left|\mathbf{v}_1^d\right|^2 \quad \text{and} \quad \left\langle \mathbf{S}_{\mathrm{ac}}^d \right\rangle = \left\langle p_1 \mathbf{v}_1^d \right\rangle. \tag{2.5.13}$$

In addition to $\left\langle \mathbf{S}_{\mathrm{ac}}^d \right\rangle$ the viscous streaming is defined via the slip boundary condition, which can be written component-wise as

$$\mathbf{v}_2^{d0} = (\mathbf{A}\cdot\hat{\mathbf{e}}_\xi)\,\hat{\mathbf{e}}_\xi + (\mathbf{A}\cdot\hat{\mathbf{e}}_\eta)\,\hat{\mathbf{e}}_\eta + (\mathbf{B}\cdot\hat{\mathbf{e}}_\zeta)\,\hat{\mathbf{e}}_\zeta \quad \text{for} \quad \mathbf{r}\in\mathbf{s}_0. \tag{2.5.14}$$

Here the Greek letters ξ, η and ζ defines a right-handed curvilinear coordinate system with outward normal direction ζ and tangent directions ξ and η. The slip vectors $\mathbf{A}$ and $\mathbf{B}$ are

$$\begin{aligned}
\mathbf{A} = &-\frac{1}{2\omega}\mathrm{Re}\left\{\left(\mathbf{v}_1^{\delta 0}\right)^*\cdot\boldsymbol{\nabla}\left(\frac{1}{2}\mathbf{v}_1^{\delta 0} - \mathrm{i}\mathbf{V}_1^0\right) - \mathrm{i}\left(\mathbf{V}_1^0\right)^*\cdot\boldsymbol{\nabla}\mathbf{v}_1^d\right.\\
&\left. + \left[\frac{2-\mathrm{i}}{2}\boldsymbol{\nabla}\cdot\left(\mathbf{v}_1^{\delta 0}\right)^* + \mathrm{i}\left(\boldsymbol{\nabla}\cdot\left(\mathbf{V}_1^0\right)^* - \partial_\zeta\left(v_{1\zeta}^d\right)^*\right)\right]\mathbf{v}_1^{\delta 0}\right\},\\
\mathbf{B} = &\frac{1}{2\omega}\mathrm{Re}\left\{\mathrm{i}\left(\mathbf{v}_1^{d0}\right)^*\cdot\boldsymbol{\nabla}\mathbf{v}_1^d\right\}.
\end{aligned} \tag{2.5.15}$$

These equations lay the foundation for the effective boundary layer theory for an arbitrary curved surface.

2.6 Viscoelastic fluids

Materials which exhibits both viscous and elastic properties are called viscoelastic or soft materials e.g. polymer solutions, colloidal systems and polymer melts. These materials can be characterised by a stress relaxation modulus $G(t)$.

If the strain $\Delta\gamma_{ij,n}$ happens at time t_n the stress τ_{ij} at time t is given by

$$\tau_{ij}(t) = G(t-t_n)\Delta\gamma_{ij,n}, \tag{2.6.1}$$

where index i and j refers to the tensor components and n is the summation index.

Assuming linear superposition the stress becomes

$$\tau_{ij}(t) = \sum_{n=1}^{N} G(t-t_n)\Delta\gamma_{ij,n}. \tag{2.6.2}$$

In the continuous limit the sum can be replaced by an integral

$$\tau_{ij}(t) = \int_{-\infty}^{t} G(t-t')\,\dot{\gamma}_{ij}(t')\,\mathrm{d}t', \tag{2.6.3}$$

where $\dot{\gamma}_{ij}(t') = \frac{\mathrm{d}\gamma_{ij}(t')}{\mathrm{d}t} = (\partial_j v_i + \partial_i v_j)(t')$ is the rate of strain containing the velocity gradient.

The lower limit is rather arbitrary as long as it contains the time at which the strain began and has been set to $-\infty$ for mathematical convenience. Eq. (2.6.3) forms the simplest linear viscoelastic model between stress and rate of strain. The relaxation modulus can be assumed to have the form

$$G(t) = \frac{\eta_0}{\lambda} \mathrm{e}^{-t/\lambda}. \tag{2.6.4}$$

Evaluating this form of relaxation in Eq. (2.6.3)

$$\tau_{ij}(t) = \frac{\eta_0}{\lambda} \int_{-\infty}^{t} \mathrm{e}^{-(t-t')/\lambda} \, \dot{\gamma}_{ij}(t') \, \mathrm{d}t', \tag{2.6.5}$$

known as the Maxwell constitutive equation. A differential equation with Eq. (2.6.5) as solution is

$$\tau_{ij} + \lambda \frac{\partial}{\partial t} \tau_{ij} = \eta_0 \dot{\gamma}_{ij}. \tag{2.6.6}$$

This equation is known as Jeffrey's model and forms a differential equation for τ_{ij}. If the system is driven by the angular frequency ω the characteristic viscoelastic scaling becomes $\lambda\omega$, also known as the Deborah number denoted De.

It turns out that by going from a curvilinear system to a fixed coordinate system the operator $\frac{\partial}{\partial t}$ should be replaced with the upper-convected time derivative defined as

$$\overset{\nabla}{A}_{ij} = \partial_t A_{ij} + v_k \partial_k A_{ij} - A_{ik} \partial_k v_j - \partial_k v_i A_{kj}, \tag{2.6.7}$$

for an arbitrary tensor A_{ij}. This was derived by J. G. Oldroyd in 1950 and also goes by the name Oldroyd derivative [12] . The constitutive equation can now be written as

$$\tau_{ij} + \lambda \overset{\nabla}{\tau}_{ij} = \eta_0 \dot{\gamma}_{ij}, \tag{2.6.8}$$

this form is known as the convected Jeffrey's model and forms a quasi-liner differential model. For a complete derivation of this we refer to Ref. [13].

2.6.1 Perturbation within the convected Jeffrey's model

To model a viscoelastic fluid using the convected Jeffrey's constitutive equation defined in Eq. (2.6.8), requires a model of $\boldsymbol{\tau}_1$ and $\boldsymbol{\tau}_2$ defined in the perturbation scheme Eq. (2.3.5) and Eq. (2.3.20). To first order the upper-convected time derivative Eq. (2.6.7) reduces to ∂_t and for the harmonic driven system Eq. (2.6.8) becomes

$$\boldsymbol{\tau}_1 = \eta(\omega)\left(\boldsymbol{\nabla}\mathbf{v}_1 + (\boldsymbol{\nabla}\mathbf{v}_1)^T\right), \tag{2.6.9}$$

where the dynamic viscosity now depends on the angular frequency

$$\eta(\omega) = \frac{\eta_0}{1 - \mathrm{i}\omega\lambda}. \tag{2.6.10}$$

To second order, the stress tensor reads

$$\begin{aligned}\boldsymbol{\tau}_2 =& \eta_0\left[\boldsymbol{\nabla}\mathbf{v}_2 + (\boldsymbol{\nabla}\mathbf{v}_2)^T\right] \\ &- \lambda\left[\langle(\mathbf{v}_1\cdot\boldsymbol{\nabla})\,\boldsymbol{\tau}_1\rangle - \langle\boldsymbol{\tau}_1\cdot\boldsymbol{\nabla}\mathbf{v}_1\rangle - \left\langle(\boldsymbol{\nabla}\mathbf{v}_1)^T\cdot\boldsymbol{\tau}_1\right\rangle\right].\end{aligned} \tag{2.6.11}$$

In the viscous limit $\lambda = 0$ the stress tensor reduces to the incompressible Newtonian fluid.

Chapter 3

Numerical implementation in the COMSOL software

Now that the relevant continuum fields has been introduced together with the conservation laws and we are ready to describe the numerical implementation.

3.1 Finite elements and the weak formulation

The finite element method (FEM) is a method to solve partial differential equations. The idea is to discretise a domain Ω bounded by $\partial\Omega$ (Fig. 3.1) into finite elements, making it possible to approximate any field by a finite basis, defined on each element. Consider a physical field $g(\mathbf{r})$, this field can be approximated in terms of the finite basis

$$g(\mathbf{r}) = \sum_n a_n \hat{g}_n(\mathbf{r}), \tag{3.1.1}$$

defined by the set of test functions $\{\hat{g}_n\}$ and expansion coefficient a_n. The test functions are defined on each element with a finite overlap as sketched in Fig. 3.1. The test functions ranges from unity at the mesh vertex and decays to zero at the neighbouring nodes, the sketch indicates linear test functions, however in the numerical model the test functions will be polynomials of order higher than two.

This basis will be used to calculate approximate solution to equations of the strong form

$$\boldsymbol{\nabla} \cdot \mathbf{J} - F = 0. \tag{3.1.2}$$

Here $\mathbf{J}$ can be appreciated as a generalised flux driven by the force F, luckily almost every conservation law can be formulated in this way.

The weak formulation is now established by projecting the test function onto Eq. (3.1.2)

$$\int_\Omega \hat{g}_m(\mathbf{r}) \left[\boldsymbol{\nabla} \cdot \mathbf{J}\left[g(\mathbf{r})\right] - F(\mathbf{r})\right] \mathrm{d}V = 0, \quad \text{for all } m. \tag{3.1.3}$$

For a linear flux operator we have $\mathbf{J}[g(\mathbf{r})] = \sum_n a_n \mathbf{J}[\hat{g}_n(\mathbf{r})]$ and the weak formulation can be written as a matrix inversion problem

$$\mathbf{K} \cdot \mathbf{a} = \mathbf{F}, \tag{3.1.4}$$

where the stiffness matrix $\mathbf{K}$ and force vector $\mathbf{F}$ are defined as

$$K_{mn} = \int_\Omega \hat{g}_m(\mathbf{r}) \boldsymbol{\nabla} \cdot \mathbf{J}[\hat{g}_n(\mathbf{r})] \, \mathrm{d}V \quad \text{and} \quad F_m = \int_\Omega \hat{g}_m(\mathbf{r}) F(\mathbf{r}) \, \mathrm{d}V. \tag{3.1.5}$$

Solving Eq. (3.1.2) has now been formulated in terms of a matrix problem determining the expansion coefficients $\{a_n\}$ through matrix inversion.

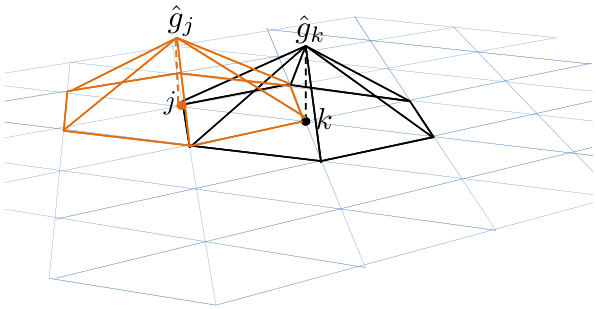

Figure 3.1: Finite element method: 2D depiction of two overlapping test-functions $\hat{g}_k$ and $\hat{g}_j$ in the discretised domain Ω centred over node k and j, respectively. The test functions are spanned by the neighbouring nodes to node k and j. Note that the tent-shape of these basis functions is due to linear (first order) polynomials describing the decrease from value 1 to 0 on neighbouring nodes.

3.1.1 Boundary conditions in COMSOL

Physical systems are uniquely defined by their boundary conditions and by using Gauss' theorem on Eq. (3.1.3) we can immediately address the boundary value problem

$$\int_{\partial\Omega} \hat{g}_m \hat{\mathbf{n}} \cdot \mathbf{J} \, \mathrm{d}A - \int_\Omega \left(\hat{g}_m F + \boldsymbol{\nabla} \hat{g}_m \cdot \mathbf{J}\right) \mathrm{d}V = 0. \tag{3.1.6}$$

This makes it easy to describe the boundary conditions via the term $\hat{\mathbf{n}} \cdot \mathbf{J}$ either by imposing a constraint on the flux

$$\hat{\mathbf{n}} \cdot \mathbf{J} = N(\mathbf{r}) \quad \text{for} \quad \mathbf{r} \in \partial\Omega \tag{3.1.7}$$

known as a Neumann boundary condition or by a constraint on the field

$$g(\mathbf{r}) = D(\mathbf{r}) \quad \text{for} \quad \mathbf{r} \in \partial\Omega, \tag{3.1.8}$$

known as a Dirichlet boundary condition.

Now it is a matter of implementing the weak formulation within the finite element method numerically. This has been done in the commercial available software COMSOL Multiphysics® 5.4 making it straight forward to work with the weak formulation using the predefined "Weak Form PDE" physics package [14]. This software package will be referred to as COMSOL.

3.2 Numerical convergence

Doing numerical simulations requires some kind of numerical convergence criteria. In this section the reference model system will be tested by mesh convergence, defined by the convergence parameter

$$C[g] = \sqrt{\frac{\int |g(\mathbf{r}) - g_{\text{ref}}(\mathbf{r})|^2 \, \mathrm{d}A}{\int |g_{\text{ref}}(\mathbf{r})|^2 \, \mathrm{d}A}}, \tag{3.2.1}$$

taking any field g as input and comparing it to the best resolved solution g_{ref}. By definition $C \to 0$ as $g \to g_{\text{ref}}$. This criteria is adapted from Ref. [15].

The reference model system comprises a solid domain with displacement field $\mathbf{u}$ and a fluid domain with acoustic pressure p_1 and second order velocity $\mathbf{v}_2$. In order to make a mesh convergence a mesh scale needs to be defined for each domain, in this case the wavenumber $k_0^{-1} = \omega/c_0$ for the fluid domain and the transverse wavenumber $k_{\text{t}} = \omega/c_{\text{t}}$ for the solid domain, where the mesh is homogeneously distributed throughout both domains*.

The mesh scale factors are $(k_0 n_{\text{mesh}})^{-1}$ and $(k_{\text{t}} n_{\text{mesh}})^{-1}$, where the convergence is made in the interval from $n_{\text{mesh}} = 1$ to $n_{\text{mesh}} = 15$, in steps of one with reference solution $n_{\text{mesh}} = 30$.

First a mesh convergence is carried out for a coupled system with homogeneous mesh throughout both domains plotted in Fig. 3.2.(A), using the effective boundary layer theory presented in Section 2.5. For the homogeneous distributed mesh, the best solution $n_{\text{mesh}} = 30$ corresponds to 344 050 domain elements and 2274 boundary elements, effectively solving for 3 160 261 degrees of freedom (DOF).

*homogeneous in the sense that the mesh density is spatially constant in both domains.

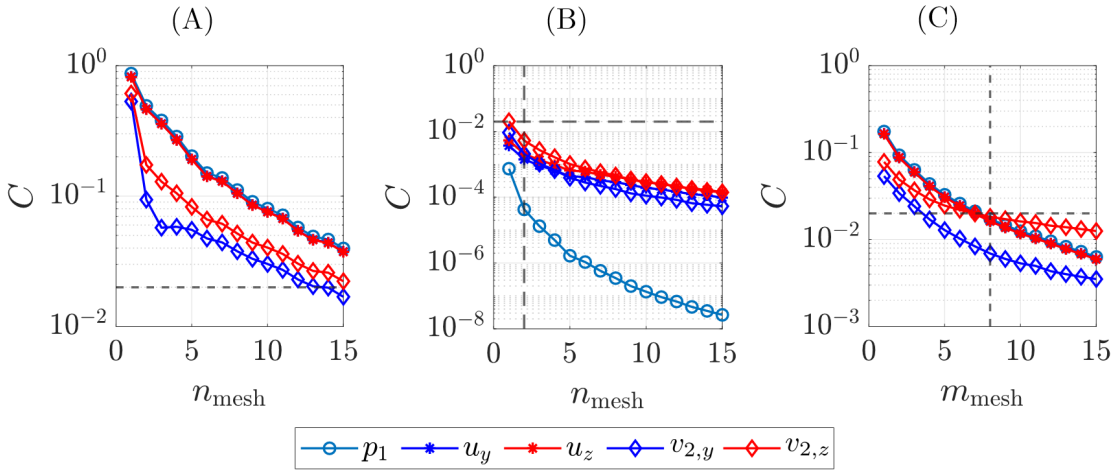

Figure 3.2: Mesh convergence parameter for different mesh settings plotted on a semilog scale. (A) Coupled system with homogeneously distributed mesh. (B) Decoupled system with homogeneously distributed mesh. (C) Coupled system where the interface is resolved at $100\delta/m_{\mathrm{mesh}}$.

By choosing the maximum allowed numerical error to be $C = 2 \times 10^{-2}$, the homogeneous mesh setting does not reach the desired criteria. However in a decoupled system where the displacement field does not couple to the acoustic pressure the convergence criteria happens already at $n_{\mathrm{mesh}} = 2$ for all the fields. This is indicated as dashed lines in Fig. 3.2.(B). By choosing these mesh scalings for each domain and combining it with a better resolved interface $100\delta/m_{\mathrm{mesh}}$, meaning that the boundary nodes is equidistant separated by $100\delta/m_{\mathrm{mesh}}$. The coupled system converge to the desired value at $n_{\mathrm{mesh}} = 2$ and $m_{\mathrm{mesh}} = 8$ resulting in 16 534 domain elements and 598 boundary elements, effectively solving for 181 771 degrees of freedom (DOF).

This convergence analysis emphasise how important it is to resolve the interface between two coupled fields, where the individual domains can be rather coarse resolved.

Chapter 4

Reference model system

The focus of this thesis will primarily concern the microfluidic device sketched in Fig. 4.1. The device consist of a solid chip of length $L_{\mathrm{sl}} = 5.0\,\mathrm{cm}$ and width $W_{\mathrm{sl}} = 3\,\mathrm{mm}$ on top of a piezoelectric transducer having the same length as the solid and width $W_{\mathrm{pzt}} = 10\,\mathrm{mm}$. Inside the chip there is a fluid microchannel with height $H_{\mathrm{fl}} = 150\,\mu\mathrm{m}$ and width $W_{\mathrm{fl}} = 375\,\mu\mathrm{m}$. In Fig. 4.1.(B) the slit size inside the transducer is denoted $\Delta W = 100\,\mu\mathrm{m}$, this slit has been cut in order to achieve a push pull effect appropriate for the acoustic resonance. The design of the end-channel/outlet depends on the desired acoustophoretic outcome, that is why it has been left out. One example is to let the flow channel end in a trifurcation, making it possible to separate and/or concentrate the particles from the medium [16].

This design is used by the Swedish biotech company AcouSort AB and patented by H. Bruus and R. Moiseyenko. AcouSort is specialised in standalone laboratory products and integrated OEM* solutions based on ultrasound, with focus on commercializing the products. The company was founded in 2010 by four professors situated at Lund university and in 2017 the company went public at the Swedish stock AktieTorget.

This section will provide the necessary equations and boundary conditions in order to model such systems . The physics has been simplified to two dimensions, since the length of the device is large compared to the width and we can assume invariance in the x-direction close to mid-channel length. Plus the flow in the length direction can be assumed laminar working with microfluidics. The 2D model cross-section is taken to be right in between the inlet and outlet and the cross-section is shown in Fig. 4.1.(B) with dimensions in Table 4.1.

*original equipment manufacturer

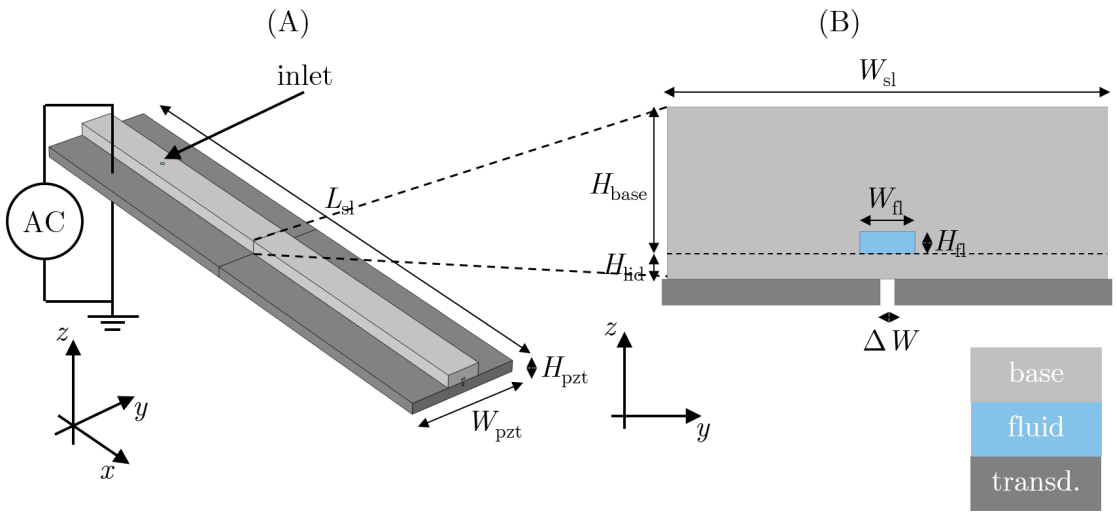

Figure 4.1: (A) 3D view of the full acoustic device; solid chip (light gray) on top of a piezoelectric transducer (dark gray). (B) Enlarged cross-sectional view of the acoustic device with fluid channel (blue) inside the solid base material (light gray), later the lid and base will be of different materials, the lid is indicated as a dashed line.

Table 4.1: Dimensions for the reference device with a transducer slit size of $\Delta W = 100\,\mu\text{m}$.

Parameter	base	lid	PZT	fluid (fl)	Unit
Width, W_i	3000	3000	10,000	375	µm
Height, H_i	1000	175	1000	150	µm
Length, L_i	5.0	5.0	5.0	4.0	cm

4.1 Governing equations

The governing equations has already been established in Chapter 2. This model will couple the acoustic fields to the displacement in the solid, all of which originates from the transducer coupled to an alternating signal with angular frequency ω. The piezoelectric effect couples the displacement and electric field and the alternating signal makes it a harmonic disturbance throughout the system.

Throughout this chapter the weak form Eq. (3.1.3) will be used to implement the governing equations in the COMSOL software, that is why we need equations of the strong form Eq. (3.1.2). Both the transducer and the base has the displacement field $\mathbf{u}$ governed by Eq. (2.4.2) according to linear theory of elastic solids. It is straight forward to convert Eq. (2.4.2) to the strong form in terms of Voigt notation written out explicitly in

Eq. (2.4.8), and the strong form governing the displacement field is

$$J_{ij}^{(\mathbf{u})} = \sigma_{ij}, \tag{4.1.1a}$$

$$F_i^{(\mathbf{u})} = \rho_0 \omega^2 \left(1 + \mathrm{i}\Gamma_{\mathrm{sl}}\right)^2 u_i. \tag{4.1.1b}$$

The artificial damping factor Γ_{sl} has been substituted $\omega \to \omega\left(1 + \mathrm{i}\Gamma_{\mathrm{sl}}\right)$ in order to mimic the damping inside the solid. The equations governing the linear displacement inside the piezoelectric transducer are also of the form Eq. (4.1.1) with an additional coupling between the electric field and the linear displacement.

In the electrostatic regime we write $\mathbf{E} = -\boldsymbol{\nabla}\phi$ and the weak form governing the electrical potential ϕ is

$$J_k^{(\phi)} = D_k = e_{k,ij}\gamma_{ij} - \epsilon_{ki}\partial_i\phi, \tag{4.1.2a}$$

$$F^{(\phi)} = 0, \tag{4.1.2b}$$

which is exactly the quasi-static equation

$$\boldsymbol{\nabla} \cdot \mathbf{D} = 0. \tag{4.1.3}$$

The coupling between displacement and electric potential for the PZT ceramic Pz26 are best illustrated in terms of Voigt notation explicit in Eq. (2.4.16).

For the first order acoustic pressure field the governing equation is the continuity equation Eq. (2.3.4) so

$$J_i^{(p_1)} = 0, \tag{4.1.4a}$$

$$F^{(p_1)} = -\partial_i v_{1,i} + \mathrm{i}\omega\kappa_0 p_1. \tag{4.1.4b}$$

The first order acoustic velocity field is governed by the linear Navier–Stokes equation Eq. (2.3.5) written in strong form as

$$J_{ij}^{(\mathbf{v}_1)} = -p_1\delta_{ij} + \tau_{1,ij} = -p_1\delta_{ij} + \eta_0\left(\partial_j v_{1,i} + \partial_i v_{1,j}\right) + \left(\eta_{\mathrm{b}} - \frac{2}{3}\eta_0\right)\partial_k v_{1,k}\delta_{ij}, \tag{4.1.5a}$$

$$F_i^{(\mathbf{v}_1)} = -\mathrm{i}\rho_0\omega v_{1,i}. \tag{4.1.5b}$$

For the effective boundary layer theory the acoustic pressure is governed by the Helmholtz equation Eq. (2.5.9) with compressional wavenumber k_{c}

$$J_i^{(p_1)} = \partial_i p_1, \tag{4.1.6a}$$

$$F^{(p_1)} = -k_{\mathrm{c}}^2 p_1. \tag{4.1.6b}$$

Turning to the second order time-averaged fields, starting with the pressure p_2 governed by continuity equation Eq. (2.3.19)

$$J_i^{(p_2)} = \rho_0 v_{2,i} + \left\langle \rho_1 v_{1,i} \right\rangle, \tag{4.1.7a}$$

$$F^{(p_2)} = 0, \tag{4.1.7b}$$

and the steady second order time-averaged velocity $\mathbf{v}_2$ governed by the second order Navier–Stokes equation

$$J_{ij}^{(\mathbf{v}_2)} = -p_2\delta_{ij} + \tau_{2,ij} - \rho_0 \langle v_{1,i} v_{1,j} \rangle \tag{4.1.8a}$$

$$= -p_2\delta_{ij} + \eta_0 \left(\partial_j v_{2,i} + \partial_i v_{2,j}\right) + \left(\eta_\mathrm{b} - \frac{2}{3}\eta_0\right) \partial_k v_{2,k}\delta_{ij} - \rho_0 \langle v_{1,i} v_{1,j} \rangle ,$$

$$F_i^{(\mathbf{v}_2)} = 0. \tag{4.1.8b}$$

Again the second order time-averaged acoustic fields can be written differently using the effective boundary layer theory. The second order pressure field is still governed by Eq. (4.1.7) but the second order bulk velocity field is now a Stokes flow where

$$J_{ij}^{(\mathbf{v}_2^d)} = -\left(p_2^d - \left\langle \mathcal{L}_\mathrm{ac}^d \right\rangle\right)\delta_{ij} + \eta_0 \partial_j v_{2,i}^d, \tag{4.1.9a}$$

$$F_i^{(\mathbf{v}_2^d)} = -\frac{\Gamma_\mathrm{fl}\omega}{c_0^2} \left\langle p_1 v_{1,i}^d \right\rangle . \tag{4.1.9b}$$

Now the first order acoustic fields serves as source terms in the equations governing the second order fields and couples via the governing equations. The displacement and acoustic fields is not coupled via the governing equations but will couple through the boundary conditions.

4.2 Boundary conditions

Any physical system is unique in terms of the given boundary conditions, these conditions for the acoustofluidic device sketched in Fig. 4.1 will now be presented, starting with the ambient air surrounding the device. Here we impose zero stress across all boundaries facing the air, corresponding to (1,2,3,4b) in Fig. 4.2, that is

$$\hat{\mathbf{n}} \cdot \boldsymbol{\sigma} = \mathbf{0} \quad \text{for} \quad \mathbf{r} \in (1, 2, 3, 4\mathrm{b}). \tag{4.2.1}$$

The actuation driven by the PZT transducer will be modelled as an idealized boundary condition due to simplification and the desire to get elementary understanding of the system. This idealized push-pull actuation can be written as

$$\mathbf{u} = -\mathrm{sgn}(y) d_0 \hat{\mathbf{e}}_z \quad \text{for} \quad \mathbf{r} \in (4\mathrm{a}, 4\mathrm{c}). \tag{4.2.2}$$

Same procedure as in previous work Ref. [6, 17], where it is pointed out that an amplitude of $d_0 = 0.1 - 0.3\,\mathrm{nm}$ predicts realistic acoustic scales measured in Ref. [15]. Numerically the boundary condition is implemented as a constraint on the displacement field.

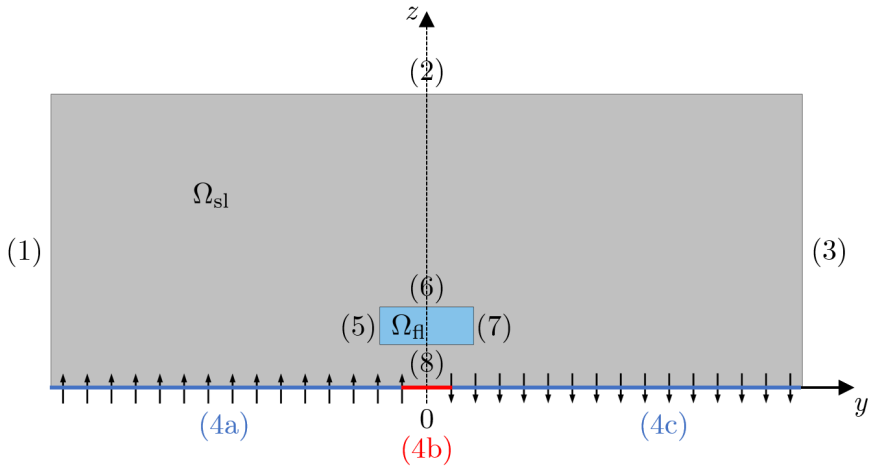

Figure 4.2: 2D sketch of the model including the simplified boundary condition, representing the actual PZT transducer (black arrows). Each boundary is numbered with an ID in order to ease the references.

The displacement field and the acoustic fields couples on the interface separating the two domains via the continuous stress and velocity condition. The continuous velocity across the fluid-solid interfaces can be written as

$$\hat{\mathbf{n}} \cdot \mathbf{v}_1 = \partial_t \mathbf{u} \cdot \hat{\mathbf{n}} = -\mathrm{i}\omega \mathbf{u} \cdot \hat{\mathbf{n}} \quad \text{for} \quad \mathbf{r} \in (5, 6, 7, 8), \tag{4.2.3}$$

in COMSOL this is implemented as a Dirichlet boundary condition.

The fluid exerts a normal stress on the solid which serves as a weak contribution to the normal stress in the solid

$$\hat{\mathbf{n}} \cdot \boldsymbol{\sigma} = -p_1 \hat{\mathbf{n}} \quad \text{for} \quad \mathbf{r} \in (5, 6, 7, 8). \tag{4.2.4}$$

The time-averaged second order pressure enters only as a gradient in the equations. This makes the second pressure level arbitrary, and we average it to zero for the entire domain. This sets the global constraint

$$\int_{\partial\Omega} p_2 \, \mathrm{d}A = 0. \tag{4.2.5}$$

For the second order time-averaged velocity $\mathbf{v}_2$ the no-slip sets a boundary condition. This is also described in Eq. (2.5.6) and reads

$$\langle \mathbf{v}_2 \rangle = -\langle (\mathbf{u} \cdot \boldsymbol{\nabla}) \, \mathbf{v}_1 \rangle \quad \text{for} \quad \mathbf{r} \in (5, 6, 7, 8), \tag{4.2.6}$$

originating from Stokes drift.

4.2.1 Effective boundary layer conditions

In the limit of weakly curved and thin boundary layers the effective boundary layer theory can be applied. This allows for numerical ease since the boundary layer effects are included analytically, hence the boundary layer does not have to be resolved in the numerical model. This makes it preferable over the complete acoustic model presented above. The governing equations were that of Helmholtz equation governing the acoustic pressure and Stokes flow for the time-averaged second order velocity. These equations were presented in the weak form Eq. (4.1.6) and Eq. (4.1.9).

The boundary condition for the first order stress are qualitatively the same as the continuous stress across boundaries, however by inclusion the boundary layer effects amounts to an additional term in Eq. (4.2.4) due to the viscous shear stress

$$\hat{\mathbf{n}} \cdot \boldsymbol{\sigma} = -p_1 \hat{\mathbf{n}} + \mathrm{i}k_\mathrm{s}\eta_0 \left(\mathbf{V}_1^0 + \frac{\mathrm{i}}{\omega\rho_0} \boldsymbol{\nabla} p_1 \right) \quad \text{for} \quad \mathbf{r} \in (5, 6, 7, 8). \tag{4.2.7}$$

This is implemented as a weak contribution to the linear displacement field. The continuous stress condition on the fluid is now

$$\partial_\zeta p_1 = \frac{\mathrm{i}\omega\rho_0}{1 - \mathrm{i}\Gamma} \left(-\hat{\mathbf{n}} - \frac{\mathrm{i}}{k_\mathrm{s}} \boldsymbol{\nabla} \right) \cdot \mathbf{V}_1^0 - \frac{\mathrm{i}}{k_\mathrm{s}} \left(k_\mathrm{c}^2 p_1 + \partial_\zeta^2 p_1 \right) \quad \text{for} \quad \mathbf{r} \in (5, 6, 7, 8). \tag{4.2.8}$$

This condition is also implemented as a weak contribution to the acoustic pressure field.

The second order slip velocity defines the boundary condition for the time-averaged second order bulk velocity field $\mathbf{v}_2^d$ as presented in Eq. (2.5.15). For the given 2D acoustofluidic system, with unit normal vector $\hat{\mathbf{n}}$ and unit tangential vector $\hat{\mathbf{t}}$, the condition reduces to

$$\mathbf{v}_2^d = \left(\mathbf{A}_y \hat{t}_y + \mathbf{A}_z \hat{t}_z \right) \hat{\mathbf{t}} + \left(\mathbf{B}_y \hat{n}_y + \mathbf{B}_z \hat{n}_z \right) \hat{\mathbf{n}}. \tag{4.2.9}$$

Chapter 5

Selected acoustofluidic devices

Using the numerical model presented in Chapter 4 we demonstrate how acoustophoresis can be accomplished in conventionally hard systems, where the microchannel is embedded inside Pyrex bonded to a piezoelectric transducer. Following R. Moiseyenko and H. Bruus [6], the idea of an all-polymer system is also evaluated as an acoustophoretic device. As mentioned the all-polymer based device has already been proposed and used by the Swedish biotech company AcouSort and some of the content serves as a verification against the numerical results presented in Ref. [6].

Typically transducers of thickness 1 mm will be most active in the low MHz regime, this is also the reasoning for choosing a fluid channel width $W_{\mathrm{fl}} = 375\,\mu\mathrm{m}$ matching the wavelength. The frequencies of interest will therefore be in the range from 1 MHz to 2.1 MHz. The system will be actuated by the idealized anti-symmetric push pull indicated in Fig. 4.2, with a displacement amplitude of $d_0 = 0.3\,\mathrm{nm}$.

5.1 Acoustic contrast

We start by considering Pyrex as the surrounding material. Pyrex is a glass type material mainly composed of SiO_2. The material parameters for Pyrex are given in Table A.3. Here the specific impedance in the solid Z_{sl}, is defined in terms of the longitudinal speed of sound

$$Z_{\mathrm{sl}} = \rho_{\mathrm{sl}} c_{\mathrm{l}}. \tag{5.1.1}$$

For Pyrex this equals $Z_{\mathrm{py}} = 12.47\,\mathrm{MPa\,s/m}$ and for water it is $Z_{\mathrm{wa}} = 1.49\,\mathrm{MPa\,s/m}$, which sets a huge contrast in acoustic properties. The huge difference in impedance makes sound waves almost completely confined to their respective domains, i.e. no transmission. This can be understood by considering the reflection coefficient R defined as the ratio between the energy-flux density in the reflected compared to the incident wave. At a plane surface

separating two infinite materials, the reflection coefficient at normal incidence is given as

$$R = \left(\frac{\tilde{Z} - 1}{\tilde{Z} + 1} \right)^2 \quad \text{where} \quad \tilde{Z} = \frac{Z_{\text{sl}}}{Z_{\text{fl}}}. \tag{5.1.2}$$

This is of course not the whole story, since the transmitted waves in the solid domain also consist of shear waves and not only longitudinal, but for normal incidence we see only longitudinal waves in both domains.

The reflection coefficient is plotted in Fig. 5.1 as a function of the relative impedance $\tilde{Z}$, this shows how the wave becomes completely reflected when $Z_{\text{sl}} \gg Z_{\text{fl}}$ or $Z_{\text{sl}} \ll Z_{\text{fl}}$, and complete transmission at $\tilde{Z} = 1$. For Pyrex more than 50% of the wave is reflected, that is why we call it a hard material. Whereas the polymers polydimethylsiloxane (PDMS) and PMMA are close to one making it soft acoustic materials.

This brief analysis was carried out to outline the concept of acoustic contrast and how it affects wave propagation. A complete description of transmission and reflection in a finite cavity remains.

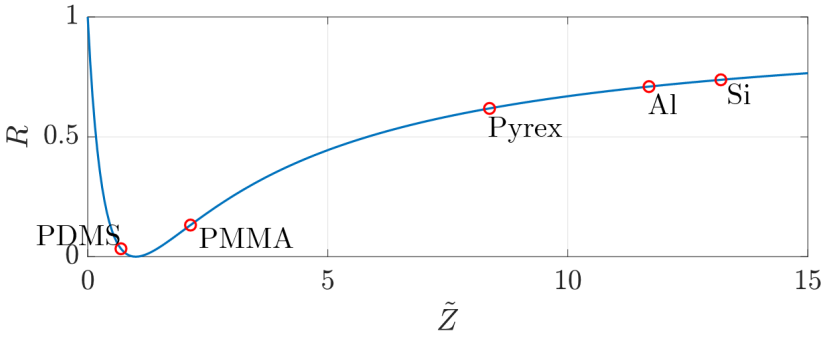

Figure 5.1: Reflection coefficient as a function of relative impedance between solid and fluid. Typical solid materials used for acoustofluidic devices are indicated with name and point.

5.2 Hard material device

To see the effect of embedding a water channel inside the Pyrex in terms of acoustic resonances, the acoustic energy in the solid $E_{\text{ac}}^{(\text{sl})}$ is probed with and without the water-filled channel. This is presented in Fig. 5.2.(A). The water parameters at 25 °C are given in Table A.1.

Without the water channel there seems to be three distinct resonances and by including the water one more resonance appear at $f = 1.851\,\text{MHz}$, where the other resonances seems

to shift down in frequency. In Fig. 5.2.(B) the absolute acoustic energies according to

$$\mathcal{E}_{\mathrm{ac}}^{(\mathrm{sl})} = \int_{\Omega_{\mathrm{sl}}} E_{\mathrm{ac}}^{(\mathrm{sl})}\,\mathrm{d}A \quad \text{and} \quad \mathcal{E}_{\mathrm{ac}}^{(\mathrm{fl})} = \int_{\Omega_{\mathrm{fl}}} E_{\mathrm{ac}}^{(\mathrm{fl})}\,\mathrm{d}A \tag{5.2.1}$$

are calculated. This shows how the water contains more energy at $f = 1.851\,\mathrm{MHz}$ even though the solid domain is sixty times larger. The same can be said about the densities, where the water has an exceptional high acoustic energy density of 1935 Pa compared to 20 Pa in the Pyrex. This is clear evidence of a decoupled water channel resonance due to the high acoustic contrast $Z_{\mathrm{py}}/Z_{\mathrm{wa}} \gg 1$. Further evidence of a decoupled resonance is the frequency itself. Lying close to the half-wave resonance of the water cavity, which is $f = c_0/(2W_{\mathrm{fl}}) = 2.00\,\mathrm{MHz}$, indicated as a dashed line in Fig. 5.2.

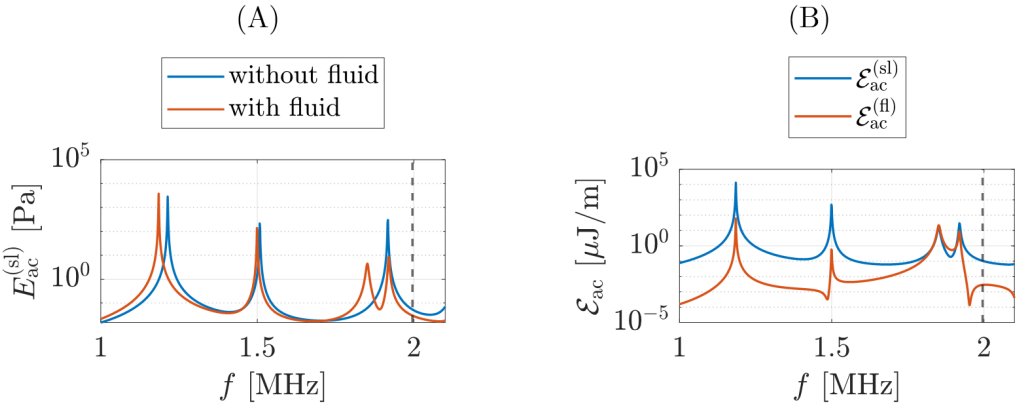

Figure 5.2: (A) Elastic energy spectrum with and without the fluid channel on a logarithmic scale. (B) Acoustic energy spectrum in the Pyrex and water domain. The dashed line indicates the distinct half-wave water resonance.

5.3 Acoustophoresis

As already touched upon in the introduction, the ability to manipulate particles inside fluid cavities is known as acoustophoresis. The focusing of particles originates from the acoustic resonances inside the fluid cavities which is the reasoning behind probing the acoustic energy as we sweep in the frequency domain.

The resonance will appear as peaks in the energy spectrum as seen in Fig. 5.2. These resonances represents configurations where the system contains an exceptional amount of energy. But it is hard to qualify the acoustophoresis by looking at the energy spectrum alone. In order to do so, the acoustic radiation force Eq. (2.3.24) is calculated according to the weighted averages

$$\bar{F}_y = \frac{1}{W_{\mathrm{fl}} H_{\mathrm{fl}}} \int_{\Omega_{\mathrm{fl}}} \frac{y}{|y|} \mathbf{F}_{\mathrm{rad}} \cdot \mathbf{e}_y \,\mathrm{d}A \quad \text{and} \quad \bar{F}_z = \frac{1}{W_{\mathrm{fl}} H_{\mathrm{fl}}} \int_{\Omega_{\mathrm{fl}}} |\mathbf{F}_{\mathrm{rad}} \cdot \mathbf{e}_z| \,\mathrm{d}A, \tag{5.3.1}$$

presented in Fig. 5.3 and calculated for 5-µm-radius polystyrene particles, with material parameters given in Table A.2. The weight $y/|y|\mathrm{d}A$ is a measure of how well the radiation force focus the particles towards the centre plane at $y = 0$. To qualify the ability to focus particles i.e. acoustophoresis we adopt the figure of merit $\mathcal{R}$ from Ref. [6]

$$\mathcal{R} = -\frac{\bar{F}_y}{\bar{F}_z}. \tag{5.3.2}$$

A good resonance is characterised by high acoustic energy density and a large figure of merit. That is why we use the weighted acoustic energy density

$$\tilde{E}_{\mathrm{ac}} = E_{\mathrm{ac}}\mathcal{R}, \tag{5.3.3}$$

to qualify the resonances according to strong acoustophoresis. This quantity is plotted in Fig. 5.3.(B) and shows how the resonance at $f_3 = 1.851\,\mathrm{MHz}$ has the largest peak.

The resonances properties are given in Table 5.1 and actually the figure of merit is much larger than unity for all four resonances. This indicates resonances with good focusing properties.

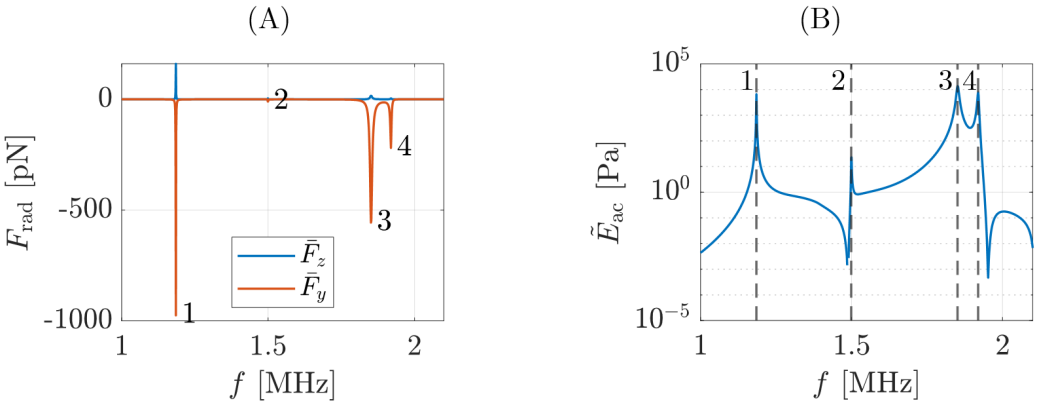

Figure 5.3: (A) Weighted radiation force components as a function of frequency. (B) Weighted acoustic energy density $\tilde{E}_{\mathrm{ac}}$, on a semilog scale, qualifying the acoustic resonance in terms of the desired centre plane focusing. Both calculated as a function of frequency from 1 MHz to 2.1 MHz.

Table 5.1: Resonance characterisation for the hard material Pyrex. The different resonances are presented together with their acoustic energy density $E_{\mathrm{ac}}^{(\mathrm{fl})}$, their radiation force components $\bar{F}_y$ and $\bar{F}_z$ and the figure of merit $\mathcal{R}$.

Resonance	Frequency [MHz]	$E_{\mathrm{ac}}^{(fl)}$ [Pa]	$\bar{F}_y$ [pN]	$\bar{F}_z$ [pN]	$\mathcal{R}$ 1
f_1	1.185	1.08×10^3	-979	160	6.12
f_2	1.499	13.9	-13.5	6.17	2.19
f_3	1.851	1.97×10^3	-2763	81.3	34.0
f_4	1.919	556	-786	17.0	46.2

According to the weighted acoustic energy density $\tilde{E}_{\mathrm{ac}}$ the best and worst resonances are evaluated. Field plots are presented in Fig. 5.4. The worst is shown to emphasise and test the predictive ability, using the weighted acoustic energy density as a qualifier.

The acoustic pressure field in Fig. 5.4.(B) at $f_3 = 1.851\,\mathrm{MHz}$ represents a standing half-wave, resulting in almost perfect focusing. Where the pressure field in Fig. 5.4.(D) at $f_2 = 1.499\,\mathrm{MHz}$ also indicates a half-wave resonance with centre focusing. However, the acoustic radiation force seems to have a negative vertical component near the side edges.

The maximum displacement amplitudes $|\mathbf{u}|/d_0 = 478$ and $|\mathbf{u}|/d_0 = 82$ are indicated for each resonance in Fig. 5.4 both resonances seems to gain three order of magnitude compared to the actuation amplitude $d_0 = 0.3\,\mathrm{nm}$. Notice how the displacement is much larger at $f_2 = 1.499\,\mathrm{MHz}$, even though the acoustic pressure is higher at f_3. This is clear evidence of decoupled resonances, and the f_3 resonance can be identified as a water channel resonance, whereas f_2 can be identified as a Pyrex resonance.

Even though we call it best and worst, both resonances seems to posses the ability to focus particles towards $y = 0$.

The decoupled resonances is a clear feature to the high acoustic contrast in the system. By smearing out this contrast the system becomes even more coupled and complex, which will be introduced in the next section.

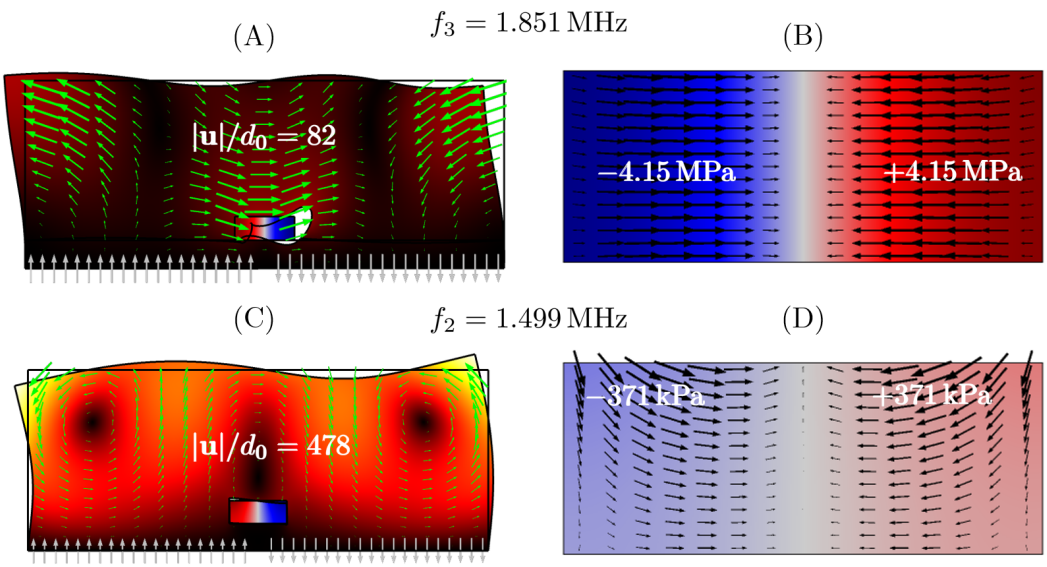

Figure 5.4: Numerical results for the best and worst resonance for the Pyrex device with actuation amplitude $d_0 = 0.3\,\mathrm{nm}$. (A)-(B) are for the best resonance $f_3 = 1.851\,\mathrm{MHz}$ and (C)-(D) are $f_2 = 1.499\,\mathrm{MHz}$. (A) Displacement field is presented both as magnitude (surface plot) and vector field (green arrows). The actuation is indicated as gray arrows at the bottom surface. (B) Acoustic pressure (surface plot) in the fluid domain together with the acoustic radiation force field (black arrows) on 5-µm-radius polystyrene particles. (C) and (D) are as (A) and (B). The deformation lines has been increased by a factor of 10,000 in (A) and 2,000 in (C) and the displacement magnitude ranges from 0 (dark) to $478d_0$ (light). The pressure magnitude ranges from −4.15 MPa (blue) to 4.15 MPa (red) symmetric around 0 (gray).

5.4 Soft material device

The meaning of soft materials within acoustics refers to the acoustic impedance being similar to that of water and by looking at Fig. 5.1, both PDMS and PMMA have acoustic impedances almost that of water.

This section will be analogous to Section 5.2, the only difference is the solid material being soft. Instead of Pyrex we now use the polymer PMMA with specific impedance $Z_{\mathrm{PMMA}} = 3.19\,\mathrm{MPa\,s/m}$ twice that of water. The material is cheap compared to Pyrex, so the big question is; can one obtain the same acoustophoresis properties using PMMA instead of Pyrex. If so, the chip would be suitable for particle studies where possible cross contamination makes single-use devices a necessity.

Again the acoustic energy in the solid is probed with and without the water-filled channel and plotted in Fig. 5.5, very different from the acoustic energies in the hard Pyrex device

in Fig. 5.2.(A). Here we see no evidence of decoupled resonances.

For the soft material device the acoustic contrast is not between the water and the surrounding PMMA but between the device and the surrounding air. That is why the system and its resonance should be considered as a whole.

To see how the fluid couples with the surrounding PMMA the acoustic energy in both domains are plotted as a function of frequency in Fig. 5.5.(B). One distinct feature is that the acoustic energy in the water is everywhere smaller compared to the acoustic energy in the PMMA. The energy density in the water on the other hand can be higher at certain resonances.

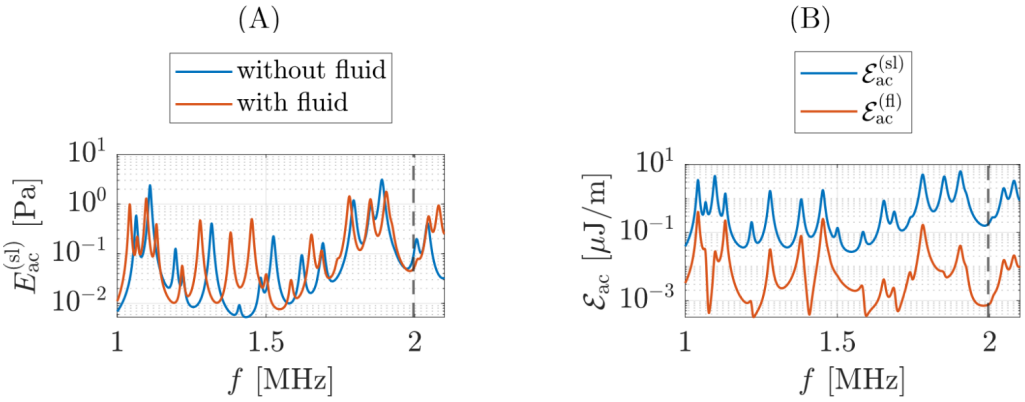

Figure 5.5: PMMA-Water system. (A) Elastic energy spectrum with and without the water filled channel on a logarithmic scale. (B) Acoustic energy spectrum in the PMMA (sl) and water (fl) domain. Dashed line indicates the distinct half-wave water resonance located at 2 MHz. The energies are again probed in the interval from 1 MHz to 2.1 MHz.

Another way to characterise the difference between hard and soft materials, is to consider the characteristic wavelengths in the elastic solid, for PMMA the transverse $\lambda_{\mathrm{t}} = c_{\mathrm{t}}/f$ and longitudinal wavelength $\lambda_{\mathrm{l}} = c_{\mathrm{l}}/f$ at 2 MHz are

$$\lambda_{\mathrm{t}} = 0.6\,\mathrm{mm} \quad \text{and} \quad \lambda_{\mathrm{l}} = 1.3\,\mathrm{mm} \quad (\mathrm{PMMA}) \quad , \tag{5.4.1}$$

whereas for Pyrex they are

$$\lambda_{\mathrm{t}} = 1.7\,\mathrm{mm} \quad \text{and} \quad \lambda_{\mathrm{l}} = 2.8\,\mathrm{mm} \quad (\mathrm{Pyrex}) \quad . \tag{5.4.2}$$

By comparing the wavelength to the dimensions of the device e.g. the height $H_{\mathrm{sl}} = 1.2\,\mathrm{mm}$ and width $W_{\mathrm{sl}} = 3\,\mathrm{mm}$ it is seen how the PMMA parameters allows for smaller wavelength to exist in the system, allowing more resonance modes to form. This is also evident from the number of resonances in the spectrum; for the Pyrex device we found four resonance whereas the PMMA device had sixteen resonances in the same frequency domain.

To qualify the different resonances the acoustic radiation forces is plotted in Fig. 5.6.(A) according to Eq. (5.3.1). Again the figure of merit $\mathcal{R}$ should be maximised together with the acoustic energy density E_{ac} indicating good centre focusing. The three best and worst resonance values are given in Table 5.2 and by purely considering the focusing properties resonance number four $f_4 = 1.132\,\text{MHz}$ is by far the best. The worst focusing seems to be number fifteen at $f_{15} = 2.047\,\text{MHz}$. This is also in accordance with the weighted energy density $\tilde{E}_{\text{ac}}$ as shown in Fig. 5.6.(B) where the good resonances is represented as peaks.

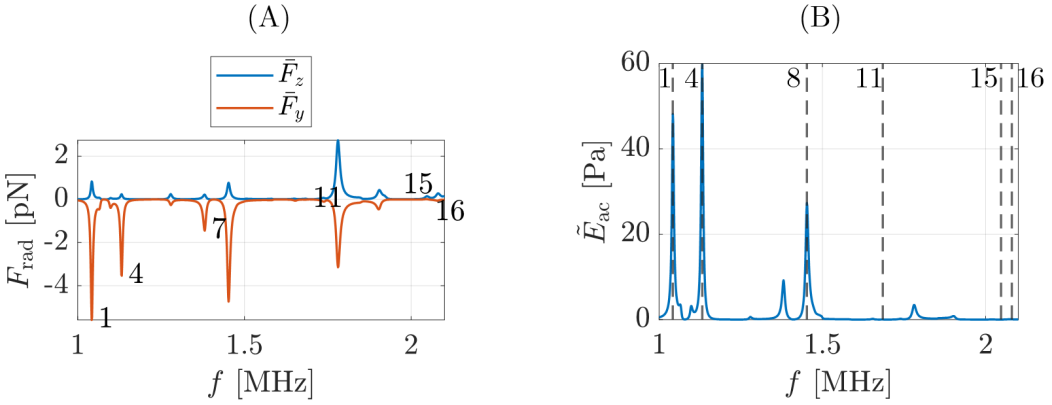

Figure 5.6: PMMA-Water system. (A) Weighted radiation force components. (B) Weighted acoustic energy density $\tilde{E}_{\text{ac}}$ qualifying the centre-plane focusing.

Table 5.2: Three best and worst resonances sorted to the figure of merit. The different resonances are presented together with their acoustic energy density $E_{\text{ac}}^{(\text{fl})}$, their radiation force components $\bar{F}_y$ and $\bar{F}_z$ and the figure of merit $\mathcal{R}$. All the resonance properties are given in Table B.2.

Resonance	Frequency [MHz]	$E_{\text{ac}}^{(\text{fl})}$ [Pa]	$\bar{F}_y$ [pN]	$\bar{F}_z$ [pN]	$\mathcal{R}$ 1
4	1.132	3.97	−3.53	0.24	15.0
1	1.042	7.14	−5.58	0.83	6.74
8	1.453	4.44	−4.73	0.77	6.14
11	1.685	0.04	−0.01	0.03	0.41
16	2.080	0.37	−0.05	0.28	0.20
15	2.047	0.28	0.01	0.15	−0.07

To elaborate on the whole-system resonances, the first order fields at these frequencies are presented in Fig. 5.7, together with the time averaged radiation force field analogue to Fig. 5.4. According to the weighted acoustic energy density $\tilde{E}_{\text{ac}}$ the best centre focusing occurs at $f_4 = 1.132\,\text{MHz}$ (see Table 5.2). From the acoustic pressure field and the time-

averaged acoustic radiation force in Fig. 5.7.(B) it turns out to be in agreement with the prediction.

The worst resonance seems to be $f_{15} = 2.047\,\text{MHz}$, this is also supported by the field plots in Fig. 5.7.(D), here the radiation force tends to move the particles towards the upper corners (the gray area), however there still exist a nodal plane at the centre, but for centre focusing this resonance is bad.

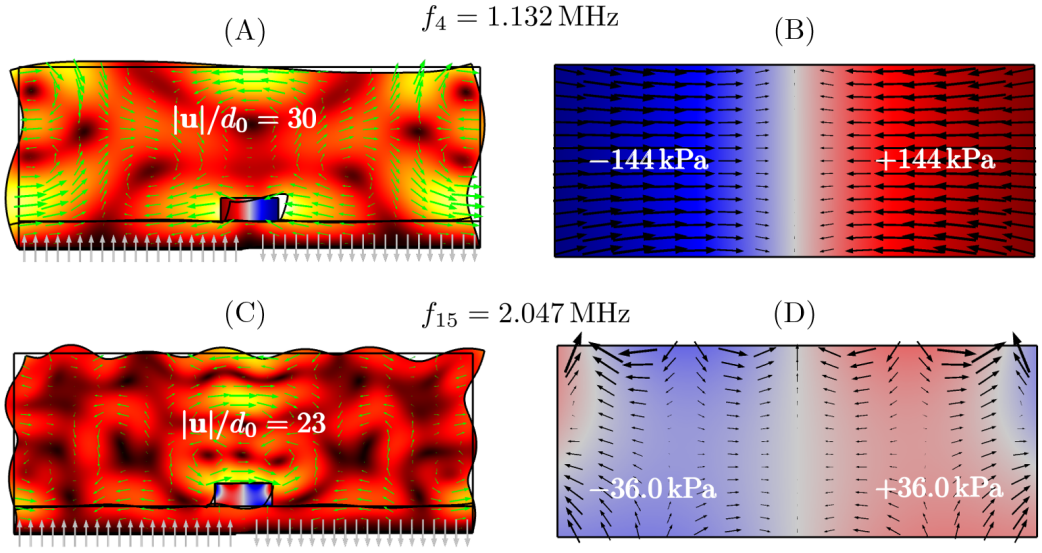

Figure 5.7: Numerical results for the best and worst resonance for the PMMA device with actuation amplitude $d_0 = 0.3\,\text{nm}$. (A)-(B) are for the best resonance $f_4 = 1.132\,\text{MHz}$ and (C)-(D) the worst $f_{15} = 2.047\,\text{MHz}$. (A) Displacement field is presented both as magnitude (surface plot) and vector field (green arrows). The actuation is indicated as gray arrows at the bottom surface. (B) Acoustic pressure (surface plot) in the fluid domain together with the radiation force field (black arrows) on 5-µm-radius polystyrene particles. (C) and (D) are as (A) and (B). The deformation lines has been increased by a factor of 30,000 in (A) and (C). The displacement magnitude ranges from 0 (dark) to $30d_0$ (light). The pressure magnitude ranges from −144 kPa (blue) to +144 kPa (red) symmetrically around 0 (gray).

This section emphasises the fundamental difference between hard and soft materials and tries to give a guiding picture of how the acoustic properties changes when going to soft all-polymer devices, where the resonances should be considered as a whole-system resonance instead of decoupled.

5.5 Parametric studies for the PMMA device

Numerical simulations allows for immediate studies of how the system depends on certain configurations, for example material parameters and chip designs. The ability to do these parametric studies is a great advantage in designing and optimizing acoustofluidic systems.

5.5.1 Base height study

There exist arbitrary many combinations and complications turning to parametric studies and one should always consider the relevance and context towards experimental partners. The study of the width dependence towards the resonance is one example, and has been studied in Ref. [6]. As a first step towards understanding the resonance/width correlation is to consider the shear half-waves at the edges in the solid domain. For a decoupled shear-wave obeying the Helmholtz equation the two-dimensional resonance condition reads

$$f = \frac{c_\mathrm{t}}{2}\sqrt{\frac{n_y^2}{W_\mathrm{sl}^2} + \frac{n_z^2}{H_\mathrm{sl}^2}}, \quad W_\mathrm{sl} = \frac{n_y}{\sqrt{\frac{4f^2}{c_\mathrm{t}^2} - \frac{n_z^2}{H_\mathrm{sl}^2}}} \quad \text{or} \quad H_\mathrm{sl} = \frac{n_z}{\sqrt{\frac{4f^2}{c_\mathrm{t}^2} - \frac{n_y^2}{W_\mathrm{sl}^2}}}, \tag{5.5.1}$$

where n_i can be thought of as the number of half shear waves in each direction. For the resonance in Fig. 5.7.(A) this correspond to $n_y = 1$ and $n_z = 2$. This turns out to agree fairly with the numerical results in Ref. [6].

It is natural to expand this study by making the same analysis in terms of the base height H_base and keeping the lid height constant $H_\mathrm{lid} = 175\,\mu\mathrm{m}$. The device used by AcouSort has a base height of $H_\mathrm{base} = 1000\,\mu\mathrm{m}$ [18].

To investigate the base height implications on the whole-system resonance, the base height is varied from $H_\mathrm{base} = 1000\,\mu\mathrm{m}$ to $H_\mathrm{base} = 325\,\mu\mathrm{m}$ in steps of $75\,\mu\mathrm{m}$. Such that the last configuration is symmetric around the horizontal mid-plane, as indicated in Fig. 5.8.(A).

For each height a energy spectrum is calculated from $f = 1.0\,\mathrm{MHz}$ to $f = 2.1\,\mathrm{MHz}$ together with the weighted radiation force components according to Eq. (5.3.1). Each resonance is represented as a point in Fig. 5.8.(B), whereas the size/area of each point is proportional to $\tilde{E}_\mathrm{ac}$. This plot makes it possible to identify good resonances according to acoustophoresis, with the ability to focus particles toward the nodal plane at $y = 0$. The best resonances seems to lie in the same region marked by the blue ellipse. Above 1.5 MHz the resonances are bad according to the weighted acoustic energy and almost non-existing.

By changing the base thickness H_base from the reference value 1 mm to 0.4 mm, the best resonance according to the size of the scatter plot Fig. 5.8 changes from 1.132 MHz to 1.29 MHz. The acoustic energy density changes from 4.0 Pa to 110 Pa almost two order of magnitude greater, just by having a thinner base, which also carries the benefit of less use of material. The resonances tendency is in fair agreement with Eq. (5.5.1) plotted as a red line in Fig. 5.8.(B) and can be used as a qualitative prediction.

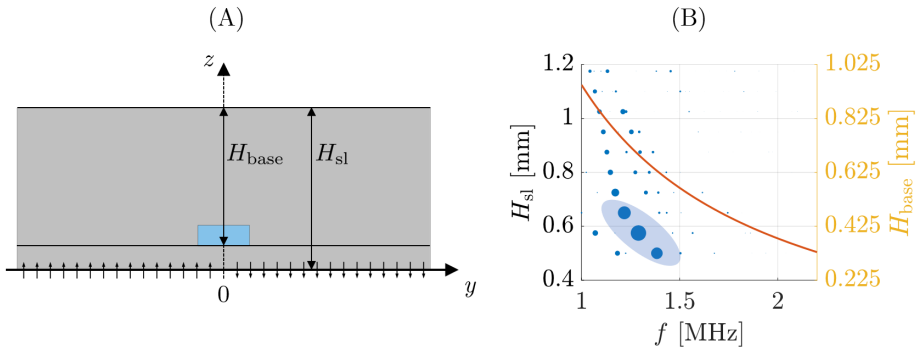

Figure 5.8: (A) The PMMA device indicating the heights used for the parametric sweep. The lid thickness is kept constant while the base thickness is varied i.e. $H_{\text{sl}} = H_{\text{base}} + H_{\text{lid}}$. (B) Resonance plot weighted to the acoustic energy density and figure of merit. Each point correspond to a resonance at the given base height and the size of each point is proportional to $\tilde{E}_{\text{ac}}$ i.e. a large point means good acoustophoretic properties. The best acoustophoresis is marked by the blue ellipse. The red curve indicates how a decoupled transverse wave resonance depends on the base height.

In order to completely validate these solutions the first order acoustic pressure and the time-averaged radiation force is plotted, for each of the three best resonances in Fig. 5.9. These fields agrees with the predicted quality according to the scatter plot and $\tilde{E}_{\text{ac}}$. If we were able to built this device at base height 0.4 mm instead of 1 mm we would achieve acoustic pressure magnitudes comparable to the one obtained for the Pyrex device, according to our numerical study.

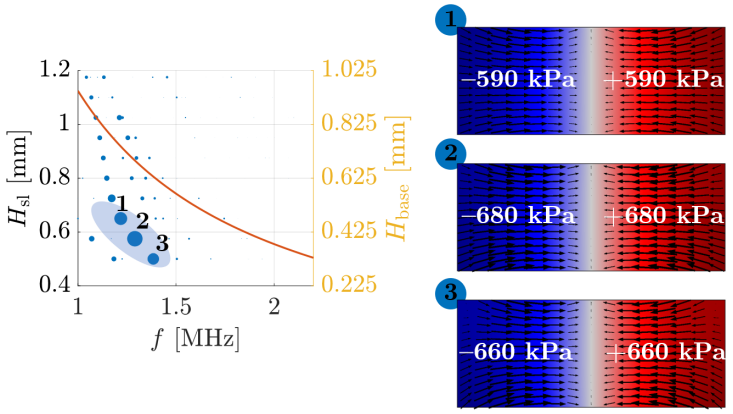

Figure 5.9: Acoustic pressure field for each of the three best resonances according to the weighted acoustic energy density $\tilde{E}_{\text{ac}}$. Each resonance is enumerated according to the scatter plot. The acoustic pressure p_1 (surface plot) is plotted together with the radiation force $\mathbf{F}_{\text{rad}}$ (black arrows). The magnitudes of the acoustic pressure is written in each figure.

Together with the width dependence analysed in Ref. [6] it seems that by minimising the solid domain the resonance becomes stronger in the sense of higher acoustic energy density and better focusing properties.

5.5.2 Channel position study

The channel position is rather easy to manipulate when designing and manufacturing the device, that is why this subsection will serve as a study towards understanding the channel position effect on the whole-system resonance. The procedure is as follows; the device dimensions is kept the same as in the reference device presented in Fig. 4.1 with dimensions in Table 4.1. The channel position will be varied as indicated in Fig. 5.10.(A) in steps of 75 µm starting from the reference design. Here the channel center position is at $y = 0\,\mu\text{m}$ and $z = 250\,\mu\text{m}$. The final position of the channel corresponds to the setup where the transducer now sits on top of the reference design, here the channel center position is $y = 0\,\mu\text{m}$ and $z = 925\,\mu\text{m}$—also indicated in Fig. 5.10.(A).

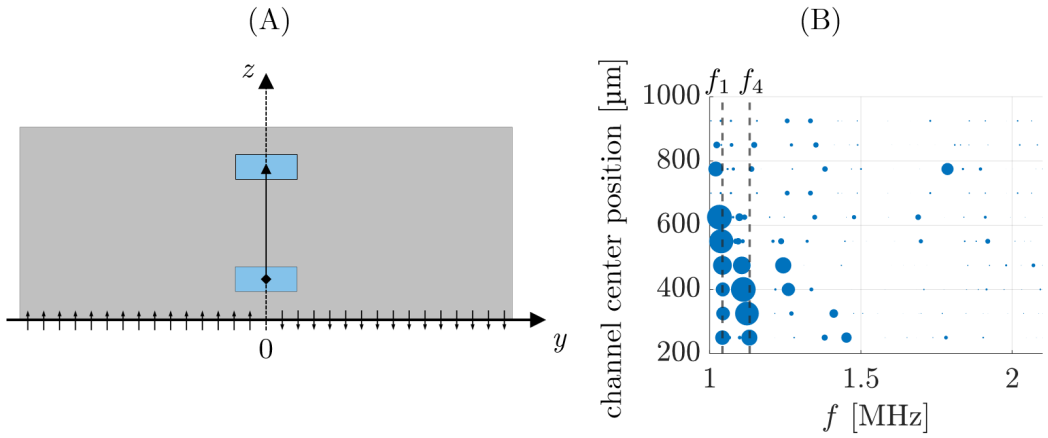

Figure 5.10: (A) Sketch of how the channel center position is varied between $z = 250\,\mu\text{m}$ and $z = 925\,\mu\text{m}$ in steps of 75 µm. (B) Resonance plot weighted to the acoustic energy density and figure of merit. Each point correspond to a resonance at the given channel center position and the size of each point is proportional to $\tilde{E}_{\text{ac}}$. Large points means good acoustophoretic properties.

From Fig. 5.10.(B) it seems some of the resonances are robust to changes in the channel center position. This is indicated as two dashed lines at the frequencies $f_1 = 1.042\,\text{MHz}$ and $f_4 = 1.132\,\text{MHz}$, which also turned out to be the best resonances in the reference setup. The resonance at 1.042 MHz tends to lower its resonance frequency as the channel center position relocates towards the top. This resonance has an optimum at a channel center position $z = 625\,\mu\text{m}$, going from $E_{\text{ac}} = 7.14\,\text{Pa}$ at reference to $E_{\text{ac}} = 16\,\text{Pa}$ at frequency 1.032 MHz, slightly below 1.042 MHz.

The same can be said about the reference resonance at 1.132 MHz; here the optimum channel position is $z = 400\,\mu\text{m}$ at frequency 1.11 MHz also slightly below the reference frequency. The acoustic energy goes from $E_{\text{ac}} = 7.14\,\text{Pa}$ to $E_{\text{ac}} = 17\,\text{Pa}$.

To assess if the resonances are robust to changes, the different resonances are compared to the reference system in Fig. 5.11. Even though the resonances are close in frequency the qualitative displacement behaviour are far from the same.

However, in Fig. 5.12 the different geometries (different channel positions) seems to yield the same qualitative behaviour. Both resonances have the same rolls in the top corners and almost the same displacement at the side edges. This is evidence of a robust resonance in the sense that one can move the channel around and still get the same acoustic behaviour.

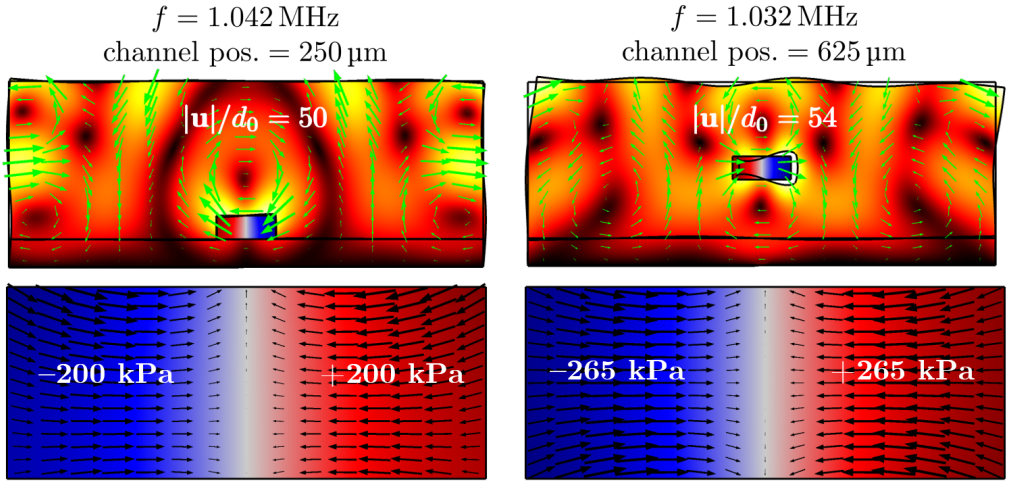

Figure 5.11: Left column: reference device resonance at 1.042 MHz with displacement field and acoustic pressure field together with the radiation force. Right column: resonance at $f = 1.032\,\text{MHz}$ with channel position $z = 625\,\mu\text{m}$. The displacement magnitude ranges from 0 (dark) to 54 (light) and the acoustic pressure is from -265 kPa (red) to 265 kPa (blue) symmetric around zero (gray).

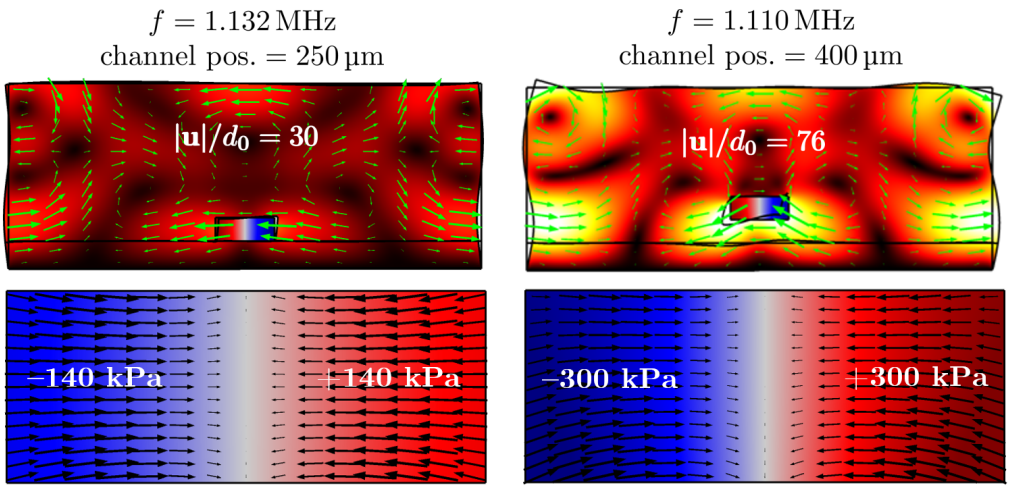

Figure 5.12: Left column: reference device resonance at 1.132 MHz with displacement field and acoustic pressure field together with the radiation force. Right column: resonance at $f = 1.110\,\mathrm{MHz}$ with channel position $z = 400\,\mu\mathrm{m}$. The displacement magnitude ranges from 0 (dark) to 76 (light) and the acoustic pressure is from -300 kPa (red) to 300 kPa (blue) symmetric around zero (gray).

5.6 Summary of the main results

This chapter offers a summary of acoustophoretic properties in both soft and hard materials. It also provides an insight in the properties of designing an acoustic microfluidic device used for acoustophoresis. Most importantly it also predicts the relative cheap material PMMA to be a descent choice of material in designing acoustofluidic devices. The different parametric studies is examples of how to optimise such devices. This showed how alternatives to the base height and channel position, could yield energies comparable to the Pyrex device.

The sweeping method where the resonances are weighted according to $\tilde{E}_{\mathrm{ac}}$ seems to be a good way to predict good acoustophoresis, but should always be accompanied with a full assessment of the fields.

Chapter 6

Acoustic streaming

First order acoustics has now been investigated in both hard and soft acoustofluidic devices motivated by acoustophoresis. Now we turn to the second order time-averaged acoustics, focusing on the PMMA device.

6.1 Introduction to acoustic streaming

For high amplitude acoustics some interesting steady phenomena occurs, and by going to second order perturbation theory one can establish successive approximations to understand these phenomena. As touched upon, the second order fields contains both steady and non-steady parts. The focus will be on the time-averaged steady effects. The high amplitude acoustic can be obtained by a high amplitude source or by tuning in on resonance, where the latter will be of interest in this case.

The first order acoustic fields serves as source terms to the second order fields and for the time-averaged second order velocity the convected momentum density governs the second order acoustics. The first theoretical study of acoustic streaming was carried out by Rayleigh. He gave an analysis to the boundary layer driven acoustics, with the remarkable property that the second order streaming is independent of viscosity but originates from this [19].

The Rayleigh streaming can be written as a boundary condition to the long ranged second order velocity field $\mathbf{v}_2^d$ as

$$\mathbf{v}_2^d(y, z=0) = \frac{3}{8}\frac{v_a^2}{c_0}\sin(2k_0 y)\hat{\mathbf{e}}_y = v_{\mathrm{R}}\sin(2k_0 y)\hat{\mathbf{e}}_y. \tag{6.1.1}$$

Here the no-slip boundary is located at $z = 0$. For a standing acoustic pressure wave the Rayleigh streaming amplitude can be written in terms of the acoustic energy density

$$v_{\mathrm{R}} = \frac{3}{2}\frac{E_{\mathrm{ac}}}{\rho c_0}. \tag{6.1.2}$$

This boundary condition is an effective way of describing the slip velocity due to the acoustic Reynolds stress inside the boundary layer. It turns out that acoustic streaming can be driven not only by the boundary layer but also by bulk attenuation, known as Eckart streaming. This kind of streaming is proportional to the damping Γ_{fl} [20]. The Eckart streaming can be observed when a travelling plane wave (fluid jet) gets attenuated and steady vortices begins to appear as backflow, also known as the quartz wind.

To establish a frame of reference with regards to the streaming, a general presentation of the well-known streaming pattern of a hard-wall system will be carried out. In reality this pattern can be achieved by choosing a hard material i.e. Pyrex, and tuning in on resonance. In Fig. 6.1 such a configuration is presented for infinite hard walls, where the side walls are oscillating in-phase yielding a standing pressure wave driving the Rayleigh streaming. The hard-wall boundary condition is conventionally written as the no-slip condition on the first order velocity field

$$\mathbf{v}_1(y = \pm W_{\text{fl}}/2, z) = -\mathrm{i}\omega d_0 \hat{\mathbf{e}}_y \quad \text{and} \quad \mathbf{v}_1(y, z = \pm H_{\text{fl}}/2) = \mathbf{0}. \tag{6.1.3}$$

The fluid channel width is such that it matches the standing half-wave resonance $W_{\text{fl}} = \lambda/2$. By looking at the bulk streaming in Fig. 6.1.(A) there seems to be four streaming rolls. But turning to Fig. 6.1.(B) there also exist rolls inside the boundary layer and in total there are eight rolls. As mentioned this boundary layer streaming is modelled as an effective boundary condition when calculating the Rayleigh streaming.

To characterise the streaming, the magnitude is normalised to the Rayleigh streaming amplitude defining the non-dimensional streaming scale $\tilde{v}_2$ as

$$\tilde{v}_2 = |\mathbf{v}_2|/v_{\text{R}}. \tag{6.1.4}$$

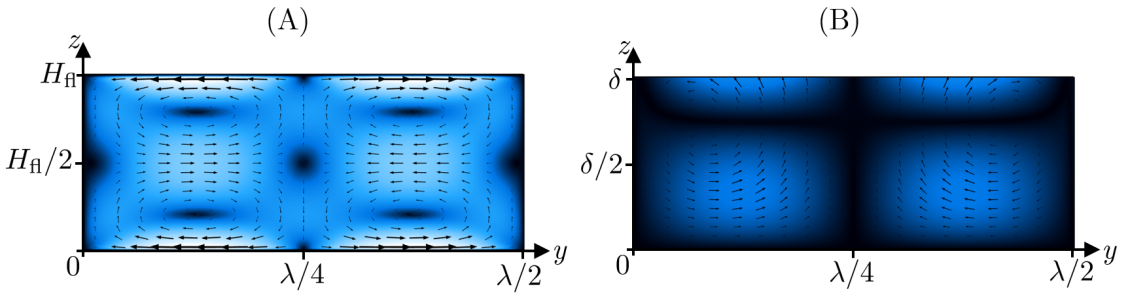

Figure 6.1: Streaming magnitude (surface plot) and vector field plot (black arrows) inside a liquid-filled channel of width $W_{\text{fl}} = \lambda/2$. The normalised streaming magnitude $\tilde{v}_2$ ranges from 0 (dark) to 1 (light). (A) Rayleigh streaming pattern in a rectangular channel. (B) Streaming pattern inside the boundary layer.

Since the viscous acoustic streaming is driven by the viscous boundary layer near obstacles, it makes the near wall region of most importance. These effects has been studied by [21,

W.L. Nyborg], where he considered perpendicular wall motions, this boundary layer theory has been further applied to arbitrary motions in Ref. [11] in the limit of weakly curved and thin boundary layers. This holds if the radius of curvature R is much larger than the boundary layer thickness δ. By virtue of the effective boundary layer condition in Eq. (2.5.15) there are effectively four fields driving the streaming; three surface fields $\mathbf{v}_1^{\delta 0}$, $\mathbf{V}_1^0$, $\mathbf{v}_1^{d0}$ and the irrotational acoustic bulk field $\mathbf{v}_1^d$ contained in the boundary condition at the wall. Here the capital $\mathbf{V}_1^0$ is the wall velocity where the lower case refers to fluid velocities.

6.2 Streaming in hard and soft acoustofluidic devices

In Chapter 5 the first order acoustic effects in both hard and soft materials were presented together with the steady acoustic radiation force. In this section the same resonances will be further investigated by including the streaming.

As mentioned the streaming is a direct consequence of the viscous boundary layer, driven by the the displaced fluid/solid interface, where the first order velocity needs to adapt over the small distance δ. This makes it interesting to compare the streaming fields for hard and soft materials, where the wall motions are qualitatively different. The focus will be on the resonances presented in Fig. 5.4.(A-B) and Fig. 5.7.(A-B) for Pyrex and PMMA respectively. These resonances turned out to be the best resonances according to the desired figure of merit and acoustic energy density.

In Fig. 6.2 the streaming patterns for the Pyrex and PMMA device is presented. Both patterns is remarkably close to classical Rayleigh streaming idealised in Fig. 6.1. However the PMMA streaming pattern is slightly different, but still qualitative the same. The streaming magnitude are also quite different, for the Pyrex device, the streaming ranges from $\tilde{v}_2 = 0$ to $\tilde{v}_2 = 1.07$ with $v_{\mathrm{R}} = 1945\,\mu\mathrm{m/s}$ very close to the ideal Rayleigh streaming presented in Fig. 6.1, where it ranges from 0 to 1.

For the PMMA device the streaming magnitude ranges from $\tilde{v}_2 = 0$ to $\tilde{v}_2 = 1.6$ with $v_{\mathrm{R}} = 4.0\,\mu\mathrm{m/s}$. Evidently there is a fundamental difference in magnitude, this is due to the idealized actuation having the same amplitude in both systems. In reality it requires more power to actuate a hard material compared to a soft. A way to circumvent this, is to use different actuation amplitudes depending on the elastic material. However, since everything scales linearly to the amplitude, the streaming patterns will be the same independent of the magnitude of the actuation—which is also the reasoning behind the normalisation in Eq. (6.1.4).

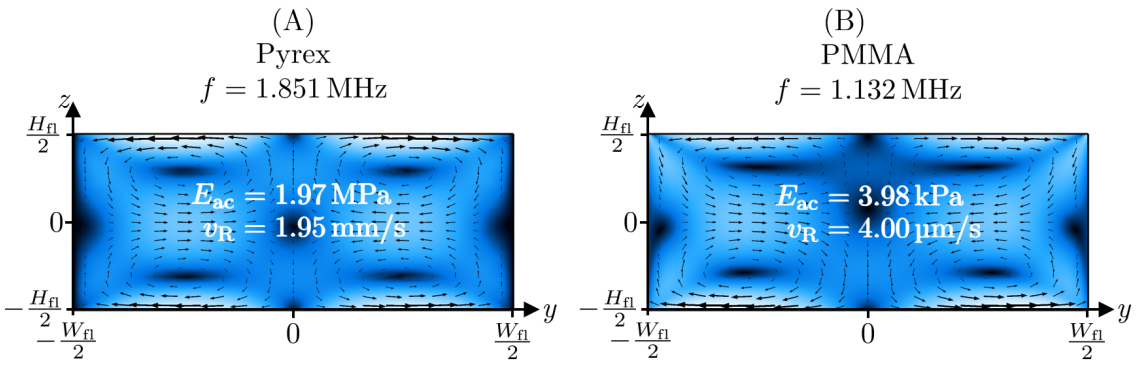

Figure 6.2: Streaming patterns for the Pyrex and PMMA device, both at the best resonance according to previous analysis. (A) Streaming pattern inside the Pyrex device. The black arrows corresponds to the vector plot of $\mathbf{v}_2$ and the surface plot corresponds to the normalised streaming $\tilde{v}_2$, ranging from 0 (dark) to 1 (light). (B) Same as (A) but for the all-polymer PMMA device. Here $\tilde{v}_2$ is plotted in the interval from 0 (black) to 1.6 (white). The acoustic energy density is indicated in each figure.

To understand the difference in the relative streaming magnitudes we consider the streaming theory of a resonant systems according to Ref. [11]. A resonant system will typically have wall velocities a factor of $Q = 1/\Gamma_{\text{fl}} \sim 1 \times 10^5$ smaller than the bulk velocity v_1^d. This means that the first order no-slip condition Eq. (2.5.8) can be approximated by $\mathbf{v}_1^{\delta 0} \approx -\mathbf{v}_1^{d0}$ yielding the parallel acoustic approximation

$$\mathbf{v}_{2\parallel}^{d0} = -\frac{3}{8\omega}\boldsymbol{\nabla}_\parallel \left|\mathbf{v}_{1\parallel}^{d0}\right|^2. \tag{6.2.1}$$

To assess this condition we consider the pressure and velocity profiles in the PMMA device along the lower fluid edge. These profiles are presented in Fig. 6.3 as solid blue curves. The profiles are compared to the usual half-wave resonance profiles (green dashed lines) $p_a \sin(k_0 y)$ and $v_a \cos(k_0 y)$ indicating quite a discrepancy.

By fitting the profiles to a new wavenumber $k_y = \alpha k_0$ we can use the α parameter to assess the waves. These phase modulated waves are indicated as red dashed lines in Fig. 6.3 corresponding to $\alpha = 1.43$. By evaluating Eq. (6.2.1) with the fitted profiles, the slip-velocity becomes

$$v_{2\parallel}^{d0} = \alpha \frac{3}{8}\frac{v_a^2}{c_0}\sin(2\alpha k_0 y)\hat{\mathbf{e}}_y. \tag{6.2.2}$$

Apart from the pre-factor α and the modulated phase it is equivalent to the Rayleigh boundary velocity i.e. $v_{2\parallel}^{d0} = \alpha v_{\text{R}} \sin(2\alpha k_0 y)$. This can explain the small departure from v_{R} in Fig. 6.2.(B), where the maximum streaming yielded $1.6 v_{\text{R}}$ close to the modulated amplitude $\alpha v_{\text{R}} = 1.35 v_{\text{R}}$.

So in general small variations to the usual half-wave resonance will yield different streaming magnitudes, compared to the standard hard-wall Rayleigh streaming where $\max(|\mathbf{v}_2|/v_\mathrm{R}) = 1$. Furthermore the parallel wavenumber k_y is a factor of α larger than k_0 and from the relation

$$k_0 = \sqrt{k_y^2 + k_z^2}, \tag{6.2.3}$$

the perpendicular wavenumber k_z must be purely imaginary indicating some kind of perpendicular damping.

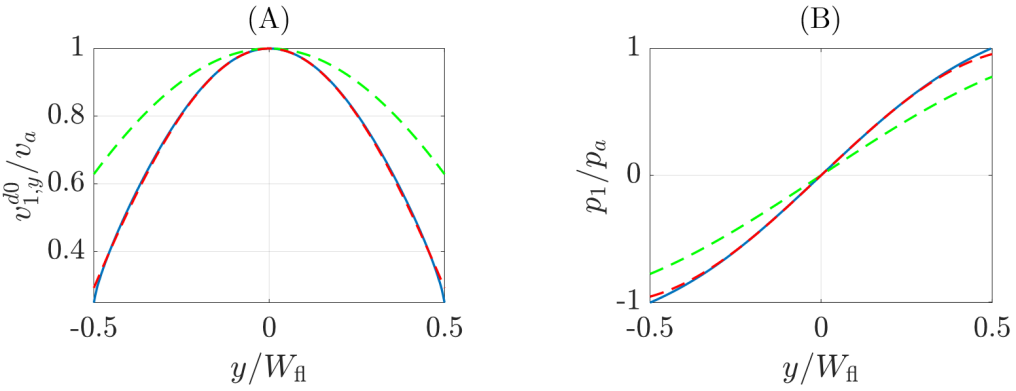

Figure 6.3: (A) Parallel velocity component (solid blue line) evaluated on the lower fluid edge and normalised to $v_a = 14.3\,\mathrm{cm/s}$, together with the standard half-wave resonance $\cos(k_0 y)$ (green dashed line) and a modulated wave $\cos(\alpha k_0 y)$ (red dashed line) with $\alpha = 1.43$. (B) Same as in (A) but for the pressure with $p_a = 142\,\mathrm{kPa}$ and sine waves instead of cosine.

6.2.1 Particles affected by streaming in a PMMA device

In Chapter 5 we showed how the acoustic pressure can focus particles under the right resonance condition due to the time-averaged radiation force. In previous chapters the radiation force was the only force acting on the suspended particles. In a more elaborate model the acting forces are of course not only the radiation force, but also buoyancy $\mathbf{F}_\mathrm{buoy}$ and drag $\mathbf{F}_\mathrm{drag}$. Like the acoustic radiation force, the buoyancy also scales with the particle volume a^3

$$\mathbf{F}_\mathrm{buoy} = \frac{4\pi}{3} a^3 \left(\tilde{\rho} - 1\right) \rho_0 \mathbf{g}. \tag{6.2.4}$$

These forces are two examples of volume forces, whereas the drag scales with the radius. For small Reynolds number the viscous drag will be that of Stokes drag caused by the relative motion of the fluid. The steady drag on a particle with velocity $\mathbf{v}_\mathrm{p}$ is therefore a consequence of the acoustic streaming $\mathbf{v}_2$

$$\mathbf{F}_\mathrm{drag} = 6\pi\eta_0 a \left(\mathbf{v}_2 - \mathbf{v}_\mathrm{p}\right). \tag{6.2.5}$$

From these equations it is evident how the streaming induced drag becomes pronounced as the particle gets smaller, essentially working against the focusing acoustophoretic behaviour. The critical particle radius at which the streaming becomes dominant has been studied in Ref. [15] and turns out to be $a_{\mathrm{cr}} \approx 1\,\mu\mathrm{m}$ at 2 MHz. Particles with radius smaller than a_{cr} will therefore be mixed by streaming. This can be understood by scaling the acting forces.

Most often we use polystyrene tracer particles to model the particle motions with material parameters given in Table A.2. The density is $\rho_{\mathrm{ps}} = 1050\,\mathrm{kg/m^3}$, which makes the particles almost neutrally buoyant since $\tilde{\rho} \approx 1$ and the buoyancy becomes negligible compared to $\mathbf{F}_{\mathrm{rad}}$ and $\mathbf{F}_{\mathrm{drag}}$.

At half-wave resonance the radiation force is calculated in Eq. (2.3.27) and the streaming magnitude can be written in terms of the acoustic energy as in Eq. (6.1.2) so the scaling between the drag and acoustic radiation force becomes

$$\frac{|\mathbf{F}_{\mathrm{rad}}|}{|\mathbf{F}_{\mathrm{drag}}|} = \frac{4}{9}\Phi_{\mathrm{ac}}\frac{a^2\omega}{\nu_0}. \tag{6.2.6}$$

For polystyrene particles in water at 2 MHz the critical radius becomes

$$a_{\mathrm{cr}} = \frac{3}{2}\sqrt{\frac{\nu_0}{\Phi_{\mathrm{ac}}\omega}} = \frac{3}{2}\frac{\delta}{\sqrt{2\Phi_{\mathrm{ac}}}} \approx 1\,\mu\mathrm{m} \tag{6.2.7}$$

the calculation uses the values in Table A.2. It is noteworthy to see how the critical radius is proportional to the boundary layer thickness.

A particle located in the pressure nodal plane with $\mathbf{F}_{\mathrm{rad}} = \mathbf{0}$ will of course sediment over time due to buoyancy. The time it takes to sediment in a channel with height $H_{\mathrm{fl}} = 150\,\mu\mathrm{m}$ can be estimated by equating drag and buoyancy

$$t_{\mathrm{sed}} = \frac{9}{2}\frac{\nu_0}{a^2\left(\tilde{\rho}-1\right)g}H_{\mathrm{fl}} \approx 46\,\mathrm{s}. \tag{6.2.8}$$

The sedimentation time should be compared with the time it takes to focus particles t_{focus}. This time scale can be estimated by equating drag and radiation force, thereby estimating the particle speed v_{p} as

$$v_{\mathrm{p}} = \frac{|\mathbf{F}_{\mathrm{rad}}|}{6\pi\eta_0 a} = \frac{2}{3}\Phi_{\mathrm{ac}}\frac{a^2 k_0 E_{\mathrm{ac}}}{\eta_0}\sin(2k_0 y). \tag{6.2.9}$$

For a channel of width W_{fl} with side walls at $y = 0$ and $y = W_{\mathrm{fl}}$, the focusing time is

$$t_{\mathrm{focus}} = \frac{3}{4}\frac{\eta_0}{\Phi_{\mathrm{ac}}a^2k_0^2E_{\mathrm{ac}}}\ln\left[\frac{\tan(2k_0y(t))}{\tan(2k_0y(0))}\right]. \tag{6.2.10}$$

For a typical hard-wall system, similar to the one considered in this thesis, the acoustic energy density has been measured in Ref. [22, 23] and is in the order of $E_{\mathrm{ac}}{\sim}20\,\mathrm{Pa}$. In

this case the distance it takes for a 5-µm-radius polystyrene tracer particle to move from $y(0) = W_{\text{fl}}/8$ to $y(t) = 3W_{\text{fl}}/8$ at $f = 2\,\text{MHz}$ is

$$t_{\text{focus}} \approx \frac{6}{4}\frac{\eta_0}{\Phi_{\text{ac}} a^2 k_0^2 E_{\text{ac}}} = 0.22\,\text{s}. \tag{6.2.11}$$

The time it takes to focus a particle happens much faster than sedimentation. These equations is actually used to measure the acoustic energy density at resonance. Either by particle tracking or by measuring the time it takes to focus particles, since all other parameters are known.

There is another time scale which is perhaps even more important for acoustophoretic applications, that is the flow rate in the length direction. Here the particles must get focused before arriving at mid-channel. The typical length of a device used by AcouSort is $L_{\text{fl}} = 40\,\text{mm}$ by these means we can calculate a critical flow rate

$$Q_{\text{cr}} = \frac{A_{\text{fl}} L_{\text{fl}}}{2t_{\text{focus}}} = 5.15\,\mu\text{L/s}. \tag{6.2.12}$$

this sets an upper limit for the throughput for a acoustophoresis at $E_{\text{ac}} = 20\,\text{Pa}$.

Now we have established the acting forces and the characteristic time scales. This leads to numerical implementation of particle tracing solving Newtons second law for the particle position $\mathbf{r}_{\text{p}}$ i.e.

$$m_{\text{p}}\frac{\text{d}^2\mathbf{r}_{\text{p}}}{\text{d}t^2} = \mathbf{F}_{\text{rad}} + \mathbf{F}_{\text{drag}} + \mathbf{F}_{\text{buoy}}. \tag{6.2.13}$$

For small particle-Reynolds number the inertial effects can be ignored and since the 5-µm-radius polystyrene particles can be considered neutral buoyant the particle force balance reads

$$\mathbf{v}_{\text{p}} = \mathbf{v}_2 + \frac{\mathbf{F}_{\text{rad}}}{6\pi\eta_0 a}. \tag{6.2.14}$$

One example of particle trajectories is given in Fig. 6.4 for the PMMA device at resonance $f = 1.132\,\text{MHz}$ equivalent to the one presented in Fig. 5.7.(A-B) and Fig. 6.2 with acoustic energy density $E_{\text{ac}} = 3.97\,\text{Pa}$. The particle properties is again that of 5-µm polystyrene tracer particles with parameters given in Table A.2. This amount to the focus time $t_{\text{focus}} = 3.4\,\text{s}$ according to Eq. (6.2.11) and critical radius $a_{\text{cr}} = 2.2\,\mu\text{m}$ according to Eq. (6.2.7).

To analyse the particle size dependence towards the particle motion in the PMMA device, particles with different radii are released at time $t = 0\,\text{s}$ and captured at times $t = 0.5t_{\text{focus}}$, $t = t_{\text{focus}}$ and $t = 2t_{\text{focus}}$ as shown in Fig. 6.4. From these trajectories it is obvious how the radiation force dominates for both $a = 5\,\mu\text{m}$ and $a = 3\,\mu\text{m}$, but when the particle radius gets below the critical radius $a = 1\,\mu\text{m}$ the streaming begins to dominate and instead of focusing the particles are mixed.

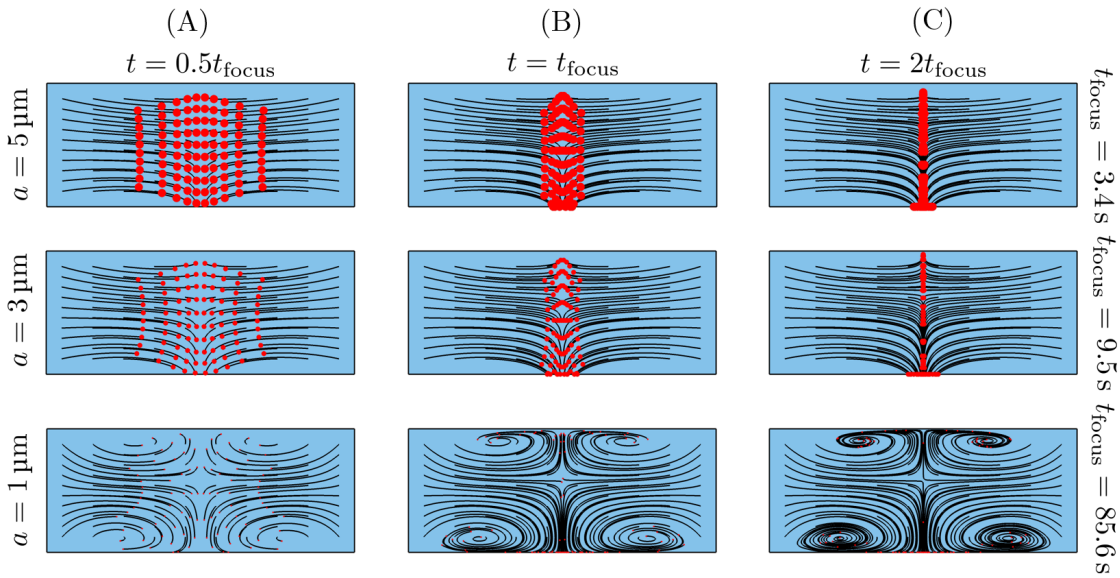

Figure 6.4: Particle (red spheres) trajectories (black lines) captured at different times $0.5t_{\text{focus}}$, t_{focus} and $2t_{\text{focus}}$. Each row of pictures correspond to different particle radii a; 1 µm, 3 µm and 5 µm respectively, thereby also different focusing time scales t_{focus}; 3.4 s, 9.5 s and 85.6 s.

In the light of acoustophoresis and particle focusing the streaming is unwanted when handling particles below 1 µm in radius e.g. bacteria, exosomes and viruses. This sets a strong motivation to study how the streaming can be diminished and suppressed. One approach is to use an inhomogeneous fluid, which has been studied in Ref. [24, 25]. It turns out that inhomogeneities in both compressibility and density will results in a non-dissipative force density, both altering and suppressing the streaming.

6.3 Hard microchannels with soft thin lids

Our Swedish colleagues from the Department of Biomedical Engineering at Lund University, suggested to use a device comprising a hard base and a soft lid enclosing the fluid channel. As another approach to suppress the streaming and at the same time having good acoustophoretic properties.

To achieve such system they use an aluminum block as a base and the soft polymer PDMS as the lid material. The device consist of a piezoelectric PZT transducer mounted underneath an aluminium base bonded with super glue. The 3D setup is sketched in Fig. C.1 together with a top view. The cross-sectional 2D principal sketch is shown in Fig. 6.5.

The 20-µm PDMS lid is spin coated and bonded to the aluminium by exposing it to air plasma. The fluid channel is micromilled inside the aluminum block. This procedure does not require any clean-room techniques, which makes it cheaper and easier to get a hold on.

This device is further motivated by rapid prototyping plus the fact that aluminium and PDMS are abundant and cheap materials.

The numerical model will concern the two-dimensional cross-section sketched in Fig. 6.5 with dimensions in Table 6.1. This section will serve as an preliminary study to support and consult our colleagues in the laboratory, essentially verifying our numerical model against experimental observations.

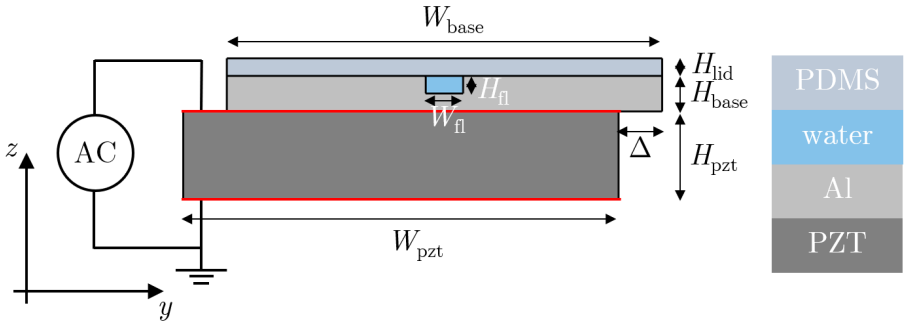

Figure 6.5: Cross-sectional view of the aluminum-PDMS device used at the Department of Biomedical Engineering at Lund University by Ph.D. student J. Lei. The dimensions is given in Table 6.1. The electrodes are marked by two red lines, one is grounded (bottom) and the other (top) is coupled to an alternating signal with peak to peak amplitude $\phi_0 = 10\,\text{V}$.

Table 6.1: aluminium-PDMS device dimensions.

Parameter	base	lid	pzt	fluid (fl)	Unit
Width, W_{i}	5000	5000	5000	430	µm
Height, H_{i}	400	20	1000	200	µm

In this model the piezoelectric transducer will be included, coupling the mechanical displacement field to the electric potential illustrated in Eq. (2.4.16). In the given setup they use the lead-zirconate-titanate (PZT-Pz26) ceramic with material parameters given in Table A.4 extracted from Ref. [26]. Due to the high electric permittivity of Pz26 the electric potential is assumed to be confined to the transducer and by assuming no free charges the electrical potential satisfies the quasi-static equation

$$\boldsymbol{\nabla} \cdot \mathbf{D} = 0. \tag{6.3.1}$$

In order to excite both asymmetric and symmetric resonances the transducer is placed asymmetrically, in this case by an amount $\Delta = 1.0\,\text{mm}$ as sketched in Fig. 6.5. The bottom will work as a grounded electrode and the electrode between the base and the PZT will be coupled to an alternating signal. These electrodes will serve as boundary conditions to the quasi-static equation

$$\phi(\mathbf{r},t) = \begin{cases} \phi_0(\mathbf{r})\mathrm{e}^{-\mathrm{i}\omega t} & \text{top electrode,} \\ 0 & \text{bottom electrode,} \end{cases} \tag{6.3.2}$$

where $\phi_0 = 10\,\text{V}$. Since it is a constraint on the potential field itself this boundary condition is implemented as a Dirichlet boundary condition in COMSOL.

6.3.1 Comparison to experimental observations

To find the resonances the acoustic energy is probed from 1.8 MHz to 2.8 MHz, this is the frequency domain at which the experiment was observed. The numerical procedure is as follows

1. Probe the acoustic energy in the given frequency range.
2. Pick out the frequency at which the acoustic energy inside the fluid channel peaks.
3. Choose the best resonance according to the weighted acoustic energy density Eq. (5.3.3).

According to the procedure we find the best resonance at frequency $f = 2.235\,\text{MHz}$. Remarkably close to the observations made in Lund by Ph.D. student J. Lei and postdoc W. Qiu, where they found the best focusing properties at 2.24 MHz. The other resonance properties are tabulated in Table B.3.

The 5-µm-radius polystyrene tracer particles were tracked using the general-defocusing-particle-tracking (GDPT) method, measuring the particle trajectories [27]. To compare the simulations with observations made in the laboratory, the numerically calculated radiation force is compared to the measured velocities, since the radiation force will dominate the particle motion. This is shown in Fig. 6.6.

The measured particle velocity field in Fig. 6.6.(A) tends to focus the particles towards the pressure node at $y \approx 0$, however a vertical velocity component tends to force the particles towards the PDMS lid in the positive z-plane strongest above $z = 0$. At $z \approx -H_{\text{fl}}/4$ (marked by the white dashed line) there is a transition from negative to positive vertical component. Furthermore there seems to be exceptional forces at the top corners. These tendencies are also captured in our numerical simulations as shown in Fig. 6.6.(B).

In the simulations the PZT offset relocates the pressure nodal plane slightly to the right, this however does not seems to be the case for the measured velocity profiles.

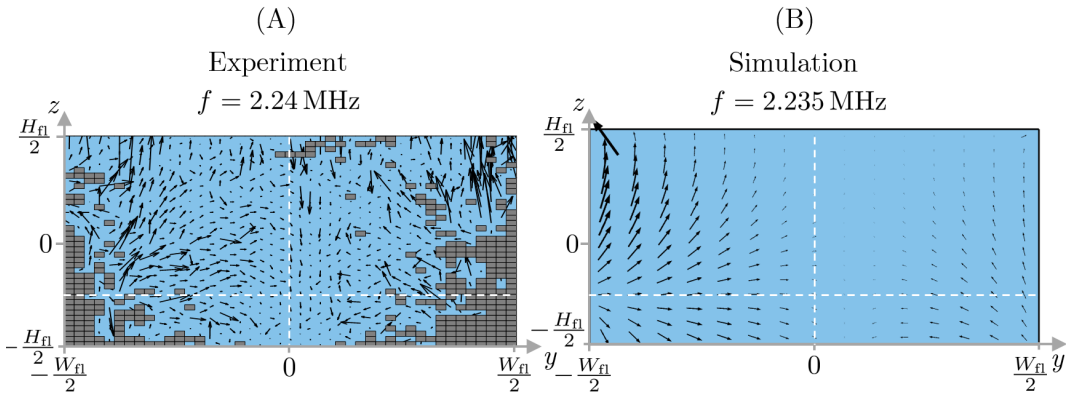

Figure 6.6: (A) GDPT measurement inside the water filled cavity for the aluminum-PDMS device, showing the particle velocity field. (B) Numerical calculated radiation force (cyan arrows) for the aluminum-PDMS device at resonance $f = 2.235\,\mathrm{MHz}$.

The acoustic radiation force field for the aluminium-PDMS device is very different from the homogeneous devices presented in Chapter 5. The streaming pattern presented in Fig. 6.7 turns out to be very complicated as well. The streaming is dominant in the top corners where it reaches its maximum value $\tilde{v}_2 = 235$ corresponding to $235 v_{\mathrm{R}} = 129\,\mu\mathrm{m/s}$. For conventional hard system the typical acoustic energy density is in the order of 20 Pa this corresponds to a Rayleigh streaming amplitude of $20\,\mu\mathrm{m/s}$. So even though the Rayleigh streaming amplitude in the Al-PDMS system is low $v_{\mathrm{R}} = 0.55\,\mu\mathrm{m/s}$ compared to conventional values, the streaming in the corners seems to exceed the conventional value five times.

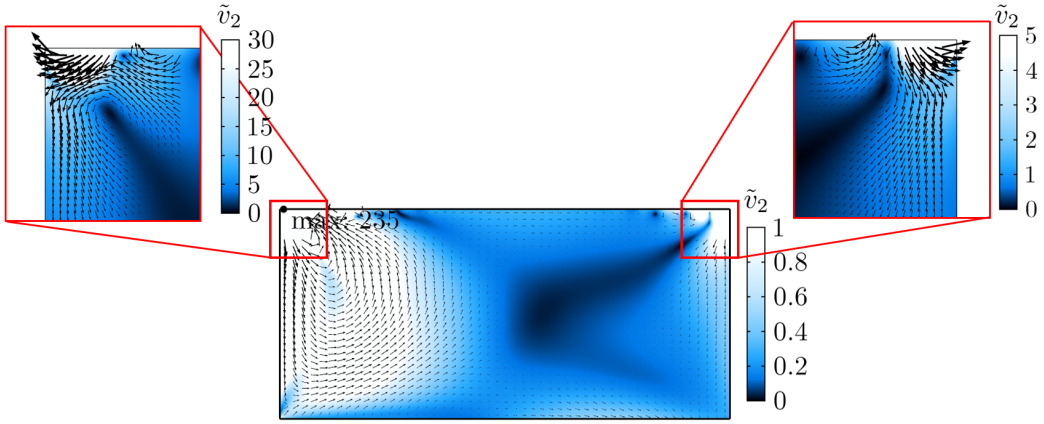

Figure 6.7: Acoustic streaming for the Al-PDMS with lid height $H_{\mathrm{lid}} = 20\,\mu\mathrm{m}$ at resonance frequency $f = 2.235\,\mathrm{MHz}$. The streaming magnitude is normalised to the Rayleigh streaming magnitude, in this case $v_{\mathrm{R}} = 0.55\,\mu\mathrm{m/s}$. The top corners is resolved on another scale which is indicated in the figure. The arrow length is logarithmic scaled.

6.3.2 PDMS lid size and streaming patterns

To assess this special behaved streaming due to the soft lid, the lid thickness is varied whereas the streaming patterns for chosen lid thickness will be investigated. For each value of the lid size the above numerical procedure is performed.

In Fig. 6.8 streaming patterns at different lid thickness is shown together with characteristic streaming values. Clearly the acoustophoresis is optimal at $H_{\text{lid}} = 150\,\mu\text{m}$. Here the streaming patterns seems to have some of the same features as for the classical Rayleigh streaming, but still dominated by the top corners. Nevertheless the complex behaved streaming at the top corners seems to persist even though the lid thickness becomes comparable to the base thickness. This is evidence of a material dependence and not an effect due to the thin lid.

The distinctive transverse speed of sound $c_t = 66.3\,\text{m/s}$ for the modelled PDMS (RTV-615) measured in Ref. [28, 29], could very well be the reason behind this complex behaved streaming.

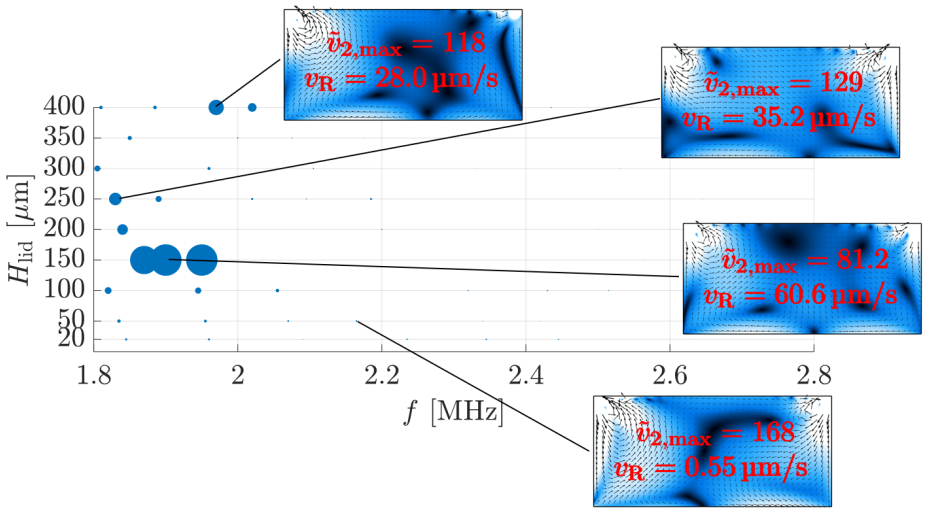

Figure 6.8: Resonance plot weighted by the acoustic energy density and figure of merit. Each point correspond to a resonance at a given lid thickness and the size of each point is proportional to $\tilde{E}_{\text{ac}}$ i.e. a large point means good acoustophoretic properties. For chosen resonances the streaming patterns are shown together with characteristic scales in the color range 0 (dark) to 1 (light) in terms of $\tilde{v}_2$. The streaming arrow length is logarithmic scaled.

6.3.3 Artificial polymer alloy

To assess if the distinctive material parameters for the given PDMS could be the reason behind the complex motions in the corners, we artificially change the material parameters towards that of PMMA.

To do so, we define a parameter μ which describes the "amount" of PMMA e.g. $\mu = 0.1$ correspond to 10% PMMA and 90% PDMS—this is not realistic but can be used to identify and characterise the problem. In Fig. 6.9 a sweep in the polymer ratio parameter μ is calculated. For each value the ratio θ between the corner streaming to the total streaming is calculated, according to

$$\theta = \frac{\int_{\text{corners}} |\mathbf{v}_2| \, \mathrm{d}A}{\int_{\text{fluid domain}} |\mathbf{v}_2| \, \mathrm{d}A}. \tag{6.3.3}$$

The corners are defined as the magenta squares in Fig. 6.9.(B).

Already at $\mu = 0.05$ the streaming at the top corners has decreased to the converged value at a streaming ratio of 18% (dashed line). This corresponds to the the material parameters $\rho_0 = 1027.5\,\mathrm{kg/m^3}$, $c_\mathrm{t} = (271.2 - \mathrm{i}3.583)\,\mathrm{m/s}$ and $c_\mathrm{l} = (1172 - \mathrm{i}1.954)\,\mathrm{m/s}$, where the complex valued speed of sounds accounts for the attenuation of sound waves. The streaming pattern is still very complex, but now it is driven by the entire lid and not the corners.

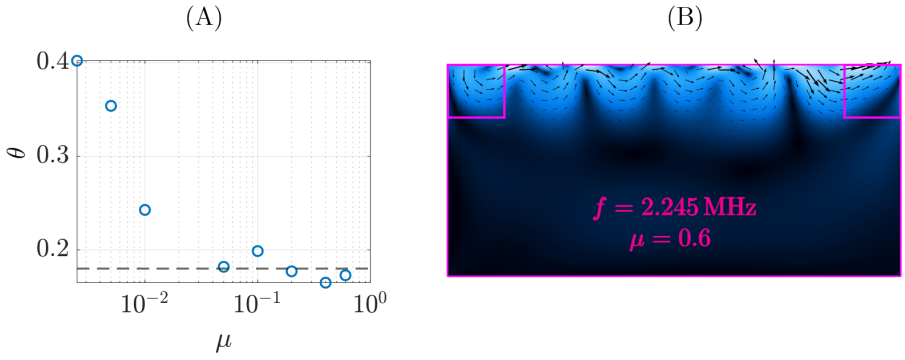

Figure 6.9: (A) Streaming ratio at different polymer ratios on a semilog scale. (B) Converged streaming pattern at $\mu = 0.6$.

PDMS comes in different variants and for the given system we are using the RTV-615 material parameters [28, 29]. The validity of a numerical study is always limited by the uncertainty on the material parameters. Doing numerical simulations accompanied with measurements, best practice requires determination of the material parameters for the specific device at hand, this goes for all systems and not only the Al-PDMS device. This numerical analysis together with the measurements has resulted in two abstracts submitted to the AcoustoFluidics conference 2019, third authoring Ref. [30] and first authoring Ref. [31].

Chapter 7

Viscoelastic acoustofluidics

Now we turn to model the fluid as a viscoelastic material. As described in Section 2.6 viscoelastic fluids can be considered as non-Newtonian. These fluids behaves both elastically and viscous, which makes them complicated to characterise. In this chapter periodic disturbances will be applied on a viscoelastic fluid comprising viscoelastic acoustofluidics. The viscoelastic effects are most pronounced within the time-averaged second order effects as pointed out in Ref. [13]. That is why this chapter will mainly concern the steady second order fields i.e. viscoelastic acoustic streaming.

7.1 Viscoelastic Rayleigh streaming

To get an understanding of how the streaming is affected by a viscoelastic behaved material, the classical Rayleigh streaming is approached with the viscoelastic model presented in Section 2.6.

Consider the situation where the far-field $\mathbf{v}_1^d$ takes the irrotational form of a standing wave with wavenumber k_0

$$\mathbf{v}_1^d = v_1^{d0} \cos(k_0 y) \hat{\mathbf{e}}_y, \tag{7.1.1}$$

above a stationary planar wall at $z = 0$ parallel to the (x, y)-plane. The half-space $z > 0$ is filled with a viscoelastic fluid.

From this a Helmholtz decomposition is constructed

$$\mathbf{v}_1 = \mathbf{v}_1^d + \mathbf{v}_1^\delta \quad \text{with} \quad \boldsymbol{\nabla} \times \mathbf{v}_1^d = \mathbf{0} \quad \text{and} \quad \boldsymbol{\nabla} \cdot \mathbf{v}_1^\delta = 0, \tag{7.1.2}$$

similar to the effective boundary layer theory.

According to Eq. (2.6.9) the viscoelastic Navier–Stokes equation reads

$$-\mathrm{i}\omega\rho_0 \mathbf{v}_1 = -\boldsymbol{\nabla} p_1 + \eta(\omega) \left[\nabla^2 \mathbf{v}_1 + \boldsymbol{\nabla} \left(\boldsymbol{\nabla} \cdot \mathbf{v}_1 \right) \right], \tag{7.1.3}$$

by taking the curl of Eq. (7.1.3) a single equation for $\mathbf{v}_1^\delta$ appears

$$\boldsymbol{\nabla} \times \left(-\mathrm{i}\omega\rho_0 \mathbf{v}_1^\delta - \eta(\omega)\nabla^2 \mathbf{v}_1^\delta \right) = \mathbf{0} \tag{7.1.4}$$

and the Helmholtz equation can be read off

$$\nabla^2 \mathbf{v}_1^\delta = -\mathrm{i}\frac{\omega\rho_0}{\eta(\omega)}\mathbf{v}_1^\delta = -2\mathrm{i}\frac{1-\mathrm{i}\omega\lambda}{\delta^2}\mathbf{v}_1^\delta. \tag{7.1.5}$$

From the scaling arguments $\partial_y \sim k_0$ and $\partial_z \sim 1/\delta$ the Laplacian can be approximated by $\nabla^2 \sim \partial_z^2$, and the y-component of Eq. (7.1.5) becomes

$$\partial_z^2 v_{1,y}^\delta = -\mathrm{i}\frac{\omega\rho_0}{\eta(\omega)} v_{1,y}^\delta = -2\mathrm{i}\frac{1-\mathrm{i}\omega\lambda}{\delta^2} v_{1,y}^\delta. \tag{7.1.6}$$

A solution satisfying $v_{1,y}^\delta \to 0$ when $z \to \infty$ together with the no-slip condition $\mathbf{v}_1(y,0) = \mathbf{0}$ is

$$v_{1,y}^\delta(y,z) = -v_1^{d0}\cos(k_0 y)\mathrm{e}^{-p\frac{z}{\delta}}\mathrm{e}^{\mathrm{i}q\frac{z}{\delta}}, \tag{7.1.7}$$

where

$$p = \sqrt{\sqrt{\omega^2\lambda^2+1} - \omega\lambda} \quad \text{and} \quad q = \sqrt{\sqrt{\omega^2\lambda^2+1} + \omega\lambda}. \tag{7.1.8}$$

The z-component can be calculated via the incompressible condition $\partial_z v_{1,z}^\delta = -\partial_y v_{1,y}^\delta$ and the no-slip condition $v_{1,z}^\delta(y,0) = 0$, which yields

$$v_{1,z}^\delta(y,z) = \frac{v_1^{d0}}{p-\mathrm{i}q}\delta k_0 \sin(k_0 y)\left(\mathrm{e}^{-p\frac{z}{\delta}}\mathrm{e}^{\mathrm{i}q\frac{z}{\delta}} - 1\right). \tag{7.1.9}$$

The full solution for a standing bulk wave $\mathbf{v}_1^d$ above a planar rigid wall at $z = 0$ reads

$$v_{1,y} = v_1^{d0}\cos(\xi)\left[1 - f(\zeta)\right] \tag{7.1.10a}$$

$$v_{1,z} = -\frac{p+\mathrm{i}q}{p^2+q^2} v_1^{d0}\delta k_0 \sin(\xi)\left[1 - f(\zeta)\right], \tag{7.1.10b}$$

where $\xi = k_0 y$, $\zeta = z/\delta$ and $f(\zeta) = \mathrm{e}^{-p\zeta}\mathrm{e}^{\mathrm{i}q\zeta}$.

In the viscous limit of zero relaxation time both p and q reduces to unity and the first order solutions reduces to the Newtonian expressions for a standing bulk wave and a stationary planar wall at $z = 0$. In the elastic limit where $\mathrm{De} \to \infty$ the coefficients will become $p \to 0$ and $q \to \infty$. Looking at the expressions in Eq. (7.1.10) the wave will become more shear like since the shear damping parameter p turns to zero, which is exactly the elastic limit.

To second order in the viscoelastic convected Jeffrey's model things becomes much more complicated due to the inclusion of the upper-convected time derivative in the Navier–Stokes equation. According to Eq. (2.6.11) the short-ranged part of the second order

viscoelastic Navier–Stokes equation reads

$$\begin{aligned}\eta_0\nabla^2\mathbf{v}_2^\delta =&\rho_0\boldsymbol{\nabla}\cdot\left\langle\mathbf{v}_1\mathbf{v}_1-\mathbf{v}_1^d\mathbf{v}_1^d\right\rangle\\&+\lambda\boldsymbol{\nabla}\cdot\left[\left\langle\left(\mathbf{v}_1^\delta\cdot\boldsymbol{\nabla}\right)\boldsymbol{\tau}_1\right\rangle-\left\langle\boldsymbol{\tau}_1\cdot\boldsymbol{\nabla}\mathbf{v}_1^\delta\right\rangle-\left\langle\left(\boldsymbol{\nabla}\mathbf{v}_1^\delta\right)^T\cdot\boldsymbol{\tau}_1\right\rangle\right].\end{aligned}\tag{7.1.11}$$

Using $\nabla^2\approx\partial_z^2$ it becomes a matter of rigorous integration*. In the end the y-component of the short-ranged second order field becomes

$$v_{2,y}^\delta=-\frac{3}{8}\frac{\left(v_1^{d0}\right)^2}{c_0}\sin(2k_0y)f(\lambda,\omega,\rho_0,\eta_0,c_0),\tag{7.1.12}$$

where the function $f(\rho_0,\lambda,\omega,\eta_0)$ is a viscoelastic correction to the classical Rayleigh streaming. This short-ranged field provides a slip boundary condition for the long ranged field $\mathbf{v}_2^d$ in order to fulfil the no-slip condition $\mathbf{v}_2(y,0)=\mathbf{v}_2^d(y,0)+\mathbf{v}_2^\delta(y,0)=\mathbf{0}$ so

$$\begin{aligned}v_{2,y}^d(y,0)=-v_{2,y}^\delta(y,0)&=\frac{3}{8}\frac{\left(v_1^{d0}\right)^2}{c_0}\sin(2k_0y)f(\lambda,\omega,\rho_0,\eta_0,c_0)\\&=v_\mathrm{R}\sin(2k_0y)f(\lambda,\omega,\rho_0,\eta_0,c_0).\end{aligned}\tag{7.1.13}$$

The function f is written in Appendix D and plotted in Fig. 7.1.

In the ultrasound regime $\delta^2k^2\ll1$ and the function f simplifies a lot

$$f=\frac{-7\mathrm{De}^2+5\mathrm{De}\sqrt{\mathrm{De}^2+1}+3}{3\left(\sqrt{\mathrm{De}^2+1}-\mathrm{De}\right)\left(\mathrm{De}^2+1\right)}.\tag{7.1.14}$$

Essentially only a function of the Deborah number $\mathrm{De}=\omega\lambda$ and independent of dynamic viscosity as for the classical Rayleigh streaming. In the viscous limit $\mathrm{De}=0$ the function $f=1$ and the well-known Rayleigh streaming condition appears. Furthermore there is a region where the slip condition is lower than the usual Rayleigh streaming, this is marked by the gray area in Fig. 7.1.

The viscoelastic Rayleigh streaming indicates a transition from positive to negative slip condition at $\mathrm{De}=1.63$, this indicates a flow reversal in the streaming. This flow reversal will now be investigated in the literature and simulated in COMSOL.

*subject to the boundary condition $v_{2,y}^\delta\to0$ for $z\to\infty$, so both integration constants are zero.

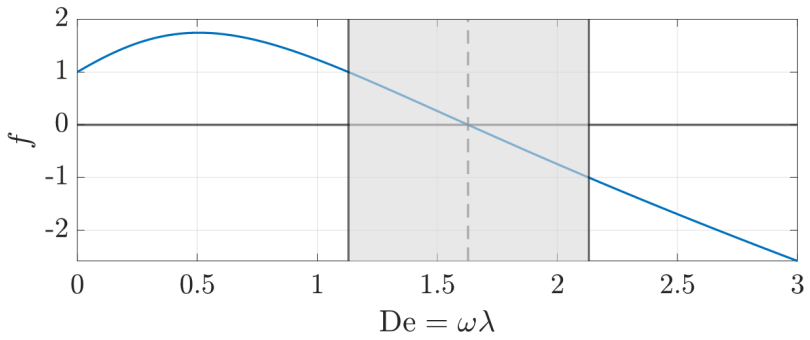

Figure 7.1: The slip condition function f as a function of the Deborah number De. The transition at De = 1.63 is indicated as a dashed line.

7.2 Steady viscoelastic flow reversal

The steady effects of using a viscoelastic fluid instead of a Newtonian has been studied in the low-sonic regime by [32, 33, Chang and Schowalter]. They found that the direction of the steady streaming was opposite that of a Newtonian fluid, the same streaming reversal was also observed by [34, 35, Hill et. al]. The reversal has also been predicted theoretically by several workers [33, 36, 37].

The setup used by [33, Chang and Schowalter] to observe the flow reversal is depicted in Fig. 7.2 and comprises a hollow outer cylinder with radius R and a massive inner cylinder with radius $a = 0.792\,\text{mm}$. The hollow outer cylinder comes in three different radii $R = 6.35\,\text{mm}$, $9.65\,\text{mm}$ and $13.3\,\text{mm}$, used to fit the measured profiles to a Deborah number according to their theory.

The inner cylinder was coupled to an alternating current which made it oscillating at frequency $f = 40\,\text{Hz}$ in the y-direction with displacement amplitude $d_0 = 1\,\text{mm}$. The low-sonic regime makes it very different from the ultrasound regime considered so far, and the boundary layer thickness is now in the order of $\delta{\sim}0.1\,\text{mm}$.

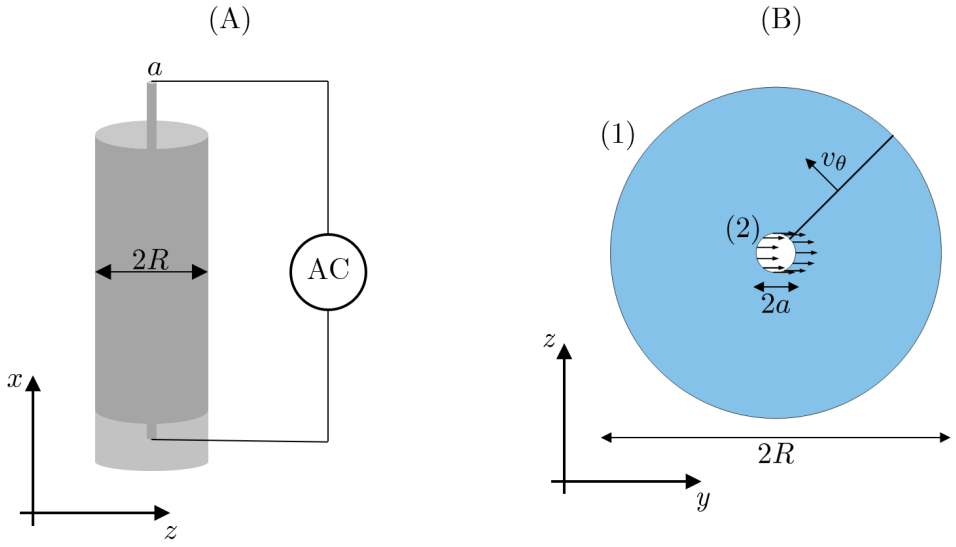

Figure 7.2: (A) Sketch of the setup used in Ref. [33]. (B) Top-view of the setup in the (y, z)-plane. Inner cylinder with radius $a = 0.792\,\text{mm}$ oscillating at $\omega = 2\pi 40\,\text{Hz}$ and outer cylinder with radius R. The oscillation is purely in the y-direction (black arrows). The diagonal black line indicates where the tangential streaming component v_θ is measured and evaluated. The numbers in parenthesis indicates the outer and inner boundaries.

7.2.1 Viscoelastic model in COMSOL

In order to implement the equations in the weak form module in COMSOL we again need equations of the strong form Eq. (3.1.2). To first order the viscoelastic model is almost similar to that of Eq. (4.1.5) apart from the stress tensor $\tau_{1,ij}$ i.e.

$$J_{ij}^{(\mathbf{v}_1)} = -p_1\delta_{ij} + \tau_{1,ij} = -p_1\delta_{ij} + \eta(\omega)\left(\partial_j v_{1,i} + \partial_i v_{1,j}\right), \tag{7.2.1a}$$

$$F_i^{(\mathbf{v}_1)} = -\mathrm{i}\rho_0\omega v_{1,i}, \tag{7.2.1b}$$

these equations are equivalent to the incompressible version of Eq. (3.1.2) apart from the complex valued Maxwell viscosity $\eta(\omega) = \frac{\eta_0}{1-\mathrm{i}\omega\lambda}$ with relaxation time λ.

To second order the stress tensor is again the only difference from the model presented in Section 4.1, so the viscoelastic streaming is governed by

$$J_{ij}^{(\mathbf{v}_2)} = -p_2\delta_{ij} + \tau_{2,ij} - \rho_0\left\langle v_{1,i}v_{1,j}\right\rangle, \tag{7.2.2a}$$

$$F_i^{(\mathbf{v}_2)} = 0, \tag{7.2.2b}$$

where

$$\begin{aligned}\boldsymbol{\tau}_2 =& \eta_0\left[\boldsymbol{\nabla}\mathbf{v}_2 + (\boldsymbol{\nabla}\mathbf{v}_2)^T\right] \\ &- \lambda\left[\left\langle(\mathbf{v}_1\cdot\boldsymbol{\nabla})\,\boldsymbol{\tau}_1\right\rangle - \left\langle\boldsymbol{\tau}_1\cdot\boldsymbol{\nabla}\mathbf{v}_1\right\rangle - \left\langle(\boldsymbol{\nabla}\mathbf{v}_1)^T\cdot\boldsymbol{\tau}_1\right\rangle\right].\end{aligned} \tag{7.2.3}$$

These equations comprises our numerical viscoelastic model, together with the equations governing the first order pressure Eq. (4.1.4) and the time-averaged second order pressure Eq. (4.1.7).

The boundary conditions for the first order velocity fields are the no-slip conditions

$$\hat{\mathbf{n}} \cdot \mathbf{v}_1 = 0 \quad \text{for} \quad \mathbf{r} \in (1), \tag{7.2.4a}$$
$$\mathbf{v}_1 = -\mathrm{i}\omega d_0 \hat{\mathbf{e}}_y \quad \text{for} \quad \mathbf{r} \in (2), \tag{7.2.4b}$$

implemented as a constraint on the velocity field.

As for the time-averaged second order velocity field the conditions are that of Stokes drift

$$\hat{\mathbf{n}} \cdot \mathbf{v}_2 = 0 \quad \text{for} \quad \mathbf{r} \in (1), \tag{7.2.5a}$$
$$\mathbf{v}_2 = -\left\langle \left(\frac{\mathrm{i}}{\omega} \mathbf{v}_1 \cdot \boldsymbol{\nabla} \right) \mathbf{v}_1 \right\rangle \quad \text{for} \quad \mathbf{r} \in (2). \tag{7.2.5b}$$

Again similar to the model presented in Section 4.2 and implemented as a Dirichlet boundary condition.

7.2.2 Viscoelastic streaming

In the experiment conducted by [32, Chang and Schowalter] the tangential flow profiles v_θ along the 45° diagonal was measured at three different outer radii $R = 6.35\,\mathrm{mm}$, $9.65\,\mathrm{mm}$ and $13.3\,\mathrm{mm}$, for both Newtonian and a viscoelastic fluid. The Newtonian fluid consisted of a water-glycerol mixture with density $\rho_0 = 1.235\,\mathrm{g/cm^3}$ and dynamic viscosity $\eta_0 = 6.08\,\mathrm{mPa\,s}$. For the viscoelastic fluid they used a 100 p.p.m. aqueous PolyHall 295 solution with density $\rho_0 = 1.0374\,\mathrm{g/cm^3}$ and dynamic viscosity $\eta_0 = 375\,\mathrm{mPa\,s}$.

The two different fluids will have different boundary layer thickness due to the difference in dynamic viscosity

$$\delta_{\mathrm{w/g}} = 0.198\,\mathrm{mm} \quad \text{and} \quad \delta_{295} = 1.70\,\mathrm{mm}. \tag{7.2.6}$$

The numerical results for the tangential streaming profile v_θ along the 45° diagonal (according to Fig. 7.2) is presented in Fig. 7.3. By comparing to Ref. [33] there is an agreement within ∼10% to the experimental measured profiles. This comparison serves as a verification to our numerical results.

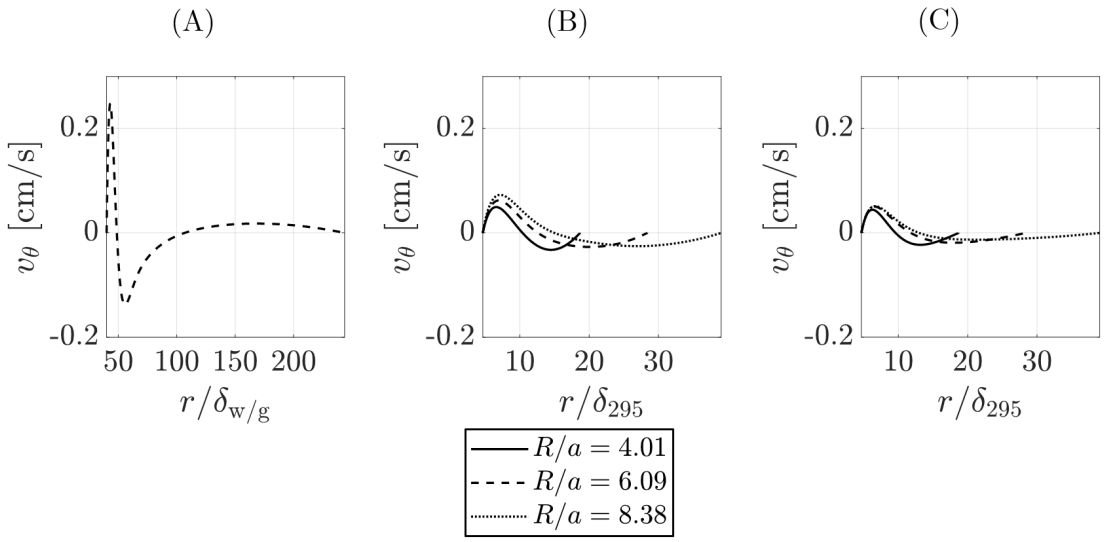

Figure 7.3: Tangential streaming profile along the 45° diagonal indicated in Fig. 7.2, as a function of radial distance r normalized to the boundary layer thickness. (A) For a Newtonian water-glycerol mixture with density $\rho_0 = 1.235\,\mathrm{g/cm^3}$ and dynamic viscosity $\eta_0 = 6.08\,\mathrm{mPa\,s}$ for the cylindrical ratio $R/a = 6.09$. (B) For a 100 p.p.m. aqueous PolyHall 295 solution with density $\rho_0 = 1.0374\,\mathrm{g/cm^3}$ and dynamic viscosity $\eta_0 = 375\,\mathrm{mPa\,s}$ at different geometric ratios, as indicated in the legend. (C) Same settings as in (B) but for a Newtonian fluid i.e. $\mathrm{De} = 0$.

In Fig. 7.3.(A) the Newtonian water-glycerol mixture has two zero crossings, which means that two streaming rolls are present; one below $r/\delta_{\mathrm{w/g}}{\sim}55$ and one above. For the viscoelastic case there exist only one zero crossing which means only one roll are present. In Fig. 7.3.(C) the same mass density and dynamic viscosity, as for the 100 p.p.m. aqueous PolyHall 295 solution, has been used to model the flow in the Newtonian limit $\mathrm{De} = 0$. Comparing Fig. 7.3.(B) and Fig. 7.3.(C) shows a discrepancy in magnitude but same qualitative behaviour, Without the viscoelastic parameter De we would underestimate the streaming amplitude.

The streaming profiles in Fig. 7.3.(B) are shown in Fig. 7.4 as a 2D vector plot. Here the vector field is the time-averaged Lagrangian velocity $\langle \mathbf{V}_2 \rangle$ i.e. the velocity at which a point particle travels

$$\langle \mathbf{V}_2 \rangle = \mathbf{v}_2 + \left\langle \frac{\mathrm{i}}{\omega} \left(\mathbf{v_1} \cdot \boldsymbol{\nabla} \right) \mathbf{v}_1 \right\rangle . \tag{7.2.7}$$

These plots serves as a further verification to our model and the streamlines presented in Ref. [33].

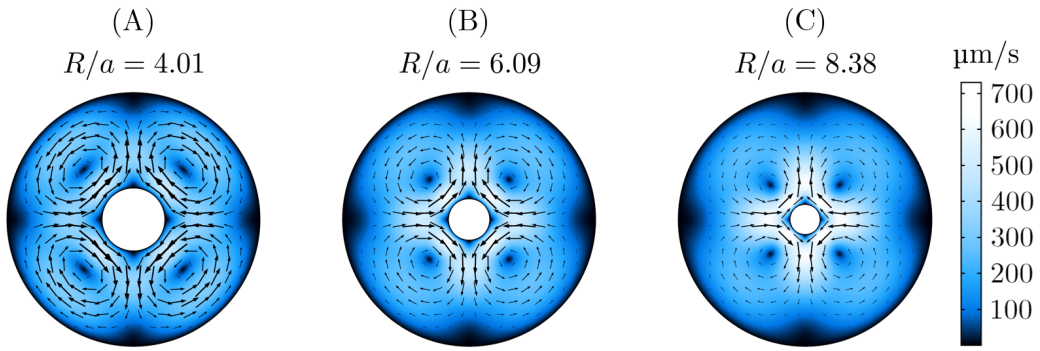

Figure 7.4: Streaming at three different ratios between inner and outer cylinder, for the 100 p.p.m. PolyHall 295 solute. The surface plot indicates the streaming magnitude and the vector plot indicates the time-averaged Lagrangian velocity $\langle \mathbf{V}_2 \rangle$.

Increased relaxation time

By considering the same setup as above, now with water instead of the viscoelastic PolyHall 295 solution, we can artificially tune the relaxation time, making the water more and more viscoelastic. In reality one would dissolve a polymer solute to achieve increased viscoelastic behaviour. This artificial fluid is used to give an indication of how the streaming behave as the fluid gets increasingly viscoelastic.

To give a measure of how the streaming depends on the viscoelastic parameter De the streaming energy density $E_{\text{st}} = \rho_0 c_0 |\mathbf{v}|$ is probed while sweeping in De from 0 to 0.44. The sweep is presented in Fig. 7.5.(A) together with chosen streaming profiles Fig. 7.5.(B).

As seen in Fig. 7.5.(A) there clearly exist a minimum at De = 0.29, which also indicates a transition. To assess whether or not it is due to flow reversal, the profiles at different De values are visualised in Fig. 7.5.(B).

Here the streamlines is plotted at four different Deborah numbers (indicated as diamonds in Fig. 7.5.(A)) equal in energy density around the transition point. The incompressible Newtonian fluid is obtained at De = 0, here two rolls are present, which is the same situation for De = 0.15.

At De = 0.35 the flow reversal is evident and only one streaming roll is present, the same goes for De = 0.37. For the given geometry the transition happens at De = 0.29, where the streaming energy has decreased from 150 Pa to 130 Pa, above this transition the streaming increases as the viscoelastic fluid gets more and more elastic.

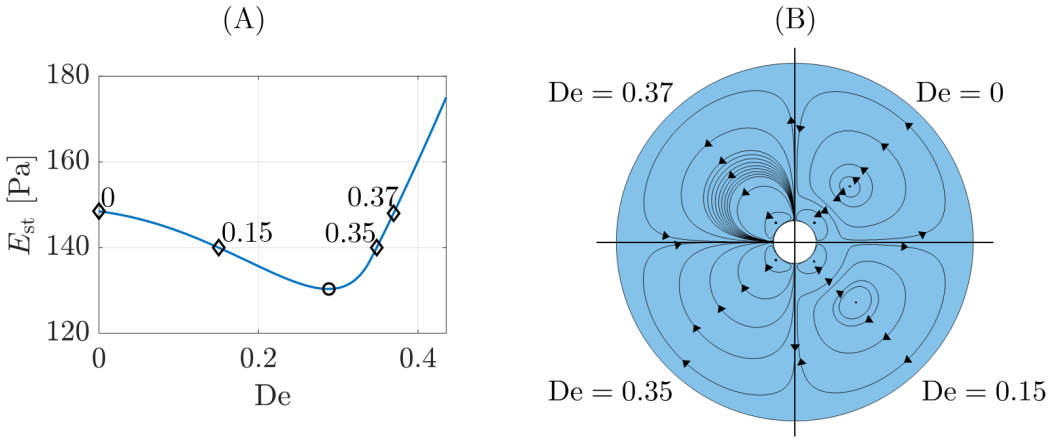

Figure 7.5: (A) Streaming energy as a function of the viscoelastic parameter De. The minimum energy is marked with a circle and the diamonds indicates the Deborah numbers at which the streamlines are visualised. (B) Streamlines at four different Deborah numbers (each quadrant) as indicated with diamonds in (A). The black arrows indicates the streaming direction.

Rectangular channel

It is interesting to see what happens if we apply the same conditions to the acoustofluidic device presented in Chapter 4. To simplify the problem, we only model the acoustic fields inside the microchannel corresponding to hard walls as in Eq. (6.1.3). Apart from the geometrically different system it is also at MHz frequencies very different from the Hz regime.

As before, the viscoelastic behaviour is characterised by increasing the Deborah number De from 0 to 2.4 and at the same time probing the streaming energy density as shown in Fig. 7.6.(A). This characteristic is very different from the cylindrical system in Fig. 7.5, but very close to the viscoelastic Rayleigh streaming condition in Fig. 7.1, as would be expected.

The streaming is again assessed by plotting the streamlines at different De values together with the acoustic pressure, as shown in Fig. 7.6.(B). The transition at De = 1.63 is again characterised by flow reversal visualised in Fig. 7.6.(B) at De $= 0, 0.68, 1.85, 2.07$. Here the streamlines in second and third quadrant is opposite to the first and fourth quadrant—all of Rayleigh type streaming profiles. The transition is equal to the theoretical predicted at De = 1.63 as shown in Fig. 7.1.

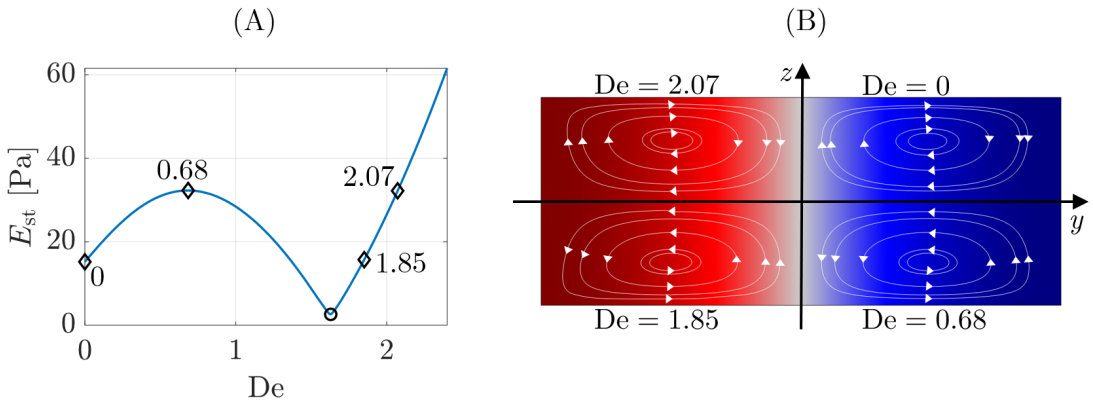

Figure 7.6: (A) Streaming energy density as a function of the viscoelastic parameter De. The minimum energy at De = 1.63 is marked with a circle and the diamonds indicates the Deborah numbers used to visualise the streamlines. (B) Streamlines at four different Deborah numbers (each quadrant) as indicated with diamonds in (A). The white arrows indicates the streaming direction. The acoustic pressure p_1 is presented as a surface plot (red is positive, blue is negative and gray is zero).

For both cases presented above there seems to be a certain relaxation time where the streaming is at a minimum. For the cylindrical low-sonic system the streaming energy density E_{st} went from 150 Pa to 130 Pa, whereas the rectangular ultrasound system went from 15.2 Pa to 2.60 Pa. This analysis suggest a method to minimise the streaming by having a viscoelastic fluid with the right Deborah number, depending on the system. In reality a change in the Deborah number can be obtained by gradually increasing the concentration of a polymer solution as in Ref. [38].

The flow reversal shown in Ref. [33] was concluded to originate from the viscoelastic behaviour, but in Fig. 7.3 the same reversal was was obtained with a Newtonian model. This suggest that this presumable flow reversal could as well be a consequence of the viscous boundary layer being similar to the system dimensions. Since by increasing the dynamic viscosity the inner boundary layer streaming in Fig. 6.1 begins to appear, and eventually the dimensions of the device becomes comparable to the boundary layer thickness.

Chapter 8

Conclusion and outlook

Starting from the all-polymer PMMA device, we demonstrated and verified how such systems suggests an alternative to the conventional hard Pyrex/silicon systems, when doing acoustophoresis. Furthermore we showed how such system can be optimised in terms of base height and channel position, yielding acoustophoresis comparable to hard-wall systems.

Next we turned to simulate the second order streaming. Even though the soft all-polymer PMMA device is very different from Pyrex, many streaming features remains the same. The most pronounced difference was the normalised streaming magnitude being larger, suggested to originate from a small departure in the standing pressure half-wave. The particle trajectories also indicated the same critical particle radius compared to previous work on hard-wall systems [22, 23].

Next we studied the novel aluminium-PDMS device, categorised as a hard-wall-soft-lid device. This numerical analysis revealed how the acoustic response in the water channel is sensitive to the asymmetric actuation. Consequently the acoustic fields are asymmetric together with the acoustic pressure nodal plane. The PDMS turned out to be problematic in terms of the interface at the top corners, essentially driving the acoustic streaming. By artificially tuning the material parameters towards that of PMMA, the problem was identified to originate from the low transverse speed of sound for the given PDMS. Our partners were not able to tell which kind of PDMS they used for the device. Again this emphasises the need of measured material parameters for the given device. This is a necessity to ensure the predictive ability.

Our analysis also emphasize that a more systematic use of soft walls may lead to enhanced control over the resulting streaming fields, and may even suppress the streaming altogether. A much more intensive numerical and experimental study of soft walls is needed to fully understand the nature of hard-wall-soft-lid streaming. These results open up the possibility of using cheap and easily manufactured acoustofluidic devices to manipulate

sub-micrometer and nanometer particles.

Some of these results were presented in two abstracts submitted to the Acoustofluidics conference 2019 [30, 31].

Finally we described the second order streaming for a viscoelastic fluid in terms of the convected Jeffrey's model. Successfully, we were able to calculate the classical Rayleigh streaming condition for a viscoelastic fluid. The reformulated boundary condition predicted a flow reversal above the transition, defined in terms of the the relaxation time and angular frequency. This transition was in agreement with our numerical studies.
Flow reversal was observed by [33, C-F. Chang and W.R. Schowalter] in the low-sonic regime, but could as well originate from the streaming inside the boundary layer, since the same velocity profiles was obtained with a Newtonian fluid. This theoretically predicted flow reversal due to viscoelasticity at MHz frequencies remains to be verified by experiments (work in progress).

In the end, polymer acoustofluidic systems provides an alternative to conventional acoustophoresis and open up for:

- cheap acoustophoresis,
- enhanced streaming control using a soft polymer lid,
- suppressed streaming due to viscoelastic properties and
- possible sub-micron acoustophoresis.

Appendix A

Material parameters

A.1 Fluid and particle parameters

Table A.1: Material parameters at 25 °C for selected fluids.

Parameter	Symbol	Water	Water/Glycerol	100 p.p.m. aqueous PolyHall 295	Unit
source		[8]		[33]	
Mass density	ρ_{fl}	997.05	1235	1037	$\mathrm{kg/m^3}$
Dynamic viscosity	η_0	0.89	6.08	375	mPa s
Compressibility	κ_{fl}	447.7	-	-	$\mathrm{TPa^{-1}}$
Speed of sound	c_0	1496.7	1496.7	-	m/s
Damping coefficient	Γ_{fl}	Eq. (2.3.9)	0.0004	2×10^{-5}	1
Specific impedance	Z_{fl}	1.49	-	-	MPa s/m

Table A.2: Material parameters at 25 °C for selected tracer particles

Parameter	Symbol	Polystyrene	Unit
source		[39, 40]	
Radius	a	10	µm
Mass density	ρ_{p}	1050	$\mathrm{kg/m^3}$
Compressibility	κ_{p}	238	$\mathrm{TPa^{-1}}$
Monopole coefficient	f_{mp}	0.468	1
Dipole coefficient	f_{dp}	0.034	1
Acoustic contrast factor	Φ_{ac}	0.1733	1

A.2 Elastic parameters

Table A.3: Material parameters at 25 °C for selected solids. The specific impedance is calculated as $Z_{\mathrm{sl}} = \rho_{\mathrm{sl}} c_{\mathrm{l}}$.

Parameter	Symbol	PMMA	Pyrex	PDMS	Unit
source		[41–45]	[46]	[28, 29]	
Mass density	ρ_{sl}	1170	2230	1020	$\mathrm{kg/m^3}$
Transverse speed of sound	c_{t}	1105	3424	$66.26 - \mathrm{i}12.82$	m/s
Longitudinal speed of sound	c_{l}	2706	5592	$1008 - \mathrm{i}2.292$	m/s
Damping coefficient	Γ_{sl}	0.0040	0.0004	-	1
Specific impedance	Z_{sl}	3.19	12.47	1.028	MPa s/m

A.3 Piezoelectric material parameters

Table A.4: Material parameters of Ferroperm Ceramic Pz26 [26]. The x-y isotropy implies $C_{66} = \frac{1}{2}(C_{11} - C_{12})$.

Parameter	Pz26	Unit
source	Meggitt A/S [26]	
ρ_{sl}	7700	$\mathrm{kg/m^3}$
Γ_{sl}	0.02	1
C_{11}	168	GPa
C_{12}	110	GPa
C_{13}	99.9	GPa
ϵ_{11}	828	ϵ_0
C_{33}	123	GPa
C_{44}	30.1	GPa
C_{66}	29.0	GPa
ϵ_{33}	700	ϵ_0
e_{31}	-2.8	$\mathrm{C/m^2}$
e_{33}	14.7	$\mathrm{C/m^2}$
e_{15}	9.86	$\mathrm{C/m^2}$

Appendix B

Resonance properties

Table B.1: Pyrex-water. Different resonances presented together with their acoustic energy density $E_{\mathrm{ac}}^{(\mathrm{fl})}$, their radiation force components $\bar{F}_y$ and $\bar{F}_z$ and the figure of merit $\mathcal{R}$.

Resonance	Frequency [MHz]	$E_{\mathrm{ac}}^{(\mathrm{fl})}$ [Pa]	$\bar{F}_y$ [pN]	$\bar{F}_z$ [pN]	$\mathcal{R}$ 1
1	1.185	1081	−975	161	6.07
2	1.499	10.3	−9.88	4.66	2.12
3	1.851	396	−556	16.2	34.4
4	1.919	155	−219	4.42	49.7

Table B.2: PMMA-water. Different resonances presented together with their acoustic energy density $E_{\mathrm{ac}}^{(\mathrm{fl})}$, their radiation force components $\bar{F}_y$ and $\bar{F}_z$ and the figure of merit $\mathcal{R}$.

Resonance	Frequency [MHz]	$E_{\mathrm{ac}}^{(\mathrm{fl})}$ [Pa]	$\bar{F}_y$ [pN]	$\bar{F}_z$ [pN]	$\mathcal{R}$ 1
1	1.042	7.14	−5.58	0.828	6.74
2	1.064	0.590	−0.470	0.078	6.00
3	1.099	0.497	−0.392	0.062	6.37
4	1.132	3.97	−3.53	0.235	15.0
5	1.215	0.0171	−0.0100	0.007	1.34
6	1.279	0.564	−0.256	0.243	1.05
7	1.381	1.40	−1.45	0.221	6.56
8	1.453	4.44	−4.73	0.770	6.14
9	1.580	0.0490	−0.0409	0.028	1.46
10	1.652	0.0735	−0.0609	0.030	2.06
11	1.685	0.0422	−0.0119	0.029	0.407
12	1.739	0.121	−0.108	0.065	1.65
13	1.781	2.99	−3.14	2.73	1.15
14	1.904	0.724	−0.453	0.431	1.05
15	2.047	0.276	0.0100	0.146	−0.069
16	2.080	0.374	−0.0553	0.276	0.200

Table B.3: Aluminium-PDMS device. Different resonances presented together with the acoustic energy density $E_{\mathrm{ac}}^{(\mathrm{fl})}$, radiation force components $\bar{F}_y$ and $\bar{F}_z$ and figure of merit $\mathcal{R}$.

Resonance	Frequency [MHz]	$E_{\mathrm{ac}}^{(\mathrm{fl})}$ [Pa]	$\bar{F}_y$ [pN]	$\bar{F}_z$ [pN]	$\mathcal{R}$ 1
1	1.847	1.518	0.000	2.055	0.00
2	1.961	0.090	−0.029	0.115	0.25
3	2.090	0.038	−0.003	0.055	0.06
4	2.246	0.019	−0.022	0.020	1.07
5	2.345	0.020	−0.018	0.023	0.75
6	2.452	0.009	−0.010	0.011	0.96
7	2.646	0.002	−0.002	0.002	0.75
8	2.744	0.001	0.000	0.001	−0.18

Appendix C

Acoustic device designs

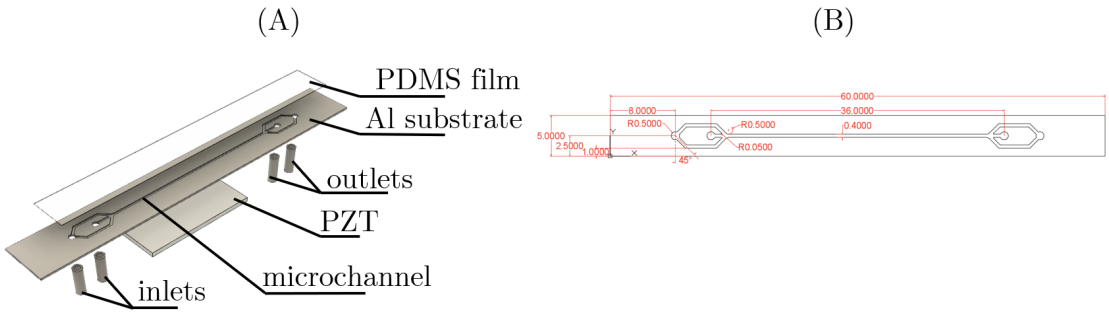

Figure C.1: Aluminium-PDMS device prints. The units are in mm.

Appendix D

Viscoelastic Rayleigh streaming

The complete function f according to the integral equation in Eq. (7.1.11) is

$$\begin{aligned} f =& \frac{1}{3c^2\rho\,(\omega^2\lambda^2+1)\,(p^2+q^2)^2\,p^2}\,\big[-8\,c^2\omega^2\left(p^4-9/4\,q^2p^2-1/4\,q^4\right)\rho\,\lambda^2 \\ &+2\,\left(\left(10\,\eta\,p^2+4\,q^2\eta\right)\omega+c^2\rho\,\left(p^4-q^4\right)\right)\omega\,\left(p^2+q^2\right)\lambda \\ &-8\,c^2\left(p^4-9/4\,q^2p^2-1/4\,q^4\right)\rho\big] \end{aligned} \tag{D.0.1}$$

$$p=\sqrt{\sqrt{\omega^2\lambda^2+1}-\omega\lambda}\quad\text{and}\quad q=\sqrt{\sqrt{\omega^2\lambda^2+1}+\omega\lambda}. \tag{D.0.2}$$

Bibliography

[1] P. Augustsson, J. T. Karlsen, H.-W. Su, H. Bruus, and J. Voldman, *Iso-acoustic focusing of cells for size-insensitive acousto-mechanical phenotyping*. Nature Communications **7**(1), 11556 (2016).

[2] B. Hammarström, B. Nilson, T. Laurell, J. Nilsson, and S. Ekström, *Acoustic trapping for bacteria identification in positive blood cultures with MALDI-TOF MS*. Analytical Chemistry **86**(21), 10560–10567 (2014).

[3] B. W. Drinkwater, *Dynamic-field devices for the ultrasonic manipulation of microparticles*. Lab on a Chip **16**(13), 2360–2375 (2016).

[4] P. Sehgal and B. J. Kirby, *Separation of 300 and 100 nm particles in fabry–perot acoustofluidic resonators*. Analytical Chemistry **89**(22), 12192–12200 (2017).

[5] R. Barnkob, *Physics of microparticle acoustophoresis*. Ph.D. thesis, Technical University of Denmark (2012).

[6] R. P. Moiseyenko and H. Bruus, *Whole-system ultrasound resonances as the basis for acoustophoresis in all-polymer microfluidic devices*. Physical Review Applied **11**(1), 014014 (2019).

[7] AcouSort AB. `https://acousort.com/`, (2019).

[8] P. B. Muller and H. Bruus, *Numerical study of thermoviscous effects in ultrasound-induced acoustic streaming in microchannels*. Phys. Rev. E **90**(4), 043016 (2014).

[9] J. T. Karlsen and H. Bruus, *Forces acting on a small particle in an acoustical field in a thermoviscous fluid*. Physical Review E **92**(4), 043010 (2015).

[10] M. Settnes and H. Bruus, *Forces acting on a small particle in an acoustical field in a viscous fluid*. Phys. Rev. E **85**, 016327 (2012).

[11] J. S. Bach and H. Bruus, *Theory of pressure acoustics with viscous boundary layers and streaming in curved elastic cavities*. The Journal of the Acoustical Society of America **144**(2), 766–784 (2018).

[12] J. G. Oldroyd, *On the formulation of rheological equations of state*. Proceedings of the Royal Society of London. Series A. Mathematical and Physical Sciences **200**(1063), 523–541 (1950).

[13] R. B. Bird, R. C. Armstrong, and O. Hassager, *Dynamics of Polymeric Liquids, Volume 1: Fluid Mechanics* (Wiley-Interscience) (1987).

[14] COMSOL Multiphysics 5.4, www.comsol.com (2019).

[15] P. B. Muller, R. Barnkob, M. J. H. Jensen, and H. Bruus, *A numerical study of microparticle acoustophoresis driven by acoustic radiation forces and streaming-induced drag forces*. Lab Chip **12**, 4617–4627 (2012).

[16] A. Nilsson, F. Petersson, H. Jönsson, and T. Laurell, *Acoustic control of suspended particles in micro fluidic chips*. Lab Chip **4**(2), 131–135 (2004).

[17] M. W. Ley and H. Bruus, *Three-dimensional numerical modeling of acoustic trapping in glass capillaries*. Physical Review Applied **8**(2), 204020 (2017).

[18] AcouSort AB. private communication (2018).

[19] L. Rayleigh, *On the circulation of air observed in Kundt's tubes, and on some allied acoustical problems*. Philos Trans R Soc London **175**, 1–21 (1884).

[20] C. Eckart, *Vortices and streams caused by sound waves*. Phys. Rev. **73**(1), 68–76 (1948).

[21] W. L. Nyborg, *Acoustic streaming near a boundary*. J. Acoust. Soc. Am. **30**(4), 329–339 (1958).

[22] R. Barnkob, P. Augustsson, T. Laurell, and H. Bruus, *Acoustic radiation- and streaming-induced microparticle velocities determined by microparticle image velocimetry in an ultrasound symmetry plane*. Phys. Rev. E **86**, 056307 (2012).

[23] P. B. Muller, M. Rossi, A. G. Marin, R. Barnkob, P. Augustsson, T. Laurell, C. J. Kähler, and H. Bruus, *Ultrasound-induced acoustophoretic motion of microparticles in three dimensions*. Phys. Rev. E **88**(2), 023006 (2013).

[24] J. T. Karlsen, W. Qiu, P. Augustsson, and H. Bruus, *Acoustic streaming and its suppression in inhomogeneous fluids*. Physical Review Letters **120**(5), 054501 (2018).

[25] W. Qiu, J. T. Karlsen, H. Bruus, and P. Augustsson, *Experimental characterization of acoustic streaming in gradients of density and compressibility*. Physical Review Applied **11**(2), 024018 (2019).

[26] Meggit A/S, *Ferroperm matdat 2017 - pz26*. `https://www.meggittferroperm.com/`,

(2018).

[27] R. Barnkob, C. J. Kähler, and M. Rossi, *General defocusing particle tracking.* Lab on a Chip **15**(17), 3556–3560 (2015).

[28] D. L. Folds, *Speed of sound and transmission loss in silicone rubbers at ultrasonic frequencies.* The Journal of the Acoustical Society of America **56**(4), 1295–1296 (1974).

[29] E. L. Madsen, H. J. Sathoff, and J. A. Zagzebski, *Ultrasonic shear wave properties of soft tissues and tissuelike materials.* The Journal of the Acoustical Society of America **74**(5), 1346–1355 (1983).

[30] L. Jiang, W. Qiu, W. N. Bodé, N. Peng, A. Lenshof, H. Bruus, and T. Laurell, *Characterization of acoustic streaming and its potential suppression in aluminum-pdms acoustofluidic chips.* Proceedings Acoustofluidics 2019, Twente 25-27 August 2019 submitted (2019).

[31] W. N. Bodé and H. Bruus, *Modeling of acoustophoresis in hard microchannels with soft lids.* Proceedings Acoustofluidics 2019, Twente 25-27 August 2019 submitted (2019).

[32] C.-F. Chang and W. Schowalter, *Flow near an oscillating cylinder in dilute viscoelastic fluid.* Nature **252**(5485), 686–688 (1974).

[33] C.-F. Chang and W. Schowalter, *Secondary flow in the neighborhood of a cylinder oscillating in a viscoelastic fluid.* Journal of Non-Newtonian Fluid Mechanics **6**(1), 47–67 (1979).

[34] C. T. Hill, J. D. Huppler, and R. B. Bird, *Secondary flows in the disk-and-cylinder system.* Chemical Engineering Science **21**(9), 815–817 (1966).

[35] C. T. Hill, *Nearly viscometric flow of viscoelastic fluids in the disk and cylinder system.* Transactions of the Society of Rheology **16**(2), 213–245 (1972).

[36] R. L. Powell, *Acoustic streaming reversal by a finite amplitude sound wave in a non-newtonian fluid.* The Journal of the Acoustical Society of America **71**(5), 1118–1123 (1982).

[37] G. Böhme, *On steady streaming in viscoelastic liquids.* Journal of Non-Newtonian Fluid Mechanics **44**, 149–170 (1992).

[38] K. W. Ebagninin, A. Benchabane, and K. Bekkour, *Rheological characterization of poly(ethylene oxide) solutions of different molecular weights.* Journal of Colloid and Interface Science **336**(1), 360–367 (2009).

[39] B. Hartmann and J. Jarzynski, *Polymer sound speeds and elastic constants.* Naval

Ordnance Laboratory Report NOLTR 72–269 (1972).

[40] J. T. Karlsen and H. Bruus, *Forces acting on a small particle in an acoustical field in a thermoviscous fluid*. Phys. Rev. E **92**, 043010 (2015).

[41] H. J. Sutherland and R. Lingle, *An acoustic characterization of polymethyl methacrylate and three epoxy formulations*. Journal of Applied Physics **43**(10), 4022–4026 (1972).

[42] H. J. Sutherland, *Acoustical determination of the shear relaxation functions for polymethyl methacrylate and epon 828-z*. Journal of Applied Physics **49**(7), 3941–3945 (1978).

[43] J. E. Carlson, J. van Deventer, A. Scolan, and C. Carlander, *Frequency and temperature dependence of acoustic properties of polymers used in pulse-echo systems*. In *IEEE Symposium on Ultrasonics, 2003*, 885–888 (IEEE) (2003).

[44] P. H. Mott, J. R. Dorgan, and C. M. Roland, *The bulk modulus and poisson's ratio of "incompressible" materials*. J Sound Vibr **312**(4-5), 572–575 (2008).

[45] M. Treiber, J.-Y. Kim, L. J. Jacobs, and J. Qu, *Correction for partial reflection in ultrasonic attenuation measurements using contact transducers*. The Journal of the Acoustical Society of America **125**(5), 2946 (2009).

[46] Corning, *Glass silicon constraint substrates*. `https://www.corning.com`, (2019).